学 位 論 文

Development of a 100-meter Delay-Line Laser Interferometer

(100 メートル ディレーライン型レーザー干渉計の開発)

平成7年12月 博士（理学）申請

東京大学大学院理学系研究科物理学専攻

三代木 伸二

Development of a 100-meter Delay-Line Laser Interferometer

by

Shinji Miyoki

March 1996

A Dissertation Submitted
for the Degree of
Doctor of Science

Department of Physics
Graduate School of Science
The University of Tokyo
3-1-1 Hongo, Bunkyo-ku, Tokyo, Japan

Contents

List of Figures

List of Tables

Acknowledgement

I would like to acknowledge some of those who have been instrumental in the completion of my doctoral work and my growth as an experimental physicist.

I am grateful to leaders of Gravitational Wave Group in Japan who supported our experiment at ISAS, specially, Professor.T.Nakamura, Professor.K.Thubono, Professor.M.Fujimoto, Professor.K.Ueda, Professor.K.Kuroda, Professor.N.Mio and Dr.M.Ohashi for constant advice over the years.

I am especially grateful to my supervisor, Professor.N.Kawashima, for his tolerant heart to give me a chance to participate in a project at ISAS, and for his support and advice to accomplish my work.

I heartily thank my previous advisor, Dr.S.Kawamura at California Institute of Technology (Caltech) and Dr.D.H.Shoemaker at Massachusetts Institute of Technology (MIT), for giving me a lot of ultimate pedagogical wisdom and advice in deciding the basic design of TENKO-100.

I am also grateful to many of my senior colleagues including Dr.E.Mizuno, Dr.J.Mizuno, Dr.R.Takahashi, Professor.J.Hirao and Dr.E.Heflin for their assistance and advice.

I wish to thank many of my colleagues of the Institute of Space and Astronautical Science, the National Astronomical Observatory, the National Laboratory for High Energy Physics, the University of Electro-Communications, the Institute of Cosmic Ray Research and the University of Tokyo for their companionship and advice.

Additionally, I would like to acknowledge the support from those who have helped me over the years in my pursuit of physics, especially Mr.Chujo and Mr.Nishioka.

This work was supported by the Japanese Society for Promotion of Science (JSPS).

Chapter 1

Introduction

A wave solution traveling with the speed of light was deduced from Einstein's field equation under the weak gravitational field, which is so-called as "Gravitational Waves". They are expected to be radiated from supernovae and coalescence of compact binary stars. Although the radiation of gravitational waves was observed indirectly by J.H.Taylor *et al* from PSR1913+16, any gravitational waves have not been observed directly yet as "ripples of space-time" because of its weak interaction, and insufficient optical and electrical technology at that time. However, at present, the gravitational wave is regarded as the realistic and promising observational tool which realizes "Gravitational Wave Astronomy", and many groups in the world have been proceeding the research and the development for the gravitational wave detectors.

1.1 General Theory of Relativity and Gravitational Waves

The General Theory of Relativity by Einstein predicts various phenomena in space-time [1] which cannot be deduced from Newton dynamics. They are the slowing of time and Lorentz contraction of length of objects traveling with nearly the speed of light, the space curvature, the gravitational lensing and the gravitational wave. Although the equivalence principle fundamental for the General Relativity and other relativistic phenomena have been verified directly, one important consequence of the General Relativity, *i.e.* the gravitational wave, has not been verified directly yet [2, 3, 4, 5, 6, 7, 8].

According to the General Relativity, a wave solution is deduced from the Einstein's field equation analogously with an electromagnetic wave from Maxwell Equation, which is so-called gravitational wave [9]. It propagates with the speed of light as electromagnetic wave and its effect is observed as a small change of the distance between two free falling points in space-time. For example, the effect of gravitational waves from the Virgo Cluster is equivalent to the change of the scale of Hydrogen on length to the distance between the Sun and the Earth. Such relative change of 10^{-21} is due to its weak interaction, and this is partly why it has not been detected yet. Its detection not only verifies the General Relativity but also brings much information about the mechanism of supernova explosions, the General Relativity in the strong relativistic field such as neutron binary systems and black holes, and atomic phenomena during collisions of compact binary stars. In order to detect so weak gravitational waves as a new channel of observation, the development of a detector itself is quite important work.

1.2 History of Gravitational Wave Detection

Historically, the first experimental attempt to detect gravitational waves directly was done by J. Weber in 1969 with two bar-type detectors [10]. His trial encouraged other scientists to detect gravitational waves. Recently, J.H.Taylor *et al* succeeded in obtaining indirect evidence of a gravitational wave radiation from a binary pulsar system, PSR1913+16. The method was based on the advancement of the perihelion shift derived from the observation of pulses from the pulsar in accordance with 0.4 % from the theoretical prediction [11] from the General Relativity.

At present, many laboratories have been developing gravitational wave detectors for the direct detection of gravitational waves as "ripples of space-time" for "Gravitational Wave Astronomy" in future. Of the different detection types presently in use such as resonant type detectors, laser interferometric detectors, and doppler tracking (detailed in Chapter 3), laser interferometric detectors are becoming the popular detectors from early resonant-type detectors because they have wide-band property in general and their sensitivities can be increased with longer arm length in contrast to resonant-type detectors whose sensitivities are limited by quantum limit. Although the best sensitivity of laser

interferometric detectors of the world is $8 \times 10^{-21}\, 1/\sqrt{\text{Hz}}$ in strain obtained by 40m Fabry-Perot interferometer at Caltech, the strain sensitivity of $h = 10^{-21}\, 1/\sqrt{\text{Hz}}$ is needed to observe several bursts from supernova explosions or coalescence of compact binary stars in Virgo cluster over the period of a year. To attain this level, Caltech and MIT are proceeding LIGO project to develop two km-class Fabry-Perot interferometric gravitational wave detectors with 4 km base-line in USA. LIGO project is based on scaling the 40m Fabry-Perot interferometer at Caltech [12]. Pisa and Orseille groups are also proceeding VIRGO project to develop a km-class Fabry-Perot interferometric gravitational wave detector with 3 km arm length in Italy. The other major effort is TAMA project in Japan which also started in 1995 to develop a Fabry-Perot interferometric gravitational wave detector with 300m base-line in the NAO at Mitaka [13]. TAMA project is based on scaling the 20m Fabry-Perot interferometer in NAO [14, 15] and the 100m Delay-Line interferometer (named as TENKO-100) at ISAS which is described about its development in this thesis.

1.3 Thesis Overview

In this thesis, I report on the development of the prototype 100m Delay-Line laser interferometric gravitational wave detector (TENKO-100) which is based on scaling TENKO-10 [16] developed in ISAS from 1980 to 1991. At that time when we started constructing of TENKO-100 in 1991, the each advantage of the Fabry-Perot type and the Delay-Line type was not verified. The Fabry-Perot type has advantages for a km-class : (1) It has small mirror size (30 cm) and accepts roughness of mirror surface ($\lambda/30$), (2) Lower contribution of the scattered light noise because of its superimposed beam path. However, it has disadvantages : (1) Feedback topology is difficult and complex, (2) Difficulties of matching reflectivity of mirrors, and it needs mirrors with extremely low optical loss. On the other hand, the Delay-Line type has advantages : (1) Feedback topology is quite easy and simple, (2) Various selections of material for mirrors. However, it has disadvantages : (1) High contribution of the scattered light noise because of its separate beam paths, (2) It needs big mirror size (60 cm) and high quality of roughness of mirror surface ($\lambda/100$), and it is quite difficult to match the mirror curvatures equally. Therefore, it is very important to evaluate the performance of both interferometers for the future km-class interferometer.

Because of technical simplicity and our enough experiences on the Delay-Line interferometer of TENKO-10, we developed the control system of TENKO-100 and verified its noise performance.

The most characteristic aspect of TENKO-100 is its 10 km optical path length. This is attained by 102 reflections of the beam between two suspended mirrors separated by 100.5 m in each arm. It is the longest laser interferometer in the world. Another important aspect is its attained strain sensitivity, 8×10^{-20} $1/\sqrt{\text{Hz}}$ around 1 kHz and 1.1×10^{-19} $1/\sqrt{\text{Hz}}$ typically which represents an improvement 30th times the sensitivity of TENKO-10. TENKO-10 was a Delay-Line laser interferometer which had 1 km optical path length provided by 102 reflections over 10 m base-line. Important characteristic of TENKO-100 performance is stable and effective operation of a new type absolute control system for the reduction of the scattered light noise in such a large scale interferometer, as well as verification of the various noise performance.

In chapter 2, gravitational waves derived from the General Relativity and their physical appearances are described. The current studies on gravitational wave sources and expected scientific outputs from observations of gravitational waves are also introduced. In chapter 3, different types of practical gravitational wave detectors are presented, especially interferometric detectors which are popular gravitational wave detectors in future. Focus is placed on the signal readout to detect the effect of gravitational waves with interferometric detectors and on such folding techniques as the Delay-Line type and the Fabry-Perot type to obtain long optical path length within practical arm length. Chapter 4 explains the fundamental construction of TENKO-100 as a Delay-Line laser interferometric gravitational wave detector with the targeted strain sensitivity of 2×10^{-20} $1/\sqrt{\text{Hz}}$ at 100 Hz. In chapter 5, different types of obstructive noise sources and their expected behavior in TENKO-100 are discussed, and analyzed experimentally with TENKO-100. In addition, the principles and experimental apparatus of noise reduction techniques to eliminate their contributions in the sensitivity are explained, and their performances are studied. Chapter 6 provides the best attained strain sensitivity of TENKO-100 in frequency. The possible dominant noise sources are explained for each frequency range. In Chapter 7, summaries and problems of TENKO-100 performance are discussed for the improvement of the current system and for the more stable operation as a gravitational wave detector in future.

Chapter 2

Gravitational Waves in General Relativity

2.1 Gravitational Waves

2.1.1 Linearized Einstein's Field Equation

As the electromagnetic wave solution is deduced from electromagnetic field equation, a wave solution can be deduced from the linearized Einstein's field equation just analogously, which is so-called as gravitational wave. According to the General Theory of Relativity, the metric tensor $g_{\mu\nu}$ is related with Einstein's field equation as follows

$$R_{\mu\nu} - \frac{1}{2} R g_{\mu\nu} = \kappa T_{\mu\nu} \quad , \tag{2.1}$$

where

$T_{\mu\nu}$	:	Energy-momentum tensor
$R_{\mu\nu}$	:	Ricci curvature tensor
R	:	Curvature scalor
κ	:	Einstein's gravitational constant

where $R_{\mu\nu}$ and R are defined in accordance to the contraction of 4 parameter curvature tensor $R_{\alpha\beta\mu\nu}$,

$$R \equiv g^{\mu\nu} R_{\mu\nu} \quad , \tag{2.2}$$

$$R_{\mu\nu} \equiv R^{\alpha}_{\nu\mu\alpha} = \partial_\mu \Gamma^{\alpha}_{\alpha\nu} - \partial_\alpha \Gamma^{\alpha}_{\mu\nu} + \Gamma^{\alpha}_{\mu\tau} \Gamma^{\tau}_{\nu\alpha} - \Gamma^{\alpha}_{\alpha\tau} \Gamma^{\tau}_{\mu\nu} = R_{\nu\mu} \quad , \tag{2.3}$$

$$\Gamma^{\lambda}_{\mu\nu} \equiv \frac{1}{2} g^{\lambda\rho} \left(-\partial_\rho g_{\mu\nu} + \partial_\mu g_{\nu\rho} + \partial_\nu g_{\rho\mu} \right) \quad , \tag{2.4}$$

and κ is given by

$$\kappa = \frac{8\pi G}{c^4} \quad . \tag{2.5}$$

G : Universal gravitational constant $= 6.672 \times 10^{-11}\ [\mathrm{Nm^2/kg^2}]$
c : Speed of light $= 2.998 \times 10^{8}\ [\mathrm{m/s}]$

Eq. 2.1 shows a nonlinear equation. Although analytic solution for the nonlinear equation is difficult in general, we can obtain an approximate solution for the metric tensor $g_{\mu\nu}$ that has small metric perturbation $h_{\mu\nu}$ from the metric tensor of Minkowski space-time $\eta_{\mu\nu}$, *i.e.* flat space-time

$$g_{\mu\nu} = \eta_{\mu\nu} + h_{\mu\nu} \quad , \tag{2.6}$$

$$\eta_{\mu\nu} = \begin{bmatrix} -1 & 0 & 0 & 0 \\ 0 & 1 & 0 & 0 \\ 0 & 0 & 1 & 0 \\ 0 & 0 & 0 & 1 \end{bmatrix} \quad . \tag{2.7}$$

In addition, we define pseudo-tensor ϕ to simplify the Einstein's field equation, as the following :

$$\phi_{\mu\nu} = h_{\mu\nu} - \frac{1}{2} h \eta_{\mu\nu} \quad , \tag{2.8}$$

$$h_{\mu\nu} = \phi_{\mu\nu} - \frac{1}{2} h \phi_{\mu\nu} \quad , \tag{2.9}$$

$$h = h^{\alpha}_{\alpha} \quad . \tag{2.10}$$

This choice of metric satisfies gauge conditions

$$\frac{\partial}{\partial x^{\nu}} \phi^{\nu}_{\mu} = \frac{\partial}{\partial x^{\nu}} h^{\nu}_{\mu} - \frac{1}{2} \frac{\partial}{\partial x^{\mu}} h = 0 \quad . \tag{2.11}$$

Assuming that the proper gauge invariance is adopted, the Einstein's field equation can be linearized as follows

$$\Box \phi_{\mu\nu} = -\frac{16\pi G}{c^4} T_{\mu\nu} \quad . \tag{2.12}$$

Eq 2.12 is just the field equation of the gravitational field to produce gravitational waves.

2.1.2 Wave Solution of a Gravitational Wave

In vacuum, Eq 2.12 is simplified to

$$\Box \phi_{\mu\nu} = 0 \quad , \tag{2.13}$$

because $T_{\mu\nu} = 0$. On the assumption that a gravitational wave as a plane wave propagates along the z-axis (x^3) in rectangular coordinates, it is expressed with ten tensor factors of $\psi_{\mu\nu}$ as follows

$$\phi_{\mu\nu} = \psi_{\mu\nu} e^{ik(-x^0 + x^3)} \quad , \tag{2.14}$$

where k is a wavenumber. By choosing the Transverse Traceless Gauge Transformation (TT), $\phi_{\mu\nu}$ is simplified to

$$\phi_{\mu\nu} = \begin{bmatrix} 0 & 0 & 0 & 0 \\ 0 & \psi_{11} & \psi_{12} & 0 \\ 0 & \psi_{12} & -\psi_{11} & 0 \\ 0 & 0 & 0 & 0 \end{bmatrix} e^{ik(-x^0 + x^3)} \quad , \tag{2.15}$$

with two independent parameters, ψ_{11} and ψ_{12}. The correspondent metric perturbation $h_{\mu\nu}$ is given by

$$h_{\mu\nu} = \begin{bmatrix} 0 & 0 & 0 & 0 \\ 0 & \psi_{11} & \psi_{12} & 0 \\ 0 & \psi_{12} & -\psi_{11} & 0 \\ 0 & 0 & 0 & 0 \end{bmatrix} e^{ik(-x^0 + x^3)} \quad . \tag{2.16}$$

This indicates that waves are transverse wave traveling with the speed of light and have two polarization states shown in Figure 2.1 as follows

$$\begin{bmatrix} 0 & 0 & 0 & 0 \\ 0 & h_+ & 0 & 0 \\ 0 & 0 & -h_+ & 0 \\ 0 & 0 & 0 & 0 \end{bmatrix} \quad \text{and} \quad \begin{bmatrix} 0 & 0 & 0 & 0 \\ 0 & 0 & h_\times & 0 \\ 0 & h_\times & 0 & 0 \\ 0 & 0 & 0 & 0 \end{bmatrix} \quad . \tag{2.17}$$

2.1.3 Generation of Gravitational Waves

In analogy to electromagnetic theory, I will develop the theoretical frame-work for generation of gravitational waves. In electromagnetism, the leading-order multi-pole radiation

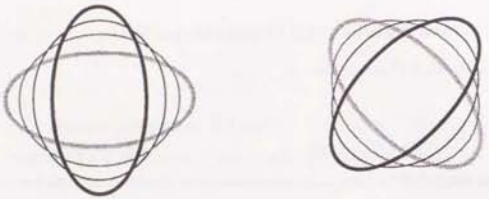

Figure 2.1: Gravitational wave polarization

from a non relativistic charge distribution is the dipole radiation. The Lorentz-gauge vector potential in the wave zone is [17]

$$A_j(t,\mathbf{x}) = \frac{1}{cr}\dot{d}_j\left(t-\frac{r}{c}\right) \quad . \tag{2.18}$$

where $r \equiv |\mathbf{x}|$ and $\mathbf{d}$ is the electric dipole moment. The $1/r$ electric and magnetic fields computed from Eq 2.18 depend only on the components of $\mathbf{d}$ transverse to the propagation direction $\mathbf{n} = \mathbf{x}/r$.

We can replace therefore d_j in Eq 2.18 by its transverse part

$$d_j^T = P_{jk}d_k \quad , \tag{2.19}$$

where P_{jk} is the projection tensor defined by

$$P_{jk} \equiv \delta_{jk} - n_j n_k \quad . \tag{2.20}$$

Substituting the $\mathbf{E}$ and $\mathbf{B}$ fields into the Pointing vector, the formula of the angular distribution of energy flux is obtained by

$$\frac{d^2E}{dtd\Omega} = \frac{1}{4\pi c^3}\ddot{d}_j^T\ddot{d}_j^T \quad . \tag{2.21}$$

If we choose the z-axis along $\mathbf{n}$, we can easily integrate Eq 2.21 over solid angles to obtain

$$\frac{dE}{dt} = \frac{2}{3c^3}\ddot{\tilde{d}}_j\ddot{\tilde{d}}_j \quad . \tag{2.22}$$

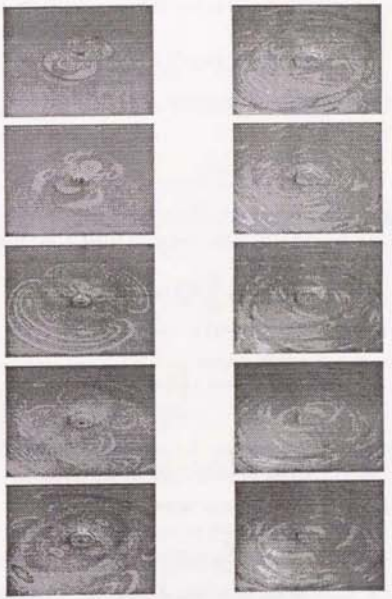

Figure 2.2: Gravitational wave polarization from black hole collision (quoted from NASA Relativity Group : *http:\\ jen-luc.ncsa.uiuc.edu/Movies/movies.html*)

Now, in the case of gravitational radiation, the dipole moment vanishes due to the conservation law of momentum as follows

$$\ddot{\vec{d}}_j = \sum_A m_A \ddot{x}_j^A = \sum_A \dot{p}_j^A \approx 0 \quad . \tag{2.23}$$

In analogy to the case of electromagnetism, the "mass magnetic dipole moment" is,

$$\mu \equiv \frac{1}{c}\sum_A \mathbf{x} \times \left(m_A \dot{\mathbf{x}}^A\right) = \frac{1}{c}\sum_A \mathbf{j}^A \quad , \tag{2.24}$$

where $\mathbf{j}^A$ is the angular momentum of the particle. By the conservation of angular momentum

$$\dot{\mu} = 0 \quad . \tag{2.25}$$

There is no magnetic dipole radiation, but electric quadrupole radiation appears. From the analog of Eq 2.18, the next order is the quadrupole radiation expressed in

$$h_{jk}^{TT}(t,\mathbf{x}) = \frac{2G}{rc^4}\ddot{I}_{jk}^{TT}\left(t-\frac{r}{c}\right) \quad , \tag{2.26}$$

where I_{jk}^{TT} is the mass quadrupole moment :

$$I_{jk}^{TT} \equiv P_{jk}P_{km}I_{lm} - \frac{1}{2}P_{jk}\left(P_{lm}I_{lm}\right) \quad , \tag{2.27}$$

where

$$I_{jk} = \sum_A m_A\left[x_j^A x_k^A - \frac{1}{3}\delta_{jk}\left(x^A\right)^2\right] \quad . \tag{2.28}$$

The energy flux is given by the stress-energy tensor

$$T_{0r} = \frac{c^4}{32\pi G}\left\langle \dot{h}_{jk,0}^{TT}\dot{h}_{jk,r}^{TT}\right\rangle \quad . \tag{2.29}$$

Substituting Eq 2.26, we obtain the distribution of energy flux of quadrupole radiation

$$\frac{d^2E}{dtd\Omega} = \frac{1}{8\pi}\frac{G}{c^5}\left\langle \ddot{I}_{jk}^{TT}\ddot{I}_{jk}^{TT}\right\rangle \quad . \tag{2.30}$$

Integrating over n, we get

$$L_{GW} = \frac{G}{5c^5}\left\langle \dddot{I}_{jk}\dddot{I}_{jk}\right\rangle \quad . \tag{2.31}$$

Thus, we can understand that gravitational waves cannot be radiated from symmetrical motion of sources and that astronomical asymmetrical motions would be very reliable sources for detectable gravitational waves.

2.1.4 Effect on a Free Falling Point Mass

The motion equation of a point mass perturbed only by gravity (so-called free falling mass), is given by the geodesic equation, *i.e.*

$$\frac{dx^\alpha}{d\tau^2} + \Gamma_{\mu\nu}^\alpha \frac{dx^\mu}{d\tau}\frac{dx^\nu}{d\tau} = 0 \quad , \tag{2.32}$$

where x^α, $\Gamma_{\mu\nu}^\alpha$ are the four vectors of a point mass and the Christoffel Symbol, respectively. Assuming that the velocity of the mass $\ll c$ and $dx^\alpha/d\tau = (-c,0,0,0)$, Eq 2.32 is simplified to

$$\frac{d^2x^\alpha}{d\tau^2} + c^2\Gamma_{00}^\alpha = 0 \tag{2.33}$$

In the case of a weak gravitational wave expressed in Eq 2.15, Eq 2.33 is just

$$\frac{d^2x^\alpha}{d\tau^2} = 0 \quad . \tag{2.34}$$

This shows that the effect of a gravitational wave cannot be observed with a single test mass. To detect the effect of a gravitational wave, we should investigate the deviation of geodesics of masses.

We define X^α as the relative displacement vector between two point masses, x^α and $x^\alpha + \xi^\alpha$. This satisfies the geodesic equation as follows

$$\frac{d^2X^\alpha}{d\tau^2} + R_{\mu\nu\beta}^\alpha \frac{dx^\mu}{d\tau}\frac{dx^\nu}{d\tau}X^\beta = 0 \quad , \tag{2.35}$$

with

$$\frac{dx^\alpha}{d\tau} = 0 \quad . \tag{2.36}$$

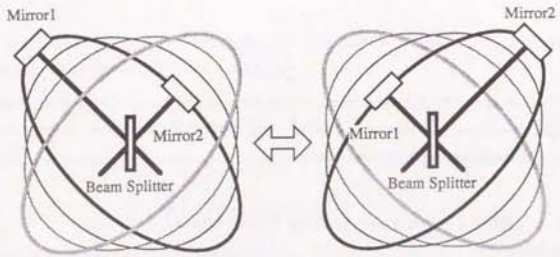

Figure 2.3: Mass motion perturbed by the most effectively polarized gravitational wave

Accordingly

$$\frac{d^2\xi^\alpha}{d\tau^2} + R^\alpha_{\mu\nu\beta}\frac{dx^\mu}{d\tau}\frac{dx^\nu}{d\tau}X^\beta = 0 \quad . \tag{2.37}$$

In the approximation that velocity$\ll c$ and $\xi^0 = 0$, we obtain

$$\ddot{\xi}_i = \frac{1}{2}\sum_{j=1}^{3}\ddot{h}_{ij}X_j \quad . \tag{2.38}$$

This shows that the distance perturbation between two point masses changes in proportional to the distance between point masses for the proper polarized gravitational wave.

2.1.5 Effects of Gravitational Waves in Interferometric Gravitational Wave Detectors

The change of the distance between two point masses due to a gravitational wave can be detected by the change of phase for a coherent beam of photons traveling between two point masses. To simplify, we set two point masses at (0,0,0) and (ℓ,0,0), and take the gravitational wave propagating along the z-axis with $h_{12} = h_{21} = 0$, $h_{11} = h_{22} = h(t)$. The proper distance of a photon is then given by,

$$ds^2 = -c^2t^2 + (1 + h(t))\,dx^2 = 0 \quad . \tag{2.39}$$

The time, Δt_x to trip between two point masses satisfies

$$\int_{t-\Delta t_x}^{t}\left(1 - \frac{1}{2}h(t')\right)\,cdt' = 2\ell \quad . \tag{2.40}$$

Accordingly, we obtain

$$\Delta t_x = \frac{2\ell}{c} + \int_{t-\frac{2\ell}{c}}^{t}\frac{1}{2}h(t')\,cdt' \quad . \tag{2.41}$$

In this formula, the second term shows the excess time of the traveling photon due to the gravitational wave's perturbation, which is namely the effect of the gravitational wave. In an interferometric gravitational wave detector, we can obtain double amplitude of the signal by interfering both photons because the time perturbation appears inversely due to the orthogonality of the two optical paths as shown in Figure 2.3.

2.2 Gravitational Wave Sources

Various gravitational wave sources and their strain amplitudes were estimated and are shown in Table 2.1.

2.2.1 Coalescing Binary Compact Stars

It is expected that a lot of binary systems with only one compact star (a white dwarf, a neutron star and a black hole) will form because almost all of stars in our universe form binary systems. Although they can radiate gravitational waves at a frequency equal to twice the orbital frequency, *e.g.* 10^{-4} Hz [19] due to the rotation of binary systems, it is so weak, *e.g.* $h \sim 10^{-23}$ on the Earth that they hardly coalesce due to the energy loss of the gravitational wave radiation within the age of our universe.

On the hand, a few of them may evolve to binary systems with two compact binary systems, such as PSR1913+16, PSR2127+11C and PSR1534+12 in our galaxy. These binary systems can coalesce with huge gravitational wave radiation ($h \sim 10^{-18}$) within the age of

Sources of GW	Frequency	Strain	Event Rate	Detection
Coalescing Binary Neutron Stars ($\leq$ 200MPC)	10Hz ~1kHz	10^{-21}	3 / year	Interferometer Template
Super Novae (Milky Way)	~1kHz	10^{-18}	$3 \sim 1$ / Century	Interferometer Resonant Detector
Super Novae (Virgo Cluster)	~1kHz	10^{-21}	$3 \sim 1$ / year	Interferometer
Black Hole Generation	~1mHz	10^{-17}	1 / year	Space Interferometer
Pulsars	10Hz ~1kHz	10^{-25}	Periodic	Interferometer Resonant Detector
Cosmic Strings	$\sim 10^{-7}$	10^{-15}	Stochastic	Pulsar Timing

Table 2.1: Sources of gravitational waves [18, 20, 26]

the universe, *e.g.* 3.5×10^8 years, 2×10^8 years and 30×10^8 years, respectively [20]. According to detailed simulations, a sinusoidal chirp wave, *e.g.* 100 Hz~1kHz quasi-sinusoidal wave, is radiated during the last 3 minutes before coalescence and burst wave, *e.g.* $\sim$ kHz during the last millisecond. Burst signals are the most reliable and detectable gravitational wave signals.

The expected event rate of the coalescence of binary systems within 200 Mpc which includes the Virgo cluster is about three per year. The expected strain amplitudes is $h = 10^{-21}\, 1/\sqrt{\text{Hz}}$ [21]. This is just detectable with full-scale interferometric gravitational wave detectors with km base-line using a technique of a matched filter.

2.2.2 Supernova Explosions

During the final process in the life cycle of a star, it collapses due to its gravitational force to a compact star and outer layers are dramatically exploded out, which is a process known as supernova explosion. Its violent gravitational collapse may be one of the most reliable source of burst like gravitational waves. In general, the calculated strain amplitude of gravitational waves from supernovae is given by [18]

$$h_{GW} = 1.6 \times 10^{-21} \left[\frac{E_{GW}}{10^{-2} M_\odot c^2}\right]^{\frac{1}{2}} \left[\frac{f}{1\text{kHz}}\right]^{-1} \left[\frac{\tau}{1\text{m sec}}\right]^{-\frac{1}{2}} \left[\frac{r}{15\text{Mpc}}\right]^{-1} \quad . \tag{2.42}$$

E_{GW}	:	Energy of a gravitational wave	$[M_\odot c^2]$
f	:	Frequency of a gravitational wave	[kHz]
τ	:	Time of observation	[msec]
r	:	Distance between a gravitational wave source and the earth	[Mpc]

However, since a symmetrical explosion never produces a gravitational wave due to the phase cancellation of the gravitational wave itself, its source star should have rotational angular momentum which produces asymmetrical gravitational collapse. Unfortunately, observations of the rotational period of neutron stars which provide the angular momentum before explosions support almost symmetrical process of gravitational collapse [22]. According to simulations [23], the estimated energy of gravitational waves from supernova explosions of a rotating star is given by,

$$E_{GW} \leq 10^{-7} M_\odot c^2 \quad . \tag{2.43}$$

This produces a strain amplitude $h \leq 10^{-20}$ on the Earth, if it is radiated in our galaxy. If it is radiated at 15Mpc nearer in the Virgo cluster which includes $\sim$ 3000 galaxies, a strain amplitude is $h \leq 10^{-23}$, which is too small to be detected.

If the angular momentum is much larger, the core forms a massive asymmetrical ring with a piece of small cores. When they coalesce again, huge gravitational waves with 1 % of the total released energy is expected to be radiated. They produce $h \leq 10^{-21}$ strain amplitude which is within a sensitivity of full scale interferometers [24, 25] if radiated within 20 Mpc. They produce strain amplitudes of $h \leq 10^{-22}$ within 60 Mpc where more than 1000 supernovae per a year in "star burst galaxies" are expected. However, such calculations have so much uncertainties that they make it likely that the strain amplitudes from supernovae will change in future.

2.2.3 Pulsars

A pulsar is a compact star noted for its extraordinarily precise and relatively fast sweep of electromagnetic wave or X-ray radiation alike the sweep of a search light from a lighthouse.

If the pulsar has a slight geometrical asymmetrical dip on it, it can radiate continuous gravitational waves. The frequency of the gravitational wave is twice the rotational frequency of the pulsar and its strain amplitude is given by the upper limitation of spin down of the pulsar. For example, Crab pulsar away 2 kpc is expected to radiate continuous 60 Hz gravitational waves and its strain amplitude is estimated to be $h \leq 10^{-25}$ [26]. We can enhance this signal to noise ratio by the data integration because we know its precise rotational period.

2.2.4 Stochastic Background Radiation

According to the cosmic string scenario, if strings had provided the seeds around which galaxies condensed, their decay might have produced a gravitational wave background. The expected strain amplitude of the background gravitational waves is given by

$$h_{GW} = 1.8 \times 10^{-25} \left[\frac{f}{100\mathrm{Hz}}\right]^{-\frac{1}{2}} \left[\frac{B}{2\mathrm{Hz}}\right]^{\frac{1}{2}} \left[\frac{\rho_{GW}}{10^{-8}}\right]^{-\frac{1}{2}} \left[\frac{H_0}{100\mathrm{kmMpc}^{-1}s^{-1}}\right] \quad . \tag{2.44}$$

B : Band width
ρ_{GW} : Energy density of a gravitational wave
H_0 : Hubble constant

Since the typical frequency is below 1 Hz, the interferometric detectors cannot observe stochastic background. Other techniques, such as pulsar tracking method or doppler tracking method [27, 28, 29] can observe it.

2.3 Scientific Outputs from Gravitational Wave Observations

Gravitational waves certainly provide us with a new channel to observe the universe which is hardly observed by such present methods as visible light, Ultra-violet light, infrared light, optical, X-rays and γ-ray and so on.

If we construct km-class interferometers and detect gravitational waves, we will obtain the following knowledge [18],

- Verification of the General Theory of Relativity
  The detection of gravitational waves will help to sort out the many gravity theories which are consistent with all to date measured property of gravitational waves. Three detectors enable us to obtain complete information about gravitational waves such as propagation direction, polarization, amplitude, speed and so on.

- Determination of Hubble Constant
  The observation of gravitational radiation from a few coalescence binaries within 100 Mpc per year will allow a determination of Hubble constant with a few % accuracy. This is due to the reliability of such observations to yield accurate proper distances.

If we can observe the shapes of gravitational waves, we can deduce the following knowledge.

- Study of the Strong Gravitational Field
  The observation of gravitational waves will help the study of the strong gravitational field. Informations about mass, spin, total angular momentum of massive stars of binary systems will be investigated.

- Knowledge of the Supernova Mechanism
  The internal mechanism of supernova explosions is only practically observable through gravitational waves in contrast to electromagnetic waves. Such observations give informations about the energy ratio of stellar objects used for gravitational wave radiations, the production of neutron stars or black holes, the contribution of rotational angular momentum to the generation of gravitational waves, and the upper limit of neutron star mass.

If we can observe gravitational waves in enough low frequency range with the future advanced detectors, we will obtain the following

- Understanding the Early Universe
  In most cosmological models, remnants of the early universe in the form of the stochastic background gravitational wave radiation is predicted. Extracting this stochastic signal would give a great information about the early universe and allow us to retrace to the Big Bang.

In addition, the detection technique for gravitational waves is equivalent with the technique to observe the relative scale of 10^{-23} which has never been detected in human history. It is historical advancement in physics.

Chapter 3

Gravitational Wave Detectors

In this section, I explain different types of gravitational wave detectors. One of them is a resonant-type detector and the other is an interferometric detector which has been becoming popular for gravitational wave detectors. Especially, we explain two types interferometric detectors, *i.e.* the Fabry-Perot type and the Delay-Line type, and characteristics of each type such as frequency response and technical demands for a km-class interferometer.

3.1 Resonant-Type Gravitational Wave Detectors

The first generation of practical gravitational detectors was a resonant-type detector by J.Weber [10]. It was based on the principle of detecting gravitational waves through internal elastic resonances of an isolated cylindrical bar made of aluminum with high mechanical Q value. The high Q value enhances the amplitude of its excited elastic resonance whose frequency is set around gravitational wave frequencies. In this way, detectable gravitational wave frequencies are limited to the resonant frequencies of the bar and the sensitivity is limited by one of quantum nature, *i.e.* thermal noise. Present second-generation resonant-type detectors, listed up in Table 3.1 [30], use transducer (TRD) to detect resonances and they are cooled below several Kelvin to minimize the contributions of thermal noise [31]. Presently, a detector with a resonant Fabry-Perot transducer, whose one of mirrors is set on the resonant bar and the other is outside, is in development [32] and it will be expected to provide comparable sensitivity with cryogenic resonant-type detectors even

at room temperatures. For example, a resonant-type detector which targets continuous gravitational radiation from the crab pulsar estimated to radiate at the extraordinarily precise frequency of 60 Hz is under development.

Although the present resonant-type detectors have performances superior to the prototype interferometric detectors, both in stable long term operation keeping high sensitivities and in the attained sensitivities, the future interferometric detectors are expected to outperform them in their final stage.

3.2 Laser Interferometric Gravitational Wave Detectors

Gertsenshtein and Poustvoit at Moscow State University [33] proposed an interferometric scheme to detect the effect of gravitational waves as the optical path difference of coherent photon beams traveling two orthogonal paths in a Michelson-Morley interferometer, and Weiss at MIT [34] was the first to develop a practical interferometer for a gravitational wave detector and MPIQ (Billing) and Glasgow (R.P.Drever) followed it. One great advantage of the interferometric approach is that a signal due to gravitational waves can be increased with longer optical path length. Its sensitivity is principally limited by the shot noise of photons due to quantum nature, but it can be also improved by high power laser (refer in Chapter 4 and 5). Practically, many stabilization systems for the laser and seismic noise isolation systems are needed to reach the shot noise level (detailed later).

The present laser interferometric detectors are listed in Table 3.2. The most difference between these detectors is the folding technique for the optical path, one is an optical delay-line (namely Delay-Line type) and the other is a Fabry-Perot cavity (namely Fabry-Perot type) . The 40 m Fabry-Perot interferometer at Caltech built by R.P.Drever has the sensitivity 8×10^{-21} $1/\sqrt{}$ Hz at 500 Hz attained with Locked Fabry-Perot style. To date, this is the best sensitivity for the laser interferometric detectors in the world.

In Japan, the 20 m Fabry-Perot interferometer is developed in NAO using a Recombined style which is an indispensable technique for km-class interferometers contrasted to the Locked Fabry-Perot style which cannot be applied for the future interferometer design including the recycling technique. The 100 m Delay-Line laser interferometer TENKO-

Group	Antenna	Transducer	Sensitivity
CERN (ROME)	AL5056, 2.3t, 2.6K	Capacitive + SQUID	7×10^{-19}
CERN (NAUTILUS)	AL5056, 2.3t, 0.1K	Capacitive + SQUID	2×10^{-18}
Louisiana.S.U (USA)	AL5056, 1.1t, 4.2K	Inductive + SQUID	7×10^{-19}
Stanford.U (USA)	AL6061, 4.8t, 4.2K	Inductive + SQUID	10^{-18}
West Australia (Aust)	NB, 1.5t, 5K	RF Cavity	9×10^{-19}
ICRR (Japan)	AL5056, 1.7t, 300K	Laser TRD	-
KEK (Japan)	AL5056, 1.2t, 4.2K	Capacitive + FET	4×10^{-22} 60Hz

Table 3.1: Current Resonant-type Gravitational Wave Detectors [30]

Group	Base-Line	Folding Type	Sensitivity
Caltech (USA)	40 m	Locked Fabry-Perot	8×10^{-21}
Glasgow	10m	Locked Fabry-Perot	5×10^{-20}
NAO (Japan)	20 m	Recombined Fabry-Perot	5×10^{-18}
TOKYO (Japan)	3 m	Recombined Fabry-Perot	10^{-15}
MPIQ (Germany)	30 m	Delay-Line	1×10^{-19}
ISAS (Japan)	100 m	Delay-Line	1×10^{-19}

Table 3.2: Current prototype Laser Interferometric Gravitational Wave Detectors

100 at ISAS has the longest optical path ($\sim$ 10 km) in the world. TENKO-100 has the sensitivity, 8×10^{-20} $1/\sqrt{}$ Hz and typically 1.1×10^{-19} $1/\sqrt{}$ Hz around 1 kHz.

3.3 Principle of the Michelson Interferometer

3.3.1 Optical Signal Readout System of the Michelson Interferometer

The propagation time of coherent photons perturbed by a gravitational wave with an optimum polarization makes inverse phase shift for two orthogonal optical paths as mentioned in Chapter 1. A Michelson laser interferometer was proposed to detect "ripples of space-time" due to gravitational waves as shown in Figure 3.1.

Country	Project	Base-Line	Type	Schedule
USA (Caltech & MIT)	LIGO	two 4 km	FP	1998
Italy & France	VIRGO	3 km	FP	1998
Germany & England	GEO	600 m	Dual Recycling	1998
Japan	TAMA	300 m	FP	1998

Table 3.3: Current Projects for Gravitational Wave Observation

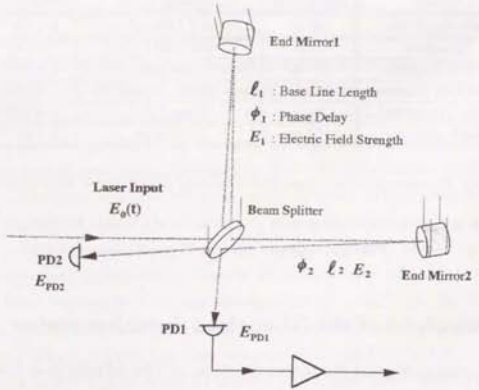

Figure 3.1: The principle of the Michelson interferometer

The basic Michelson interferometer consists of one beam splitter (BS) and two end mirrors (EM1, EM2) which are suspended to act as free-masses at higher frequencies above the pendulum resonant frequencies. A coherent laser beam is divided in orthogonal directions by the BS with a half in power and these two beams are recombined at the BS again after a round trip between the BS and the EM. The effect of a gravitational wave appears as phase perturbation in each optical path. This leads to power fluctuations of the recombined beam and it is detected as the fluctuation of the photo-current of two complementary photo-detectors set at the output ports of the interferometer (PD1, PD2).

To calculate the output photo-current due to relative phase difference of traveling photons, we take the electric field strength of the injection beam to be E_0, and assume it is divided perfectly half in power by the BS without any loss. The electric field strength of traveling beams are set as E_1 and E_2, and their phase delays due to the round trip are taken as ϕ_1 and ϕ_2. Then, each electric field strength of the recombined laser at either output port, the PD1 and the PD2, is given by

$$E_{PD1,PD2} = E_1 e^{-i\phi_1} \pm E_2 e^{-i\phi_2} \quad , \tag{3.1}$$

where the each phase at the PD1 and the D2 is different by π. Each output photo-current is given by

$$I_{PD1,PD2} \propto E_{PD1} E^*_{PD1} = E_1^2 + E_2^2 \pm 2E_1 E_2 \cos(\phi_1 - \phi_2) \quad , \tag{3.2}$$

defining the contrast K as follows

$$K = \frac{2E_1 E_2}{E_1^2 + E_2^2} = \frac{I_{\max} - I_{\min}}{I_{\max} + I_{\min}} \quad . \tag{3.3}$$

Eq 3.2 becomes

$$I_{PD1} \propto \frac{I_0}{2}(1 \pm K\cos(\phi_1 - \phi_2)) \quad . \tag{3.4}$$

This indicates that the output signals of both ports have complimentary phase, in other words, if the PD1's fringe is dark, the PD2's fringe is bright.

Eq 3.4 was expanded on the assumption that $K = 1$, *i.e.* perfect contrast

$$I_{PD1} \propto \frac{I_0}{2}(1 + \cos\Phi_0 - \sin\Phi_0\Delta\phi + \cdots) \quad , \tag{3.5}$$

where $\phi_1 - \phi_2 = \Phi_0 + \Delta\phi$, Φ_0 is the stationary relative phase difference and $\Delta\phi$ is the phase difference due to the perturbation of gravitational waves. To the first order, $\Delta\phi$ corresponds to the gravitational wave signal, while the square root of DC current is the noise which will be discussed in the later section. Thus, the signal to noise ratio is given by

$$\left(\frac{S}{N}\right)_{PD1} = \sin\left(\frac{\Phi_0}{2}\right)\sqrt{\frac{I_0}{2e}} \quad . \tag{3.6}$$

3.3.2 Phase Perturbation due to a Gravitational Wave

To simplicity, assume that an interferometer is orientated along the x-axis and the y-axis with both arm length, ℓ_x and ℓ_y, where $\ell_x \approx \ell_y = \ell$. We also assume that the optimum polarized gravitational wave with strain amplitude $h(t)$ passes along the z-axis. The proper distance of a photon beam satisfies the following equation :

$$ds^2 = -c^2dt^2 + (1 + h(t))\,dx^2 \quad . \tag{3.7}$$

In the case of photons, ds equals to zero. Thus, photons traveling along the x axis satisfy the equation

$$\frac{2\ell_x}{c} = \int_{t_x}^{t} \frac{1}{\sqrt{1 + h(t')}} dt' \approx \int_{t_x}^{t} \left(1 - \frac{1}{2}h(t')\right)\, dt' \quad . \tag{3.8}$$

Then, the phase delay $\phi_x(t)$ is given by

$$\phi_x = \Omega t_x = \Omega\left(t - \frac{2\ell_x}{c} - \frac{1}{2}\int_{t-2\ell_x/c}^{t} h(t')\, dt'\right) \quad . \tag{3.9}$$

where Ω is an angular frequency of the beam.

In the same manner except the inverse effect of the gravitational wave, the phase delay, $\phi_y(t)$, for photons traveling along the y-axis, is given by

$$\phi_y = \Omega t_y = \Omega\left(t - \frac{2\ell_y}{c} + \frac{1}{2}\int_{t-2\ell_y/c}^{t} h(t')\, dt'\right) \quad . \tag{3.10}$$

The second term corresponds to the perturbation due to the gravitational wave. The relative phase difference, assuming $h(t) = h_0 \sin(\omega t)$, is given by

$$\Delta\phi = \Omega(t_x - t_y) = 2h_0\frac{\Omega}{\omega}\sin\omega\left(t - \frac{\ell}{c}\right) \quad , \tag{3.11}$$

where we use $\ell_x \approx \ell_y = \ell$.

If the period of the gravitational wave is small enough with respect to the traveling time (or storage time), the strain amplitude can be regarded to be constant during a Delay-Line trip. Then, Eq 3.11 becomes

$$\Delta\phi_{(T_{GW} \le ST)} = \Omega\frac{2\ell}{c}h_0 \quad , \tag{3.12}$$

and, it can be represented by the shadow area in Figure 3.2 (a).

E.q. 3.12 shows that the phase difference can be increased with a longer optical path length. However, if it is below twice the storage time, phase cancellation appears and the maximum phase difference decreases. For example, it is 1.8 times, the phase difference can be seen as shadow area in Figure 3.2 (c) If it is even, it disappears as shown in Figure 3.2 (d). If it is below the storage time, the residual difference from cancellation appears and is increased with a proper gravitational wave period again. The correspondent phase difference shown in Figure 3.2 (e,g) is clearly smaller than before. Furthermore, the derivative of such a maximized phase difference for the proper period of a gravitational wave is expected to be in proportional to the period of a gravitational wave, *i.e.* $1/\omega$. At the same time, vanishing points also appear if the period of the gravitational wave satisfies

$$\frac{\omega\ell}{c} = n\pi \quad . \tag{3.13}$$

3.3.3 Frequency Response to Gravitational Waves

In order to express the frequency response of a Michelson interferometer to gravitational waves, we consider the Fourier spectrum $h(\omega)$ for $h(t)$, given by

$$h(t) = \int_{-\infty}^{\infty} h(\omega)e^{i\omega t}\, d\omega \quad . \tag{3.14}$$

Then, relative phase perturbation due to the gravitational wave is expressed as follows

$$\Delta\phi_{GW}(t) = 2\Omega\int_{-\infty}^{\infty} \sin\left(\frac{\omega\ell}{c}\right)\frac{h(\omega)}{\omega}e^{-i\frac{\omega\ell}{c}}\, e^{i\omega t}dt \quad . \tag{3.15}$$

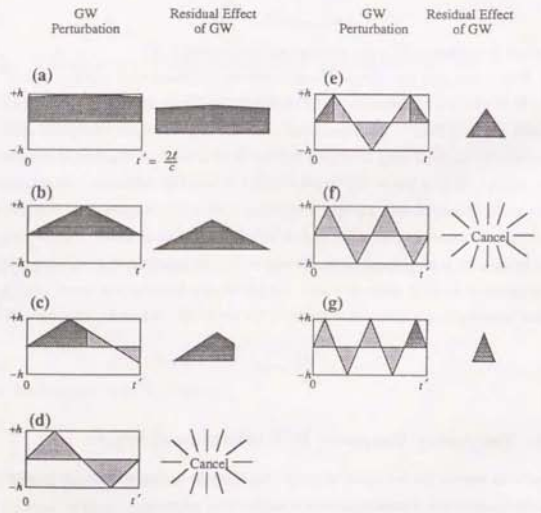

Figure 3.2: Cancellation of the phase perturbation due to a gravitational wave in a Michelson laser interferometer

At the same time, we define

$$\Delta\phi_{GW}(t) \equiv \int_{-\infty}^{\infty} \delta\phi(\omega)\, e^{i\omega t} d\omega \quad . \tag{3.16}$$

In this way, we can define the frequency response of a Michelson interferometer $H_M(\omega)$ as follows

$$\delta\phi(\omega) = H_M(\omega)\, h(\omega) \quad , \tag{3.17}$$

$$H_M(\omega) = \frac{2\Omega}{\omega} \sin\left(\frac{\omega\ell}{c}\right) e^{-\frac{i\omega\ell}{c}} \quad , \tag{3.18}$$

which behaves just as expected in Figure 3.2, and indicates the optimum choice of the arm length for the targeted gravitational wave's frequency, since too long arm length loses the sensitivity over the corner frequency. For example, if we intend to detect a gravitational wave with frequency below 1 kHz, we should set arm length around 75 km in accordance with Eq 3.18.

However, such a large interferometer would be hardly practical for a number of reasons : (1) the enormous vacuum chamber would be extremely costly, (2) the location site is quite hard to find (3) the localization of gravity at each mirror's locations becomes important. Many techniques to fold a long optical path length into a practical arm length of $3 \sim 4$ km have been proposed. All of these prototypes fall into two types, one is the Delay-Line type and the other is the Fabry-Perot type.

3.4 Delay-Line Type and Fabry-Perot Type

3.4.1 Frequency Response to Gravitational Waves

As a modification of Michelson interferometers, not only end mirrors (EM) but also near mirrors (NM) neighboring with a beam splitter are newly required for folded interferometers. One of techniques uses the optical delay-lines, which folds the optical path into successive reflecting light paths spacing with each other (detailed later). Then, the total optical path length of the optical delay-line, whose arm length is ℓ m and reflection number

is N, becomes $N \times \ell$ m. So, the frequency response of a Delay-Line interferometer is given by

$$H_{DL}(\omega) = \frac{2\Omega}{\omega} \sin\left(\frac{\omega N \ell}{c}\right) e^{-\frac{i\omega N \ell}{2c}} \quad . \tag{3.19}$$

For example, a Delay-Line interferometer with, $\ell = 4$ km and $N = 102$, reveals frequency response as shown by a solid curve in Figure 3.3 calculated from $|H_{DL}(\omega)|$

$$|H_{DL}(\omega)| = \frac{2\Omega}{\omega} \sin\left(\frac{\omega N \ell}{c}\right) \quad . \tag{3.20}$$

The other technique uses Fabry-Perot cavities, which has a resonant Fabry-Perot cavity constructed with the NM and the EM in each arm with reflecting light paths superimposed into the cavity axis. So, the reflected light from one arm consists of beams which have different storage time by multiples of one round trip and different amplitude by multiples of the product of reflectivity of the NM and the EM. As it were, the Fabry-Perot interferometer is an integration of Michelson interferometers with different arm length by one round trip. Hence, the frequency response of a Fabry-Perot interferometer can be deduced from integrated frequency response of simple Michelson interferometers. So, "gutters" seen in the Michelson type and the Delay-Line type are expected to be averaged smoothly. According to calculation, it is given by

$$H_{FP}(\omega) = \frac{2\alpha\Omega}{\omega} \sin\left(\frac{\omega \ell}{c}\right) e^{-\frac{i\omega \ell}{c}} \frac{1}{1 - r_1 r_2 \exp(-2i\omega\ell/c)} \quad . \tag{3.21}$$

$$\alpha = \frac{t_1^2 r_2}{(t_1^2 + r_1^2) r_2 - r_1} \quad , \tag{3.22}$$

where r_1, r_2 and t_1, t_2 are the reflectivities and transmittances of two mirrors, respectively.

For example, a Fabry-Perot interferometer with $\ell = 4$ km and $\mathcal{F}$=162, gives a frequency response as shown by a dotted curve in Figure 3.3 calculated from $|H_{FP}(\omega)|$

$$|H_{FP}(\omega)| = \frac{2\alpha\Omega}{\omega(1 - r_1 r_2)} \frac{|\sin(\omega\ell/c)|}{\sqrt{1 + F \sin^2(\omega\ell/c)}} \quad , \tag{3.23}$$

$$F = \frac{4 r_1 r_2}{(1 - r_1 r_2)^2} = \left(\frac{2\mathcal{F}}{\pi}\right)^2 \quad , \tag{3.24}$$

where $\mathcal{F}$ is called finesse, an important parameter for the performance of a Fabry-Perot cavity.

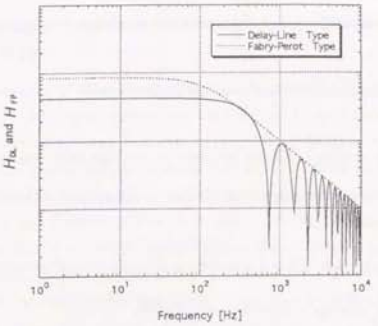

Figure 3.3: The frequency response of a Delay-Line Laser Interferometer and a Fabry-Perot Laser Interferometer

The reflection number, *i.e.* the folding parameter, of the Delay-Line type can be related to the Finesse of the Fabry-Perot type as follows

$$N = \frac{2\mathcal{F}}{\pi} \quad . \tag{3.25}$$

3.4.2 Comparison of the Fabry-Perot type and the Delay-Line type for km-class interferometers

In the scale of a 10m base-line interferometer, the remarkable advantages and disadvantages of the Fabry-Perot type and the Delay-Line type were not reported. Only the best sensitivities of each type revealed the difference of styles, *e.g.* $8 \times 10^{-21}\ 1/\sqrt{\text{Hz}}$ of the 40m Fabry-Perot interferometer in Caltech and $1 \times 10^{-19}\ 1/\sqrt{\text{Hz}}$ of the 30m Delay-Line interferometer in MPIQ. However, it is important to evaluate both performances and possibilities for the future km-class interferometer.

Some of the demands for a Fabry-Perot interferometer as a km-class interferometer follow as :

- The mirror size is 30 cm and high quality of roughness of mirror surface ($\lambda/30$) is needed.
- Lower contribution of the scattered light noise because of its superimposed beam path.
- The feedback topology is difficult and complex, but they have been recently overcome.
- It is difficult to match reflectivities of mirrors, and mirrors with extremely low loss $\leq 50ppm$ are needed.

On the other hand, some of the demands for a Delay-Line interferometer follow as

- The feedback topology is quite easy and simple.
- Various material can be good for mirrors.
- High contribution of the scattered light noise because of its separate beam paths. Not only the up-conversion noise (detailed in Chapter 5) but also the "non-stationary" scattered light noise is harmful.
- It needs big mirror size (60 cm) and extremely high quality of roughness of mirror surface ($\lambda/100$). Furthermore, it is quite difficult to match radii of mirror curvatures equally.

Historically, the Delay-Line type was developed ahead of the Fabry-Perot type and some of characteristics of the Delay-Line type are suitable for a km-class interferometer. However, the Fabry-Perot type was selected for the style of the future km-class interferometer such as LIGO project and VIRGO project based on the outcome of the 10m base-line Fabry-Perot interferometers. Thus, it is also important to verify characteristics of a Delay-Line interferometer with the equal base-line scale, and TENKO-100 took charge of verifying its characteristics in the 1/10 times scale of a km-class interferometer.

3.4.3 Ultimate Sensitivity of Interferometric Gravitational Wave Detectors

Ultimate sensitivity of a Fabry-Perot interferometric gravitational wave detector is shown in Figure 3.4 [35]. The frequency range less than about 100Hz are dominated by the seismic noise through suspending wires even after seismic noise isolation. To isolate the seismic noise contribution, various isolation systems such as the 7 layers pendulum (for VIRGO project), the stack (for LIGO project) and the super low resonant pendulum (for TAMA project) are proposed (detailed in Chapter 5 : Seismic Noise). The frequency range from 100Hz to several 100Hz are dominated by either pendulum thermal and internal thermal noise of test mass (detailed in Chapter 5 : Thermal Noise). To avoid the contribution of thermal noise, we should select material with high mechanical Q value for mirrors and should pay attention not to decrease their Q value with some components attached with them. The frequency range over several 100Hz are dominated by photon shot noise (detailed in Chapter 5 : Shot Noise). The shot noise level, in other words, signal to noise ratio, can be improved with higher laser power. However, it produces other problems such as thermal lensing effect and radiation pressure noise (detailed in Chapter 5 : Radiation Pressure Noise).

3.5 Other Types of Gravitational Wave Detection

Contrary to resonant-bar-type detectors and laser interferometric detectors which target gravitational waves with frequency about 100 Hz∼1 kHz, following detection styles target background gravitational waves with frequencies below 0.1 Hz.

One type of detectors uses pulsar timing, where gravitational waves were tried to be observed as the fluctuation of the arrival time of pulses radiated from pulsars and its time resolution was provided with the extraordinarily precise rotational periods of pulsars ($\Delta P/P \approx 10^{-8}$). At present, the H_2 maser used for the standard time limits its sensitivity $h \approx 10^{-14}\ 1/\sqrt{\ }$ Hz because its counting accuracy is lower than the period of the pulsar's pulse signal.

Another uses Doppler tracking, where gravitational waves were tried to be detected as Doppler shift of electromagnetic waves communicated between the earth and a satellite

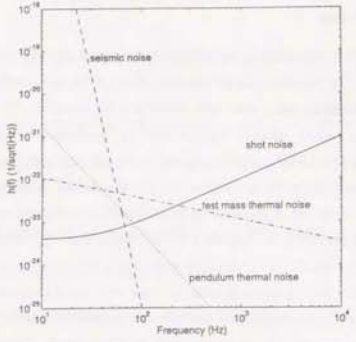

Figure 3.4: The ultimate sensitivity of interferometric gravitational wave detectors

in space. However, the fluctuation due to plasma in space was so dominant that it was difficult to detect gravitational waves with high sensitivity.

Future detection involves usage of a space interferometer (LISA in Europe), which has two drag free satellites at each arm end separated by 7.5 million km from two "near" satellites and they orbit behind the Earth with 20 degrees angle [36]. Instead of the optical reflection on end mirrors to complete a round trip, transponders equipped with end drag free satellites are used to transmit a laser beam locked in phase to the received laser beam from "near" satellites. The employment of detectors in space is a promising method to eliminate the seismic noise, and it should be sensitive to strong, however, low frequency gravitational waves.

Chapter 4

Construction of a 100m Delay-Line Laser Interferometer

In this chapter, We explain the fundamental construction of a 100m Delay-Line laser interferometer for a gravitational wave detector. We used a laser source as a coherent light source, and suspended mirrors to obtain quasi-free falling masses. 10 km optical path was attained with the optical delay-line path by folding it into 100 m base-line. To control the mirror position, the local control was used, and the darkfringe locking method with the internal modulation technique was used for the signal readout of gravitational waves.

4.1 Laser

The easiest method to enhance the sensitivity of an interferometric gravitational wave detector is to increase the laser light power stored in optical paths. We chose an argon ion gas laser as a light source for TENKO-100. One reasons for this choice was due to our great deal of experience and knowledge on the same type laser (produced by NEC) used as a frequency-tunable light source for TENKO-10. (TENKO-10 was the antecedent of TENKO-100 with a baseline of 10m, in the form of a Delay-Line laser interferometer with 102 reflections for a total optical path length of 1 km). Another reason for this choice was that it was one of the few commercially available high power laser that would realize the shot noise level, 2×10^{-16} m/$\sqrt{}$ Hz. The nominal specifications of the argon ion laser are shown in Table 4.1. This laser was model BeamLok 2080/85-25S produced by Spectra Physics Lasers which can provided 10 W light power at 514.5 nm. In practice, the

maximum laser power at 514.5 nm decreased to about 8 W as a result of miss-alignment caused by reforming the attachment mechanism of both front and rear mirrors for the frequency stabilization. A stable single frequency operation was achieved by a temperature-stabilized etalon inserted between the rear mirror and the laser tube (Etalon Lock). The transverse mode consisted of mainly TEM_{00}, with other higher modes mixed with beam jitter noise. The typical free-running frequency noise was 10^5 Hz/$\sqrt{}$ Hz under 100 Hz and fell to 1 Hz/$\sqrt{}$ Hz at 100 kHz due to a f^{-2} law. Although it was three orders of magnitude worse than the MISER which provided 700 mW infrared beam with 1064 nm wave length (invisible) used in the 20 m Fabry-Perot interferometer at NAO, it did not matter because it could be well stabilized easily to $\sim$ 100 mHz/$\sqrt{}$ Hz demanded for the most pessimistic mirror specifications that would provide $\sim$ 10 m optical path difference under the same re-entrance conditions (detailed in Chapter 5) in contrast to a Fabry-Perot interferometer which demanded much more frequency stability. Thus, we could trade laser beam noise for the high power of the laser without any loss of overall performance of the interferometer.

The practical environment of the laser was noisy. The laser tube and the front and the rear mirrors were fixed on an optical super-inver table, which rested on another bigger optical flat bench directly on the floor in the center room. In addition, the super-inver table was always oscillated by cooling water flow whose hose was connected to the laser tube. All local vibrations might be the source of the frequency noise, the intensity noise, and the geometrical beam jitter noise. It would be best to isolate the laser tube itself from the optical bench through isolation stack mechanics.

4.2 Optical Delay-Line Path

4.2.1 Folded Light Path

Another easy way to enhance the sensitivity of interferometric gravitational wave detectors is to lengthen the total optical path length as we saw in chapter 3. However, it is hardly practical or possible to build a simple Michelson interferometer with a long arm length, *e.g.* 500 km arm length with an optimum sensitivity of $\sim 10^{-22}$ 1/$\sqrt{}$ Hz at 200 Hz. That is because some techniques to fold a long optical path into a practical shorter length are indispensable. Of the two folding techniques, the optical delay-line technique

Output Characteristics		
	Nominal	Customize
Beam Diameter at 1/e Position	1.9 [mm]	-
Beam Divergence, Full Angle	45 [mrad]	-
Polarization (Vertical)	$\geq 100:1$	-
Cavity Length	1.71 [m]	1.90 [m]
FSR (Mode Spacing)	87 [MHz]	78.9 [MHz]
Noise	0.4% [rms]	-
Power Stability	1.0 %	-
Beam Position Stability		
position offset	≤ 0.5 [μ m / °C]	-
angular offset	≤ 5.0 [μrad]	-
Single Frequency Operation		
Temperature Range for Mode Hop	≤ 4 [°C]	-
Frequency Jitter	15 [MHz] ≤ 1 [sec]	-
Conversion Efficiency	$\geq 60\%$	-
Output Power		
Visible Multiline Power		
(454.5 [nm]~528.7[nm])	25 [W]	22 [W]
514.5 [nm]	10 [W]	8 [W]
Others		
Water Cooling	10 [°C] ~ 3 [°C]	-
Current Assumption	60 [A] (max 73 [A])	-
Voltage Assumption	480 [V]	-

Table 4.1: Specifications of the argon ion laser

was adopted in TENKO-100. One reason for this choice was that we already had a great deal of experience to study and to understand the control and various noise performance of the Delay-Line laser interferometer, *i.e.* TENKO-10. Another reason for this choice was that the almost of control systems and noise performances of the Delay-Line type were so simpler (detailed in later) except for the scattered light noise behavior than those for a Fabry-Perot type. Thus, it was expected to be relatively easy to obtain high sensitivity with the optical delay-line technique even if the scale factor of the base-line would increase by 10 times from TENKO-10 to TENKO-100. At the same time, however, we were afraid that the difficulty to make four main mirrors equally with such large spherical curvature of 100 m within the present polishing and coating technology would bring a problem such as optical path length difference of $\sim$ 10 m and that much more frequency stability would be required (detailed in later).

4.2.2 Ray Tracing of the Optical Delay-Line Path

The Herriot-Kogelnik-Kompfner type optical delay-line [37] used in TENKO-100 is one of the technique to lengthen the total optical path length within the limited practical arm length by allowing the laser beam to reflect at many times between two mirrors with the same spherical curvature radii (R m) separated by nearly the same distance (ℓ m) as their curvature radii (Figure 4.1).

In the case of the symmetrical optical delay-line, a small hole drilled out at 3 o'clock position in the near mirror allows the laser beam to enter the space between the two mirrors, and it hit and reflects at 6 o'clock position on the end mirror. This reflected beam goes back to the near mirror and is focused at 9 o'clock position in the near mirror and re-reflected beam goes to 12 o'clock position and re-focused on the end mirror. If the distance between the two mirrors ℓ m is selected properly, the beam reflected from 12 o'clock on the end mirror is focused slightly upon the entrance hole. According to this rule, the beam spots on both mirror surfaces lie on a circle (Figure 4.2) as follows

$$x_n = x_0 \sin(n\theta + \varphi_x) \quad , \tag{4.1}$$

$$y_n = y_0 \sin(n\theta + \varphi_y) \quad . \tag{4.2}$$

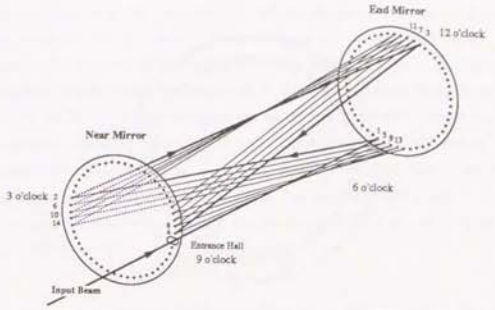

Figure 4.1: Alignment of the optical delay-line path

x_n	:	The x coordinate of the spot on the mirror
y_n	:	The y coordinate of the spot on the mirror
φ_x	:	Offset due to the initial beam profile for x
φ_y	:	Offset due to the initial beam profile for y
n (even)	:	Spot on the near mirror
n (odd)	:	Spot on the end mirror

The angle θ between successive beam spots is given by

$$\cos\theta = 1 - \frac{\ell}{R} \quad . \tag{4.3}$$

If θ satisfies the following equation :

$$N\theta = m \times 2\pi \quad , \tag{4.4}$$

N	:	Reflection number of the Delay-Line (always even number)
m	:	Natural number

the N-th beam spot on the near mirror matches with the position of the entrance hole. In other words, this laser beam emerges through the same hole where the incident laser beam enters through after traveling the Delay-Line path of approximately $N \times \ell$ (this

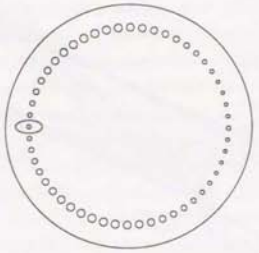

Figure 4.2: The Delay-Line spots on a mirror

is called as re-entrance condition). If ℓ equals R called as the confocal setting, the re-entrance condition provides four reflection numbers. If ℓ is slightly smaller than R, i.e. the near-confocal setting, Eq 4.3 is approximately expressed as follows

$$\ell \approx R\left(1-\frac{\pi}{N}\right) \quad \Rightarrow \quad N=\frac{\pi}{(1-\ell/R)} \quad . \tag{4.5}$$

This means that the total path length can be longer than the base-line by more than 100 times. Practically in TENKO-100, the distance between two mirrors with about 103.7 m curvature radius was adjusted to 100.5 m. Therefore, we could obtain the reflection number of 102, i.e. 10 km total optical path length. In addition, Eq 4.5 shows that the reflection number N can be adjusted by the deviation $d\ell$ m of the distance between mirrors ℓ m as follows

$$d\ell \approx \frac{\pi R}{N^2} dN \quad . \tag{4.6}$$

Hence, every four of N can be increased and decreased by $d\ell = 12$ cm adjustment.

In the case of an ideal optical delay-line (curvatures of four main mirrors are perfectly equal and they are set symmetrically), one of advantages is that the outgoing beam after

the optical delay-line can be treated equivalently to the beam reflected on the back of the spherical surface of the near mirror just as a simple Michelson interferometer. Thus, the performance of a Delay-Line interferometer can be simply explained as a multiplied one of a Michelson interferometer by a factor of N. Also, the outgoing beam depends only on second order on rotations and transverse displacements of mirrors. Therefore, the optical delay-line can be considered as an optical system made of realistic components that behaves as a one dimensional optical system having only one coordinate relevant to the phase of the outgoing beam to an excellent approximation. This is a remarkably helpful character for future km-class interferometers in which the position and the alignment control of mirrors is expected to be severer.

4.2.3 Gaussian Beam Propagation in a Delay-Line Path

In the former section, we treated the laser beam as a ray propagating, but the practical laser beam has approximately Gaussian distribution in intensity around its ray's axis. Specifically, the laser beam propagating over many kilometers can hardly be treated as an ideal ray with the infinitesimal width because of its diffraction, which is crucial in determining the spot size on the mirror and the optimum mirror size.

The properties of the Gaussian beam can be characterized by two factors which are functional to z (the distance from the output port of the laser). One property is the wave front curvature radius $R(z)$, and the other is the radius of the beam $\omega(z)$ defined as the length at $1/e^2$ times maximum power position. In this proposition, the phenomenon of the diffraction can be thought of as the process where $\omega(z)$, that is intensity distribution, in one plane is transformed into far-field intensity distribution by the spatial Fourier transformation. This means one Gaussian beam is transformed into another Gaussian beam. The typical propagation of a Gaussian beam, which has $R(z)=\infty$ at $z=0$ in free space, is described by $\omega(z)$ and $R(z)$ as follows

$$\omega^2(z)=\omega_0^2\left[1+\left(\frac{\lambda z}{\pi\omega_0^2}\right)^2\right] \quad , \tag{4.7}$$

$$\frac{1}{R(z)}=\frac{z}{z^2+(\pi\omega_0^2/\lambda)^2} \quad . \tag{4.8}$$

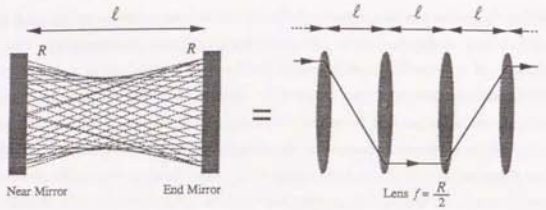

Figure 4.3: The Equivalent reflection pattern of an optical delay-line

ω_0 : The radius of a beam at the beam waist
λ : Wave length of a laser beam

This shows that $\omega(z)$ widens as filling a cone of half-angle Θ, according to

$$\Theta = \frac{\lambda}{\pi\omega_0} \quad . \tag{4.9}$$

The Delay-Line technique can prevent the beam spots from expanding out the mirror surface with the spherical curvature of the mirrors if the curvature of the beam just on the mirror is properly matched to the mirror curvature. Such beam traces back the same process after reflection on one mirror, and it is re-focused to the waist. The same curvature matching and reflection process are repeated on the other mirror which is located symmetrically about its waist. Therefore, the beam is kept between mirrors without expanding out. This is an excellent property for the confinement of the diffracted beam in finite space.

The propagation of the Gaussian beam reflecting between two mirrors according to the explained beam injection and mirror location, is equivalent with the propagation of a beam passing through a set of lenses with $R/2$ focusing length which are located with separation by the same distance ℓ m on a line successively (Figure 4.3).

Consequently, all spot sizes can be completely calculated from the first injection beam profile which is varied by two lenses. If the beam waist is set in the middle of mirrors, all spots have the same size as follows

$$\omega_{\min} = \sqrt{\frac{\ell\lambda}{\pi}} \quad . \tag{4.10}$$

Thus, we can obtain the optimum mirror size from the area and the distribution occupied by spots on the mirror.

4.2.4 Optimum Mirror size

To decide the size of mirrors, we must take into consideration the followings,

1. The entrance hole is wide enough to let the beam pass through with negligible diffraction due to the hole edge. In general, a safety factor (S) of $2 \sim 3$ is used. (S is defined as the ratio of the distance between the center of a re-entrant beam and a neighboring spot over the diameter of the re-entrant beam)

2. The neighboring spots on the near mirror should not be too close to keep "pre-re-entrant" beam from going through the entrance hole edge and keep their diffraction from coupling with the re-entrance beam. A part of them can be reflected at the edge of the entrance hole and travels a complete Delay-Line again and interferes with the re-entrant beam. This is the main source of the scattered light noise, i.e. the up-conversion noise (detailed in chapter 5).

3. A small mirror size is desirable to increase the resonant frequency of a mirror and it keeps the contribution of internal thermal noise out of the observation band.

4. It is better to eliminate overlapped area occupied by neighboring spots since it generates another type scattered light noise (detailed in chapter 5). However, it is expected to be sufficiently negligible in the contrary to the former scattered light noise that we might allow the overlapped area of spots.

For example, if we locate the injection beam waist at the entrance hole and allow spot overlaps, the minimum diameter of the spot circle can be obtained for all possible beam profiles as follows

$$D_{spot\ circle} = N\frac{S(\omega_{waist} + \omega_{next})}{2\pi} \quad . \tag{4.11}$$

In this case, one needs to consider that the biggest beam spot size of all spots, usually locating at 6 o'clock position, is safely in the mirror. Thus, the minimum mirror diameter was determined as follows

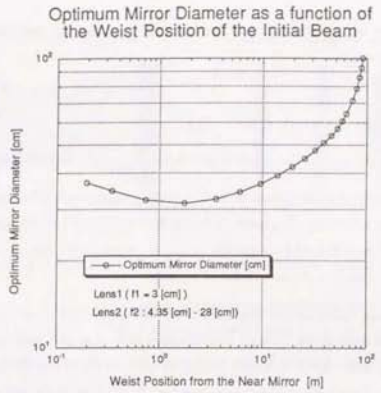

Figure 4.4: The optimum mirror diameter as a function of the waist position for the initial beam

$$D_m = S\frac{2+\sqrt{2}}{\pi}\sqrt{\lambda\ell} \quad . \tag{4.12}$$

Figure 4.4 shows the relation between the distance of the injection beam waist from the near mirror and the minimum mirror size with a safety factor 4 in the case of TENKO-100.

If N=102, $\ell = 100$ m, $\lambda = 514.5 \times 10^{-9}$ m and $S = 4$, it becomes ~ 32 cm, which was for the four main mirrors of TENKO-100. In this case, however, overlapped area was produced around 6 and 12 o'clock position on the mirrors.

4.2.5 Design of Mirrors

Table 4.2 shows the specifications of the four main mirrors, and their features are shown in Figure 4.5. All mirrors had the same features, 350 mm in diameter, 82 mm in thickness which was the minimum not to bend due to their own weight of 17 kg, and a groove around their circumference. The size and position of the entrance holes cut in only near mirrors

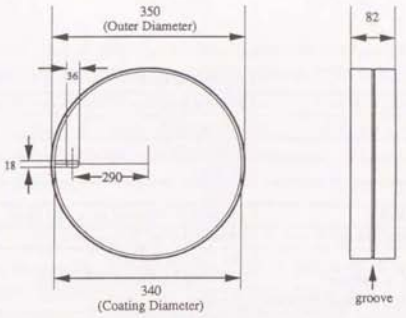

Figure 4.5: Mirror features

were based on the argument in the former section.

They were made of fused-silica which has high mechanical Q value of about 10^5 and a coefficient of thermal expansion (1.67×10^{-8} m/W). Other materials, for example, ULE and Zerodur, have excellently low coefficient of thermal expansion required under high power illumination in the future interferometers, but have low Q value of $10^3 \sim 10^4$ which are inferior property to increase the thermal noise. On the other hand, sapphire has high mechanical Q value of 10^8 and diamond has minimum coefficient of the thermal expansion, but they are awfully expensive.

The high reflectivity (over 99.99 %) and the isotropy of each mirror curvature radius are the most important property for the four main mirrors. They were polished and matched in their curvatures by Canon Co. Ltd. The polishing of the mirrors with so large curvature radius as ∼100 m was possible, while it was quite difficult to match their curvatures because the Newton Ring Method to measured their relative difference did not have enough accuracy to measure $\lambda/10$ deviation of the sasitter (defined as a gap in height between the bottom of a mirror surface and the edge of the mirror, see Figure 4.6), which causes 3.3 cm deviation of the focus length of the mirror curvature of 100 m.

Nevertheless, they have achieved ± 6 cm relative accuracy for the curvatures before coating. Absolutely, 103.73 m ± 3 cm for the averaged curvature of one pair of mirrors (after coating) in one arm and 103.68 ± 3 cm for the other pair of mirrors. These values

factors	Specifications
Substrate	Fused Silica
Density	2.22 [g/cm^3]
Diameter	ϕ 350 [mm]
Thickness	82 [mm]
Mass	17 [kg]
Entrance Hall	18 [mm] $\times$ 36 [mm] on ϕ 290 [mm]
Internal Resonance	1st=3565 [Hz], 2nd=5195 [Hz]
Radius of Curvature	100.5 [m] $\pm$ 3 [cm] (Polished by Canon. Co. Ltd)
Deviation from Ideal Surface	$\leq \lambda/10$
Roughness	$\leq 10^{-9}$ [m]
Coating	Dielectric multiple-layer (Ion Beam Sputtering by Showa Koki. Co. Ltd)
Reflectivity	99.96 % (99.95 %)
Center Wave Length	460 [nm] $\sim$ 550 [nm]
Incident Angle	0

Table 4.2: Mirror specifications

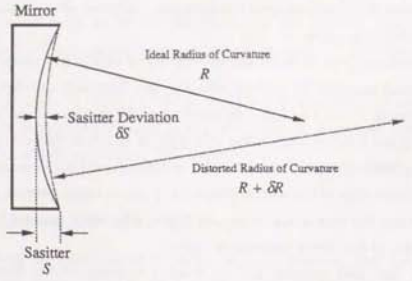

Figure 4.6: The sasitter of a mirror

were obtained by measuring the cycle of modulation frequency around 10 MHz which provided a minimum demodulated signal (which fell to 0 in ideally) from the interfering fringe between the beams before and after the delay-line modulated in phase with the same frequency. The difference of neighboring frequencies of (ν or λ) and ($\nu + \delta\nu$ or $\lambda + \delta\lambda$) which provide the worst efficient modulation means that counts of wave length involved in the Delay-Line path, *i.e.* L / λ for each frequency is different by just one as follows

$$1 = \left(\frac{L}{\lambda}\right) - \left(\frac{L}{\lambda + \delta\lambda}\right) \quad \rightarrow \quad 1 = \frac{L}{c}\nu - \frac{L}{c}(\nu + \delta\nu) = \frac{\delta\nu L}{c} \quad . \tag{4.13}$$

Thus, we could measure the absolute Delay-Line optical path length with the simple form $c/\delta\nu$ with an error by 3 cm.

After polishing, they were coated by Showa Koki Co.Ltd. with the dielectric multi-layer coating by using the Ion Beam Sputtering method. The reflectivity was 99.95 % at a wave length 514.5 nm according to their measurement, but in practice with a lot of other components in tanks, it was deteriorated to 99.9 %. This allowed only 36 % of the incident laser power to emerge from the Delay-Line. In addition, their curvature radii after coating were expected to be deformed because of the surface tension and to have the anisotropy in one mirror. Unfortunately, it was observed as a beam spot distortion detailed in the next section, as worried.

4.2.6 Beam Spot Shape Distortion and Counter Resolution

The beam spot shape distortion was an important problem in TENKO-100. If we located the beam waist at the entrance hole according to the argument of the mirror size, the beam spot shape, for example on the near mirror, became gradually transverse elliptic, and the "pre-re-entrant" spot suddenly changed its shape to longitudinal elliptic as shown in Figure 4.7(a). Finally, the re-entrant beam was distorted into a steeply longitudinal elliptic. It created a great deal of scattered light through the reflection from the entrance hole edge and decreased the contrast due to the unbalance of the both interfered light power.

It was natural to analyze this phenomenon as follows : the re-entrance condition depended on the average of the longitudinal and transverse radius of the mirror curvature, but longitudinal and transverse wave front radius of curvature in a re-entrant beam depended

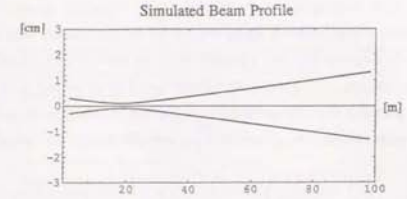

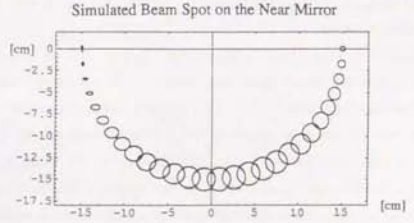

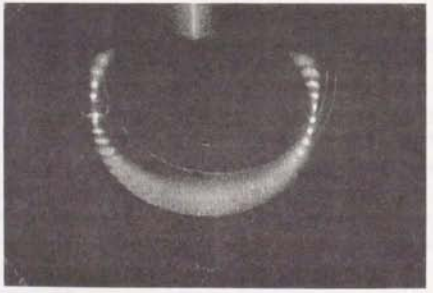

Figure 4.7: The simulations of the beam spot distortion

on the corresponding mirror curvature separately. As a result, one radius of curvature of a beam focused before the re-entrance, and the other focused after that. Consequently, this phenomenon could be explained by assuming that the longitudinal and transverse radii of a mirror curvature were not equal to each other.

We traced the radius of curvature of each beam's wave front on the near mirror using different conditions and assuming as follows (see Figure 4.8)

1. The radius of mirror curvature is different between the NM and the EM

R_0	(averaged radius of curvature)	:	100 [m]
R_l	(longitudinal radius of curvature)	:	$(1+k)\,R_0$
R_t	(transverse radius of curvature)	:	$(1-k)\,R_0$
k	(deviation parameter)	:	0.0005 to 0.005

2. Input beam profile

   The beam waist is slid from the position of the EM to the NM and to the front of the NM continuously keeping curvature matching between the averaged mirror curvature (R_0) and the beam wave front curvature.

3. Near and End mirror alignment

   The longitudinal line which involves the largest radius of curvature on the NM and the EM are set either parallel or cross.

Consequently, the distortion of the beam spot shape was simulated under the conditions that $k = 0.001$, $\omega_{near} = 0.3$ cm, $\omega_{end} = 1.3$ cm, and the parallel alignment. All of them were quantitatively consistent with the practical setting (Figure 4.7(b)) .

In addition, we found two configurations with which the beam shapes were fairly insensitive to the effect of the curvature anisotropy in a mirror. One configuration was to align the mirrors so that a longitude line which included the largest radius of curvature of each mirror cross with each other, and to prevent the both larger (or smaller) radii of curvature from dominating the focusing of one wave front radius of curvature of the beam all the time during its travel of the Delay-Line path. This was not practical work because it was hard to know exactly which longitude line involved the largest radius of curvature of the mirror. The other configuration was to locate the beam waist in the middle of the

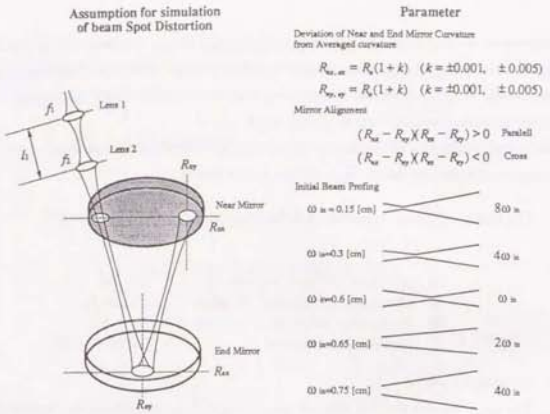

Figure 4.8: Simulation assumption for the analysis of the beam spot distortion

arm length. This created the same size spots on both mirrors as explained in the former section. As shown in Figure 4.9, we achieved drastic improvement of shapes and obtained better contrast from 80~70 % to 98 %

4.3 Suspension of Optical Components

4.3.1 Suspension for Quasi-Free Falling Masses

All four main mirrors and a beam splitter should behave as free masses for proper response to gravitational waves. To suspend test masses with wires in a pendulum configuration realizes quasi-free falling masses of mirrors over the resonant frequency of the pendulum, usually around 1 Hz. Though the ground motion excites the displacement of the test mass mirrors through the suspension wires, it provides the effective noise isolation of the external seismic noise and the acoustic noise (see in Chapter 5, Seismic Noise Isolation). In addition, the associate mass of mirrors can be used as test masses for passing gravitational waves.

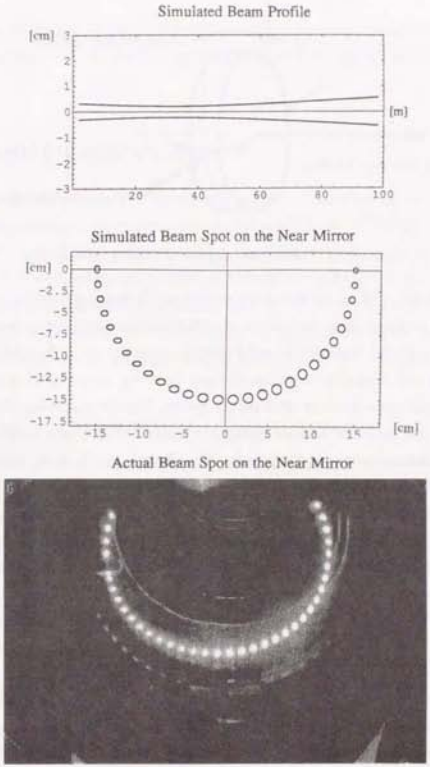

Figure 4.9: Improvement of the beam spot distortion with a beam profile which provides the beam waist in the middle of two mirrors, and correspondent simulation

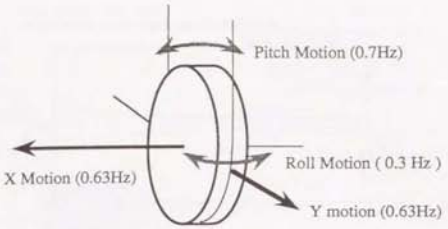

Figure 4.10: The motion degrees of freedom of a mirror

In TENKO-100, each of the four main mirrors and a beam splitter was suspended by a single wire wrapped along the groove around the lower half of the mirror perimeter. Two wire standoffs led to a mechanism for rough position control in the pitching motion of mirrors. They were located between the wire and the mirror perimeter a few mm above the half of the mirror where the wire left from the groove. The wire was made of tungsten with $\phi = 0.45$ mm that provided the least strength to suspend 17 kg mirror to enhance the first wire resonant frequency (see in Chapter 5). The effective length of the mirror pendulum (0.65 m) provided a 0.625 Hz resonant frequency in the two translational motions (named X and Y), 0.375 Hz in the rolling motion (R), and about 0.7 Hz in the pitching motion (P) (Figure 4.10). The excess resonant motions in X, Y, R, and P were so pronounced that they needed to be suppressed through a proper feedback control system such as a "Local Control" system.

4.3.2 Suspension Towers

Figure 4.11 shows a view of the suspension tower with a stack for an additional isolation. The whole suspension tower used two linear guides to adjust the position roughly in one translational direction by ± 1 cm for the matching of the optical paths. Six layers of stack were put on the top of the main frame and the top of the stack was connected through a long cylindrical spacer with the mirror suspension point. The whole structure of the mirror suspension point could be controlled in rotational and vertical motion through manometer

adjustment. Both ends of the wire wrapping the mirror were crossed along the groove of the supporting rods, and fixed along the groove of the bolts by the friction from the windings.

4.4 Mirror Local Control

A mirror local control system is an essential and fundamental system for interferometers using the suspended optical components. It has mainly two important functions. One of them is to control their position without direct contact not to excite their isolated displacements. This is indispensable not only to form the stable optical path and to obtain a good contrast but also to actuate them arbitrarily for the operation of interferometers as gravitational wave detectors. The other is to dump their excess motions at resonant frequencies of the pendulum especially excited by the ground motion through wires.

4.4.1 Rough Alignment

Each suspension tower was equipped with a coarse adjustment to the mirror positions in the vertical translation and rotation. The rotational degree of freedom was adjusted by the manometer located at the top of the stack and the pitching degree of freedom was adjusted by the screw translational function of the wire standoffs on the mirror sides in the air.

It is very important to match the both optical path lengths to suppress various kinds of noises, *e.g.* the frequency noise. In this sense, the whole end tank connected to the main duct with bellows was adjusted in position quite roughly (1 cm precision, corresponded to 1 m optical path length) in vacuum by three scissor jacks in parallel with the bellows between the end tank and the arm duct. The suspension towers for both end mirrors were adjusted in position under vacuum on linear guides by stepping motors controlled electrically from outside (maximum adjustable range was $\pm$ 1 cm, 0.1mm precision, corresponded to 1 cm optical path length).

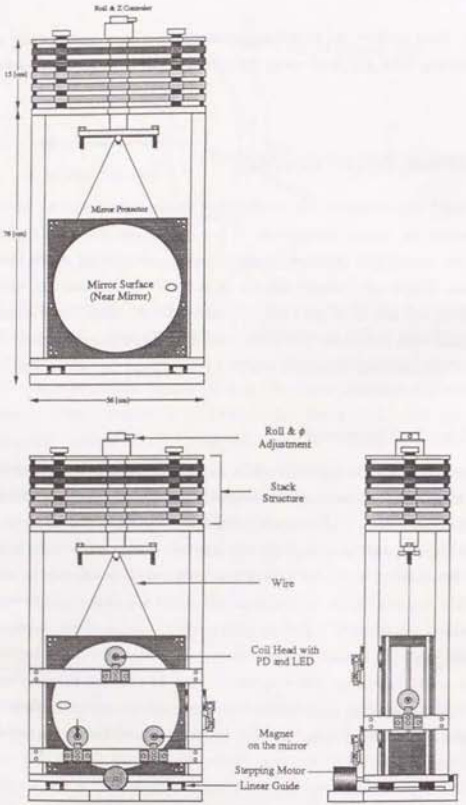

Figure 4.11: The suspension tower view

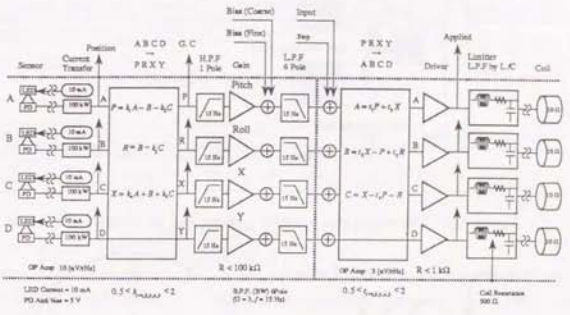

Figure 4.12: The local control feedback system

4.4.2 Local Control System

The local control system controls and maintains the relative position of the suspended mirrors to the suspension tower as well as it dumps the excess motion at the resonant frequency of the pendulum through the magnetic coupling force. Figure 4.12 shows the concept diagram of the local control system for TENKO-100.

Position Sensors and Mirror Actuators

Figure 4.13 shows the operation of the position sensor and the actuator for a mirror. The relative motion of the mirror with respect to the suspension tower was detected by a couple of an LED and a photo-detector involved in the coil-head attached to the suspension tower. In other words, it was detected as a current fluctuation in the photo-detector due to the shading the light illuminated from the LED in front of the photo-detector by the plate covered on the magnet (see in Figure 4.14). The mirror movement was controlled by the coupling force between the fixed permanent magnet and the coil current. Using this set up, the excess resonant motions of the pendulum are damped by the current of the coil

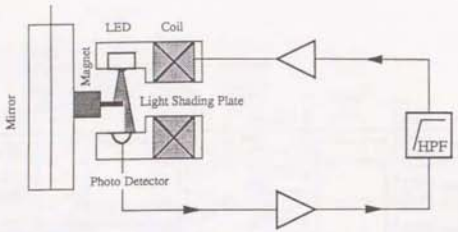

Figure 4.13: The principle of a position sensor and an actuator of a mirror

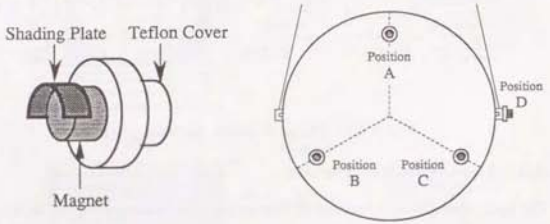

Figure 4.14: The alignment of mirror magnet

fed back from the detected signal. Moreover, the absolute position of a mirror was kept by applying a DC current to the coil.

The mirror which was suspended by a single wire had four degrees of motion freedom, *i.e.* two translational motions (X, Y) and two rotational motions (P, R) that needed to be detected and controlled. The three of the four magnets with shading plate were arranged to form "equilateral" triangle on the back of the mirror for the detection of X, R and P, and one magnet was located on the side of mirrors for the detection of Y (Figure 4.11).

The magnet (Table 4.3) should be strong enough to be able to actuate the 17 kg mirror within the practical current limited by the electric power consumption of the coil (Maximum ~1 W) under vacuum and the available FET's specifications. It should not too strong to decrease the sensitivity by its coupling noise (detailed later), and also not to enhance

Manufacturer	Product	Material	Apparatus	Magnetization
Shinetsu Chemistry	SEREM N42	Nd-B-Fe	ϕ10 [mm]×25 [mm]	T

Table 4.3: Specifications of magnets

Manufacturer	Product	Apparatus	Power	Angle	Wave Length
TOSHIBA Co. Ltd	TLN107A	4.05 [mm]×4.4 [mm] side view	2.0 [mW]	30	950 [nm]

Table 4.4: Specifications of LEDs

the eddy current in the copper wire of the coil, which disturbed the natural pendulum motion. It should not too big to decrease the mechanical Q value of a mirror which was inversely proportional to the thermal noise. In addition, the magnet was protected with a teflon cover to prevent hitting violently the mirrors and scratching them by its broken pieces (Figure 4.14).

Table 4.4 and Table 4.5 show the specifications of the LED and the photo-detector. They were especially selected because of their anti-magnetic lead line to prevent the attractive force of strong magnets from disturbing the natural pendulum performance.

The coil-head had a dynamic range of 2 mm, an efficiency was 8.3 μA/mm and the driving capability was 6×10^{-6} m/V for the translational movement.

Signal Composition and Decomposition

The excited motions at resonant frequencies for each degrees of freedom were damped below the acceptable level of the interferometer control by the coupling force between the magnets and the coil current which were controlled by the local control feedback servo

Manufacturer	Product	Apparatus	Area	Angle	Wave Length
TOSHIBA Co. Ltd	TPS703	7.6 [mm]×7.0 [mm] side view	8.7[mm^2]	130	$\geq$ 800 [nm]

Table 4.5: Specifications of photo-detectors

system. Different from the case of TENKO-10, it was expected that the displacement caused by the force of the actuator might be quite different for each degree of freedom X, R and P because the mirrors used in TENKO-100 were so heavy (about 17 times as heavy as one used in TENKO-10) that the inertia force of X, R, and P were quite different. This meant that the necessary critical damping forces were so different that the force for X might be too big to oscillate R and P. Thus, we took the method to compose the proper signals of X, R, P and Y from the position signals of A, B, C and D, and to give proper gain and filtering to them, and to decompose them proper signals for the coils A, B, C and D (refer to Figure 4.12).

The flow of the composition and the decomposition of feedback signals are shown in Figure 4.12. A set of k and t factors are gain adjusting functions to compensate the following individual characteristic coupling force : (1) the relative position between the magnets and the coils, (2) the sensor efficiency due to the relative positions between the photo-detectors and the shading plates or the LED illumination power. All of them decreased the mode separation performance of the signal composition and decomposition. Though ten factors of freedom were required for the absolute compensation, only five factors were practicably enough for the relative compensation for each factor. The set of k factors was determined experimentally by regarding the B position signal as the first reference. In the same way, the set of t factors was determined experimentally by regarding the P signal in B signal, the X and R signals in C signal as the first references (refer to Appendix A for the detailed experimental setting for the k and t factors). In this way, more than 20dB isolation of other modes could be achieved for each translation, hence, it also widened the dynamic range for the magnet-coil path of the dark fringe locking (detailed later).

Critical Damping and Feedback Servo Design

Figure 4.15 shows the feedback control block diagram for damping resonant motions of the mirror pendulum. The proper gain and the phase compensation are required since the phase of the transfer function of the pendulum is delayed by 180 degrees at the resonant frequency. At the same time, the feedback frequency range should be less than 100 Hz since the above 100 Hz is the targeted frequency band and it should not disturb the quasi-free falling mass behavior of mirrors. Thus, a band pass filter composed of a 1-pole high pass filter and a 6-pole low pass filter was used for this feedback control. The pole frequency

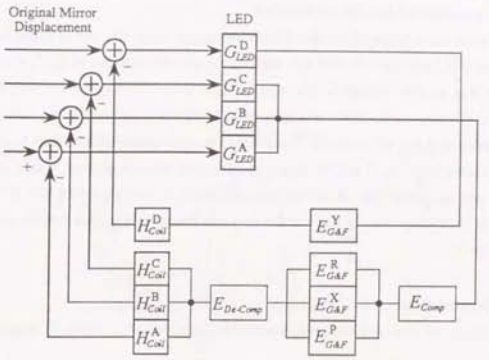

Figure 4.15: The block diagram of the local control system

of the band pass filter was desirable as low as possible, but it was limited by the demand to keep enough phase margin that was drastically lost by the 6-pole low pass filter at each resonant frequency of the pendulum. 15 Hz was chosen as its pole frequency.

Circuit Noise and Coupling Noise

The voltage applied to the coils of the local control circuit had intrinsic electrical noise such as "Johnson noise" of resistors and the equivalent input noise of available FETs. The total amount of noise after the 6-pole low pass filter could be large enough to decrease the sensitivity because the system noise voltage also actuated the mirror, *i.e.* so-called MC-coupling noise. To suppress the MC-coupling noise to less than 3 nV/$\sqrt{}$ Hz which corresponded to 2×10^{-20} 1/$\sqrt{}$ Hz at 100 Hz in sensitivity, we used resistors under 1 kΩ and FETs whose equivalent input noise were as small as possible. The present system noise is $\sim$ 30 nV/$\sqrt{}$ Hz. Hence, more improvement by decreasing the value of resistors will be required in future.

Other Functions of the Local Control

There were three types of monitor functions, one of them was the position monitor for A, B, C and D positions, another was the GC monitor for motions of X, R, P and Y, and the other was applied voltage to the coils at A, B, C and D. The mirror relative position respect to the suspension tower was controlled by the bias current to the coils controlled by the coarse and fine adjustment. There were two types of input functions to actuate the mirror motions in X, R, P and Y. One input function was the manual square pulse input function and the other was an arbitrary signal input function used for the MC feedback port of the dark fringe locking and the absolute control detailed in this chapter and Chapter 5 respectively.

Local Control Feedback Circuit

Accordingly, we designed the local control feedback circuit as shown in Appendix B.

4.5 RF Dark Fringe Locking

4.5.1 Internal Phase Modulation Technique

To obtain the first order signal of the relative optical path fluctuation, the laser was modulated in phase by the Internal Phase Modulation technique as shown in Figure 4.16. Electric Optical Modulators (EOM), or so-called Pockels cells, used to modulate the phase of the laser light were located in both laser beam paths in each arm. The modulation frequency was chosen to be over 10 MHz since the intensity noise of the laser was expected to be below the shot noise level and the intensity noise around modulation frequency would not convert down to the observational band.

One of advantages of this technique is the ease of modulation with large amplitude requested to obtain the optimum sensitivity under the low contrast. On the other hand, the absorption of the laser power and the wave front distortion due to the thermal expansion due to the location of the Pockels cell involved in each arm would deteriorate the optical power gain by the recycling technique indispensable for the future km-class interferometer.

To demonstrate the RF dark fringe locking, we take such an interferometer as shown in Figure 4.16. The input beam with electric field amplitude of E_0 is divided perfectly

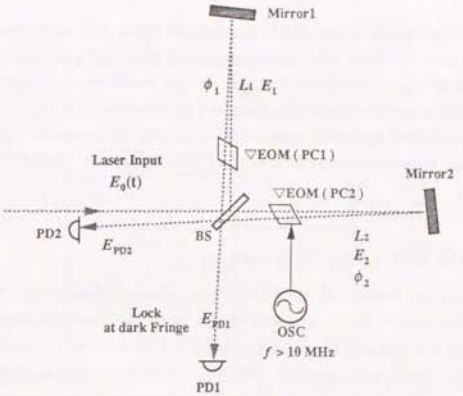

Figure 4.16: The internal modulation technique for the interferometer

in half power and the both return to the output port (PD1) with phase delays of ϕ_1 and ϕ_2, respectively. The beams in both paths are modulated by EOMs (PC1 and PC2) with inverted phase through a sinusoidal signal whose amplitude is $m/2$ (modulation index) and angular frequency $\omega_{\rm mod}$. Neglecting any losses and assuming the perfect contrast, the electric field of the interfered beam at PD1 with phase delay is given by

$$E_{\rm PD1} = \frac{E_0}{2} e^{-i\left(\phi_1 + \frac{m}{2}\sin\omega_{\rm mod}t\right)} - \frac{E_0}{2} e^{-i\left(\phi_2 - \frac{m}{2}\sin\omega_{\rm mod}t\right)} \quad . \tag{4.14}$$

Then, the output photo-current of PD1 is given by

$$I_{\rm PD1} \propto 1 - \cos\left(\phi_1 - \phi_2\right)\cos\left(m\sin\omega_{\rm mod}t\right) + \sin\left(\phi_1 - \phi_2\right)\sin\left(m\sin\omega_{\rm mod}t\right) \quad . \tag{4.15}$$

Using the condition for a dark fringe, *i.e.* $\phi_1 - \phi_2 = \Delta\phi \approx 0$, Eq 4.15 is expressed to the first order of $\Delta\phi$ with Bessel functions as follows

$$I_{PD1} = \frac{I_0}{2}\left(1 - J_0\left(m\right)\right) + I_0 J_1\left(m\right)\Delta\phi \quad . \tag{4.16}$$

The first term corresponds to the noise current and the second term corresponds to the displacement signal. The detectable displacement or equivalent shot noise can be defined by the ratio of the square root of the first term and the second term. Though the best shot noise level in principle can be obtained at $m = 0$ for the perfect contrast, the practical shot noise is deteriorated by thermal noise of a photo-detector and imperfect contrast. We, therefore, should choose the best modulation index for each contrast (detailed in Chapter 5. Shot Noise).

4.5.2 EOM with Large Aperture

In TENKO-10, the Pockels cell crystal, PM-25 (produced by Gsänger Co. Ltd.) with the aperture of 5 mm × 5 mm, was large enough to let the beam pass through. In TENKO-100, it was necessary to use larger Pockels cells with 1 cm × 1 cm apertures for the sake of minimizing the beam spot distortion due to the anisotropy of the mirror curvature. However, it would be afraid to produce a great deal of power absorption, wave front distortion, loss of the modulation efficiency and especially much scattered light.

Figure 4.17 shows the setup to measure the phase modulation efficiency from the known MC efficiency. It was measured to be 9.3 pm/V for one side voltage loading, which was 1/20 times efficiency of the PM-25. But, it was barely useful as a modulator and as a feedback actuator because of the well-stabilized frequency noise and well-damped seismic noise.

4.5.3 Optimum Modulation Index

For an ideal interferometer setup with a contrast of 100 %, $m = 0$ gives the best S/N, *i.e.* the shot noise level, which is equal to the principle S/N of an interferometric detector independent of detection techniques. In TENKO-100, the optimum modulation index should be chosen carefully for the realized contrast to maximize the S/N because the contrast was expected to be around 90 % due to the wave front distortion due to the roughness of the mirror surfaces which was strongly limited by the present polishing and coating techniques and due to the residual light power due to the scattered light from the optical delay-line path.

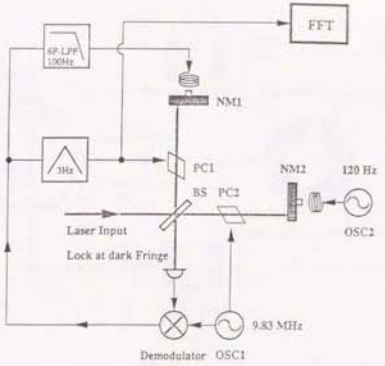

Figure 4.17: The experimental setup for H_{pc} measurement

4.5.4 Push-pull Modulation Technique

Although it would be necessary to modulate strongly the laser in phase at high frequencies over 10 MHz to minimize the shot noise level for the poor contrast in TENKO-100, it was not so easy in practice because of the poor pockels cell efficiency as measured. For example, an applied voltage over 1000 V for one Pockels cell is required to obtain $m = 0.5$ which provides minimum shot noise level for the contrast $K = 0.995$.

However, better modulation efficiency was obtained by using a push-pull modulation technique, *i.e.* twice the regular efficiency could be obtained by modulating in inverse phase for each Pockels cell. The original voltage was already amplified with the ferrite-core transformer to several hundreds volts in the secondary coil from ~ 10 V in the primary coil which was driven by the 100 W "Ham" amplifier (Figure 4.18). In addition, the "quadra-feedback" technique with additional twice efficiency by applying anti-polar voltage to two electrodes of one Pockels cell enlarged the dynamic range of the feedback efficiency of the pockels cell path for the dark fringe locking feedback servo.

In the TENKO-100, the optimum modulation index should be 0.96 with a typical contrast

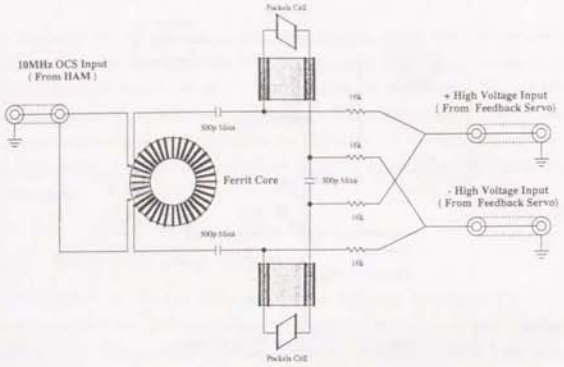

Figure 4.18: The push-pull modulation technique for the strong modulation

of 95 %. In practice, this was impossible with such big Pockels cell where $m \approx 0.2$ was the maximum. Consequently, the deterioration of the shot noise level was inevitable (detailed in Chapter 5, Shot Noise).

4.5.5 Detectors and Demodulators

The interfering light containing the mirror displacement signal produced by the phase modulation according to Eq 4.16 was detected by a photo-detector at the output port of the interferometer. The output of the detector after transformation from the photo-current to the voltage was demodulated by a double balanced mixer. The reference signal was at the same modulation frequency, but slightly shifted in phase to obtain the first order signal of the mirror displacement.

The noise of detectors directly limits the sensitivity of the interferometer since the noise of the detectors and the signal from gravitational wave produce fluctuations of photo-current *i.e.* the same signal theoretically. The equivalent displacement noise of the detector was measured as photo-current produced by the illuminated light which produced twice as large

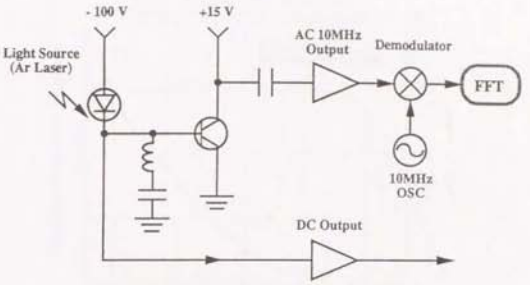

Figure 4.19: The setup for the measurement of the equivalent photo-current of the resonant type photo-detector

demodulated shot noise as one without illuminated light.

To reduce the detector's noise, a set of LC (inductor and capacitor) resonators at the modulation frequency and an LC eliminator at twice the frequency of the modulation frequency were used in series in the circuit of the detector. As a result of the measurement with the setup as shown in Figure 4.19, the equivalent photo-current noise proved to be 0.22 mA. For the same reason, a set of RC (resistor and capacitor) high pass filters were used in the circuit of the demodulator as shown in Appendix C. The two phase shifters were installed in front of the mixer for the reference modulation signal input to maximize the demodulated signal.

The photo-detector was made of InGaAs and had an aperture of $\phi = 5$ mm with a saturation laser power of about 40 mW. Ideally, the laser power of the dark fringe falls down to zero. In practice, the residual laser power due to imperfect contrast illuminated the photo-detector. In the final stage of TENKO-100, where $K = 95$ % and the incident laser power is ~2 W, the output power at the dark fringe reaches 50 mW and it exceeds the ability of the present photo-diode. Thus, a multi-photo-detector system was prepared for the future usage.

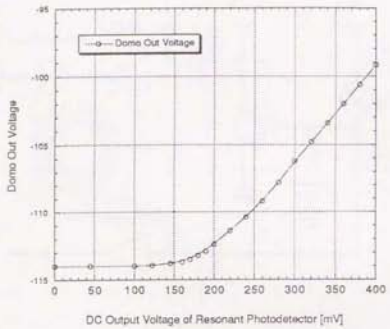

Figure 4.20: The equivalent photo-current of the resonant photo-detector

4.5.6 Main Feedback Servo Design

Observational Band Width

The observational band is inversely proportional to the characteristic time which the beam takes to travel the optical delay-line path. In the case of TENKO-100, the minimum frequency where the effect of the phase modulation to derive the displacement signal vanishes, is about 15 kHz, because the light goes through the Pockels cell twice for the phase modulation, once before and once after the Delay-Line with the time lag by 33μsec, *i.e.* which the light takes to travel the Delay-Line path of ~10 km. The normalized sensitivity of TENKO-100 became as in Figure 4.21. Therefore, the unity gain frequency of the feedback servo was limited to less than 10 kHz if we wanted to obtain more than 60 degrees of phase margin because of the phase delay due to the Delay-Line.

Feedback Path and Open Loop Gain Sharing

There were two paths in the feedback loop. One was a pockels cell path (PC) and the other was a magnet-coil path (MC) (see in Figure 4.22). The pockels cell path had fast

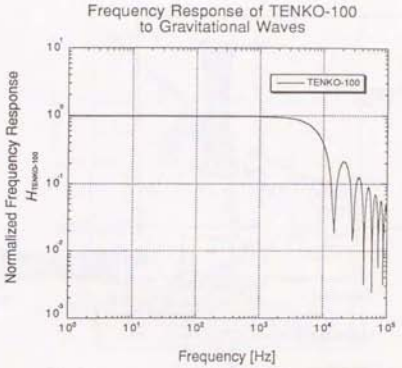

Figure 4.21: The frequency response of TENKO-100 for gravitational waves

response under 1 MHz, but its dynamic range of controllable displacement was too small (~ nano-meter) to keep the dark fringe in the low frequency range. This was because the applied voltage to the Pockels cells was limited by the practical specification of ~ 100 V. Only the high pass filtered part of the original demodulated signal was fed back to the Pockels cells with the quadra-feedback technique (refer to Figure 4.18). On the other hand, the magnetic-coil path had a sufficient ability to actuate mirrors, about 1 mm, in the low frequency range. So, only the low pass filtered part of the original demodulated signal was fed back to the MC through input function of the local control.

The proper sharing of the open loop gain between the PC part and the MC part brought the stable dark fringe locking. In the low frequency range, the original transfer function of the magnet-coil path characteristic of a f^{-2} law was by itself quite suitable for the initial feedback gain to take charge of the fluctuation of the optical path difference which was mainly dominated by the seismic noise (detailed in Chapter 5 : Seismic Noise). Its spectrum was also characteristic of a f^{-2} law. The feedback signal to the pockels cell path needed to be high-pass filtered at higher than 30 Hz to keep it from saturating in the low frequency range, and also needed to be low pass filtered to cross the MC path and the unity gain level by the derivative difference of a f^{-1}.

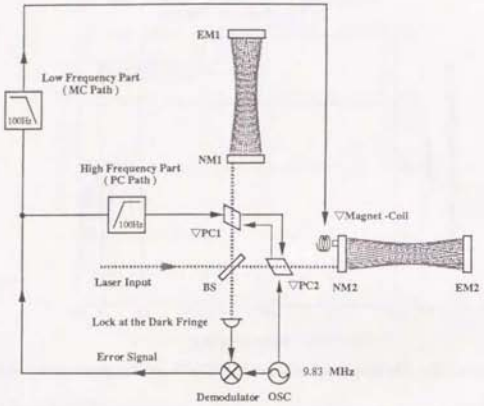

Figure 4.22: The darkfringe locking system of TENKO-100

To make the most of the feedback servo feature for the Delay-Line laser interferometer, it is desirable that the cross over frequency between the MC path and the PC path is as low as possible, and it was chosen around 50 Hz~100Hz in TENKO-100. For one thing, the feedback signal to the PC can just be regarded as the displacement fluctuation of the path difference, *i.e.* the sensitivity, over the cross over frequency (detailed later). Secondly, the wire resonance (violin mode) is at 128 Hz and its harmonics should not be excited by the MC feedback. In the same way, the feedback signal over 1 kHz must be cut severely not to excite the lowest internal resonance mode of the main mirror at 3.2 kHz by the MC feedback.

Accordingly, we designed the bode diagram of the feedback servo as shown in Figure 4.23. The measured open loop gain curves shown by a dotted curves were in good agreement with the theoretical curves shown by solid curves.

Integration of Open Loop Gain for the Intensity Noise Reduction

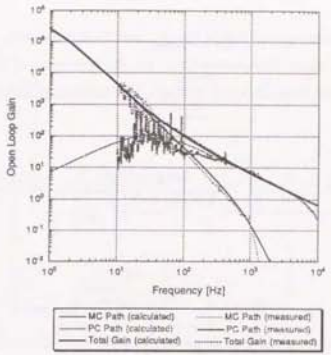

Figure 4.23: The bode diagram of the main feedback servo

The purpose of the dark fringe locking is not only a sensing technique for the interferometric gravitational wave detector but also a technique to suppress the intensity noise (detailed in Chapter 5, Laser-Originated Intensity Noise). The residual dark fringe fluctuation below about 0.5 Hz is coupled with the intensity noise as follows,

$$\Delta L_{int} = \frac{\delta I}{I} \Delta L_{dark} \quad , \tag{4.17}$$

where I, ΔI, and ΔL_{dark} are the intensity of a beam, the intensity fluctuation of the beam and residual fluctuation of the dark fringe, respectively. This residual fluctuation can be suppressed by higher open loop gain. To suppress the contribution of the intensity noise of typically $\delta I / I = 10^{-3}$ below the aimed shot noise level $\Delta L = 10^{-16}$ m/$\sqrt{}$ Hz, more than 10^3 gain was required in addition to the acquisition gain of 10^6 of the dark fringe locking.

Signal Output Section and Circuit Noise

Figure 4.24 shows the block diagram of the feedback system of TENKO-100. The equivalent input noise of each section due to FETs noise and Johnson noise of resistors in the electric feedback circuit are significant noise sources. The monitor point to obtain the

sensitivity signal was selected just before the E_{pc} part to maximize the S/N to their composition. The common signal flow section (E_{tot}) for the both path of the MC and the PC was derived theoretically from the same demand. The theoretical monitor signal V_{mon} is

$$V_{mon} = \frac{L_o D E_{tot} E_{pc} + N_{tot} E_{tot} E_{pc} - N_{pc}(E_{pc} + D E_{tot} E_{pc} E_{mc} H_{mc}) - N_{MC} D E_{tot} E_{pc} E_{mc} H_{mc}}{1 + G_{pc} + G_{mc}} \tag{4.18}$$

$$G_{pc} = D E_{tot} E_{pc} H_{pc} \quad G_{mc} = D E_{tot} E_{mc} H_{mc}$$

L_o	:	Light path fluctuation due to gravitational wave signals	[m]
D	:	Converting of an interferometer	[V/m]
H_{pc} H_{mc}	:	Efficiency of the Pockels cell and the magnet-coil	[m/V]
E_{tot} E_{pc} E_{pc}	:	Electrical gain and frequency characteristics of each section	
N_{tot} N_{pc} N_{mc}	:	Equivalent input electrical noise before E_{tot},E_{pc} and E_{mc}	[V/m]

In the frequency range where the open loop gain of the PC(G_{pc}) is much larger than that of the MC(G_{mc}), Eq 4.18 is simplified by neglecting any other noises to

$$V_{mon} = \frac{L_o}{H_{pc}} \quad . \tag{4.19}$$

This monitor voltage can be regarded as the displacement fluctuation of the optical path difference of the interferometer if it is multiplied by the pockels cell efficiency, *i.e.* H_{pc} m/V.

At the same time, Eq 4.18 shows that the equivalent input noise, $\sim$10 nV/$\sqrt{}$ Hz for N_{tot} and $\sim$ 3 nV/$\sqrt{}$ Hz for N_{mc} and N_{pc}, can be comparable with L_0, namely sensitivity itself, if they are multiplied with the electrical gain of E_{mc} assuming $D = 10^8$, and it is inversely proportional to E_{tot}. Although the electrical gain of E_{tot} is desirable to be as large as possible, it is limited to about 50 practically because of the ratio between the output voltage swing of the available lowest noise FETs used in E_{tot} *i.e.* $\pm$15 V.

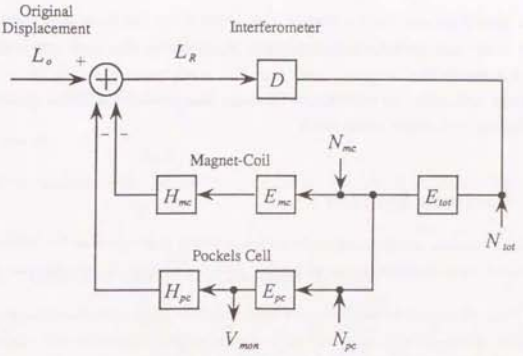

Figure 4.24: The block diagram of the main feedback servo

However, it was possible to suppress the circuit noise to $\sim 10^{-17}$ m/ $\sqrt{}$ Hz below the aimed sensitivity 2×10^{-16} m/$\sqrt{}$ Hz with the following open gain setting detailed in the next paragraph.

Circuit Design

Using the previous concept, we designed the feedback servo circuit for the dark fringe locking with only low noise FETs with the equivalent input noise of 0.9 nV/$\sqrt{}$ Hz and input resistors below 1 kHz with Johnson noise of 3 nV/$\sqrt{}$ Hz. The original demodulated signal was amplified sufficiently by 20 times for the circuit noise suppression and was divided into two sections. A gain integration circuit which changed the open loop gain slope by a f^{-1} below 1 kHz was installed before the dividing point to obtain more three orders of magnitude gain below 1 Hz for the intensity noise suppression (E_{tot} section). The signal for the PC path was amplified by 100 times in both polarities with high-voltage buffer-amp newly designed to avoid the excess input noise of a high-voltage amplifier ($\sim$100 nV/$\sqrt{}$ Hz) and band pass filtered at 30 Hz (E_{pc} section). The signal for the MC path was 6-pole

low-pass filtered not to excite the internal mode of the mirror and fed back to the X input function of the local control of one near mirror (E_{mc} section). The total circuit design is shown in Appendix D.

With this application, we succeeded in the dark fringe locking in TENKO-100 with the longest optical path length in the world.

4.6 Vacuum System

A vacuum system is indispensable for such a sensitive experiment as the detection of gravitational waves to eliminate the phase fluctuation noise and the acoustic noise due to the air.

4.6.1 Required Vacuum Level

All optical components constructing of the interferometer after polarized beam splitter (PBS) were housed in the vacuum chamber. There were many reasons for this. First, the phase fluctuation noise of the beam due to the refractive index fluctuations of the air can be eliminated and greatly reduced in a vacuum. Secondly, the acoustic noise from the environment as well as the pollution from dust can be extremely eliminated. Thirdly, the RF discharge of the modulation high voltage ($\sim$ 500 V) to the Pockels cell can be prevented. The required level of vacuum for each consideration is given by

Fluctuation noise of a beam	:	2×10^{-2} [Torr]
Acoustic noise	:	1×10^{-2} [Torr]
RF discharge	:	1×10^{-2} [Torr]

Therefore, the minimum targeted level of vacuum was set at 10^{-3} Torr which had a factor of 10 safety times. In addition, the request for the vacuum system in the future km-class interferometer is the followings,

1. High vacuum below 10^{-8} Torr

   10^{-8} Torr corresponds to the sensitivity of 10^{-21} $1/\sqrt{}$ Hz.

2. Ultra pure materials

   Low outgasing materials for ducts, components and oil free pumps. It is desirable to use only ion pumps to keep 10^{-8} Torr silent enough to operate. Special coating treatment for the ducts may be required.

3. Low cost

The vacuum system of TENKO-100 was to realize low cost, high performance vacuum system.

4.6.2 Construction of the Vacuum System

Figure 4.25 shows the whole vacuum system with chambers and ducts for the TENKO-100. Figure 4.26 shows the pumping system of TENKO-100 which was designed to obtain 10^{-6} Torr pressure with full pumping and below 10^{-4} Torr pressure with partial pumping.

Vacuum Chambers

The vacuum system consisted of two parts, one was the three tanks (one central tank and two end tanks) (Figure 4.27) to install the optical components, and the other was the ducts where the laser beam travels the optical delay-line path.

The three tanks were made of aluminum and consisted of a vessel and a cover. Their specifications are shown in Table 4.6. The central tank was placed on a spacer made of plastic fixed directly to the floor of the central room, and the end tanks were fixed on iron plates which were supported by four casters for the adjustment in their position.

The central chamber involved a beam splitter, two near mirrors, a beam sampler and a reflection mirror with a PZT for an absolute control (detailed in Chapter 5: Scattered Light Noise), a PBS, two Pockels cells, and their supporting equipments (suspension towers, stacks and optical stages and so on). The central chamber had one evacuation hole and five windows, with 60 cm diameter, two of them were used for the connection port of D-subs and BNC cables that led signals into and out the chamber. One port with five anti-reflection optical windows was used for the beam injection and readout. The other port was for looking in it. The central chamber was connected to the arm ducts, a part of which was in the central house, spaced with three components : (1) the short acrylic

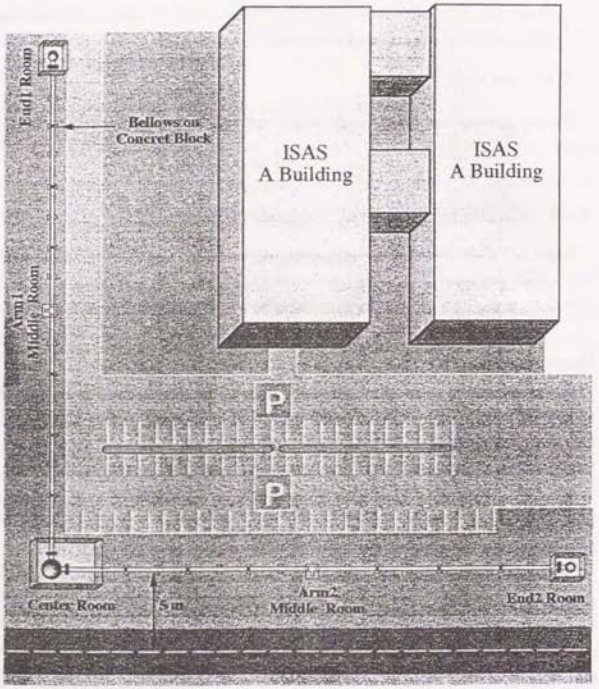

Figure 4.25: The vacuum system with chambers and ducts for TENKO-100

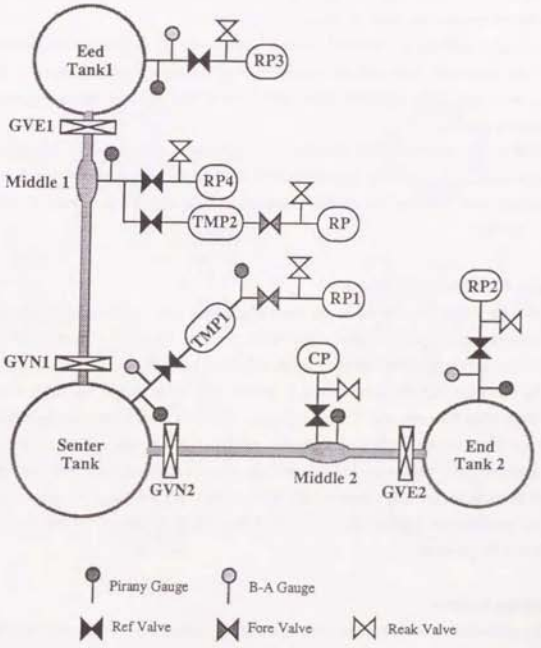

Figure 4.26: The pumping system of TENKO-100

ducts for looking at the surface of near mirrors, (2) the welded bellows (refer to Table 4.7) to compensate the thermal expansion and contraction of ducts, (3) the gate valves (refer to Table 4.8) to isolate the vacuum of the arms in order to decrease outgasing of the ducts due to the frequent exposure by the air.

The end chambers also involved the end mirrors with all supporting equipment. Each had one evacuation hole and two windows. End chambers were connected to the arm ducts with large welded bellows spaced with three scissor jacks for the adjustment of the chamber's position.

Much outgas was expected from many optical components and operational parts in the vacuum system. In addition, the outgas from the tank's surfaces consisted mainly of H_2, generated from H_2O and the chemical reaction of H_2O with Al, and made it difficult to evacuate fast.

Ducts, Bellows, Gate Valves

Table 4.9 shows that the ducts are made of stainless steel to minimize the outgas from the internal surfaces of the 100m ducts which make up the most of the internal surface area. The main composition of the outgas is H_2O, CO and H_2.

One arm consisted of eight units of a welded duct made of two 6m ducts which had 40 cm internal diameter and 3 mm thickness. All ducts were placed on the rolling rods fixed on the concrete blocks and connected with each other with bellows to compensate the transformation by the air pressure and the thermal expansion and contraction of the ducts because almost ducts were located outside and they were easy to be affected with the air temperature (Figure 4.25). The end of the arm on the side of the end chamber was fixed to a large block.

Pumping System

The achievable vacuum level and the speed of the evacuation are important aspects of a pumping system. In addition, the silent and oil free operation is also important to protect the high quality optical components alike main mirrors whose reflectivity is 99.95 % from pollution. The whole system could be evacuated to 5×10^{-5} Torr by two turbo molecular pumps (TMP1, TMP2) and one cryo pump (CP) after rough evacuation to 10^{-1} Torr by four rotary pumps (RP1, RP2, RP3, RP4) within six hours. During the operation of the

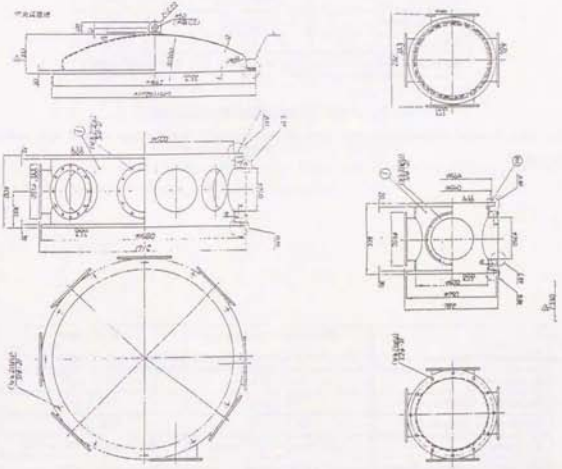

Figure 4.27: The center and end vacuum chambers

Aspect	Center Tank	End Tank
Material	Al	Al
Internal Diameter	1500 [mm]	600 [mm]
Height	2000 [mm]	1500 [mm]
Thickness	10 [mm]	10 [mm]
Volume	3×10^3 [ℓ]	0.4×10^3 [ℓ]
Surface Area	1.2×10^5 [cm^2]	3.4×10^4 [cm^2]

Table 4.6: Dimensions of chambers

They were housed individually and were connected with main arms spaced with below and gate valves.

Dimensions	Welded Bellows (for End Connection)	Bellows (for Duct Connection)
Subscribe	SUS 304	SUS 304
Internal Diameter	370 [mm]	380 [mm]
External Diameter	430 [mm]	423 [mm]
Extension	200 [mm]∼400 [mm]	80 [mm]∼140 [mm]
Extension Reception	400 times	400 times
Leakage	$\leq 10^{-9}$ [Pa m^3/s]	$\leq 10^{-9}$ [Pa m^3/s]
Temperature	0∼60 [°C]	0∼60 [°C]

Table 4.7: Dimensions of bellows

Four bellows were used for duct connections and two welded bellows used for end tank's connections to adjust their position.

Dimensions	Gate Valve
Subscribe	SUS 304
Gate Diameter	400 [mm]
Pressure Tolerance	$1.3 \times 10^{-7} \sim 1.0 \times 10^5$ [Torr]
Extension	200 [mm]∼400 [mm]
Leakage	$\leq 10^{-11}$ [Pa m^3/s]
Life Time	20000 times
Operation	Air pressure
Time	6 [s]

Table 4.8: Dimensions of gate valves

Four gate valves were used to keep the system evacuated as permanently as possible even during some works in different parts of the detectors.

Aspects	1 Unit	Total
Material	SUS 304	-
Internal Diameter	400 [mm]	-
External Diameter	406 [mm]	-
Length	12 [m] (welded with two 6 m Ducts)	96 [m] (2 sets)
Volume	1.6×10^3 [ℓ]	$2 \times 1.28 \times 10^4$ [ℓ]
Surface Area	1.5×10^5 [cm^2]	$2 \times 1.2 \times 10^6$ [cm^2]
Leakage	$\leq 10^{-8}$ [Torr ℓ / s]	-

Table 4.9: Dimensions of ducts

Eight units spaced by bellows formed one arm, and the ducts were exposed outer environment. They were not baked at all to induce outgas, but naturally baked by the sun in summer time (outer surface reaches 50 °C).

Location	Type	Evacuation Speed
West End Tank	Rotary Pump	300 [ℓ/min]
Mid West End Tank	Cryo Pump	-
Center Tank	Turbo Molecular Pump	2000 [ℓ/sec]
	Rotary Pump	760 [ℓ/min]
Mid South Tank	Turbo Molecular Pump	1500 [ℓ/sec]
	Rotary Pump	2500 [ℓ/min]
South Tank	Rotary Pump	500 [ℓ/min]

Table 4.10: Specifications of vacuum pumps

interferometer, TP1 was stopped because it produces 420 Hz vibration, and vacuum was maintained by CP and TMP2 located in the middle-arm sections. The specification of each pump is shown in Table 4.10.

4.6.3 Total Performance of the Vacuum System

In the case of the only one arm, the minimum vacuum reaches 4.4×10^{-6} Torr. From the outgas measurement of 4.16×10^{-10} [Torr liter sec^{-1} cm^{-2}] and the rate of vacuum of 0.25×10^{-6} Torr min^{-1}, operation of over 6.6 hours without pumping is possible. In practice, CP and TMP2 are operated during interferometer operation since the effect of their vibration has negligible effect on the interferometer.

Although the only each arm can be evacuated to 4.4×10^{-6} Torr and 8×10^{-7} Torr respectively, the total vacuum level is limited around 5×10^{-5} Torr.

4.7 Total Optical Design

Figure 4.28 shows the whole optical design of TENKO-100 for the gravitational wave detector. The beam emitted from the laser goes through one Faraday-Isolator to prevent any beam from returning to the laser. About 10 mW power of the beam is sampled with the beam sampler for the frequency stabilization. The rest of the beam passes through the

AOM for intensity stabilization and through a set of three lenses for the beam profile. The laser beam, then, reflects on a set of two crank mirrors to be adjusted its angle and vertical and translational position.

The beam entering into the central vacuum chamber goes through the polarized beam splitter to match it's linear polarization to the beam splitter, and partly reflected by the suspended sample mirror for the absolute control. The beam splitter divides the beam in half power. The divided beams illuminate both arms through the entrance holes of near mirrors after they are modulated in phase at 9.83 MHz with Pockels cells. The optical delay-line path involves 102 reflections between the near mirror and the end mirror forming a 10 km optical path length. The beams return through the same entrance holes and are recombined with each other at the beam splitter. This recombined beam was locked at the dark fringe to derive the signal of gravitational waves.

According to the characteristic of the beam splitter, the recombined beam at the other port is locked at the bright fringe after the dark fringe locking operation. This beam recombined to the bright fringe is "re-recombined" at the beam sampler with the sampled input beam reflected by the suspended mirror with the Slow PZT. This recombined beam is also locked at the darkfringe for the absolute control (described in Chapter 5).

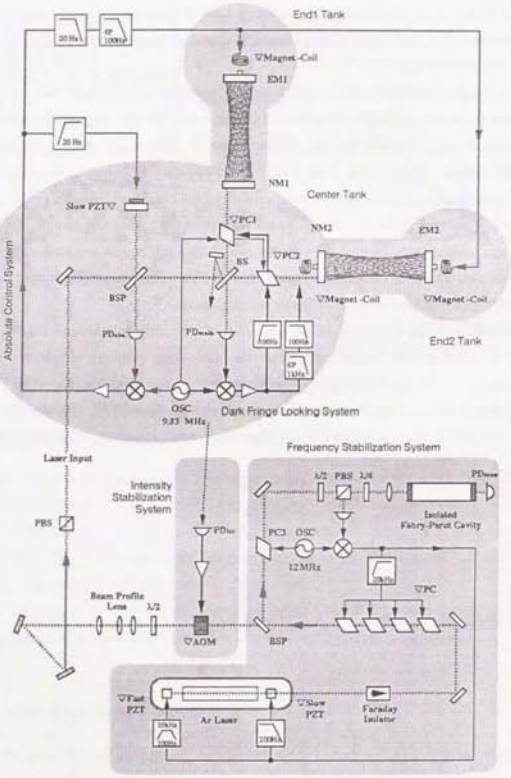

Figure 4.28: The optical design of TENKO-100

Chapter 5

Sources of Noise

In this chapter, noise sources of laser interferometric gravitational wave detectors are described. The correspondent noise reduction systems used in TENKO-100 for each noise are also explained and evaluated.

5.1 Quantum Noise

The quantum noise is based on the uncertainty principle and it limits the ultimate measurement accuracy of the distance between two mirrors. In the case of a Michelson interferometric gravitational wave detector, quantum noise is given by

$$\Delta x \Delta p \geq \hbar \rightarrow \Delta x \geq \sqrt{\frac{\pi\tau\hbar}{M}} \rightarrow \frac{1}{2\pi\nu L}\sqrt{\frac{\pi\hbar}{\tau M}} \quad . \tag{5.1}$$

M	:	Mass of mirror	[kg]
L	:	Distance of two mirrors	[m]
ν	:	Frequency of gravitational wave	[Hz]
τ	:	Observation time	[sec]
$\hbar$	:	Plank's constant / 2π	[J·s]

In the case of a resonant type detector, the quantum noise also limits the sensitivity of the detector if thermal noise is sufficiently reduced. On the other hand, in the case of laser interferometric detectors, the quantum noise of even prototypes, for example TENKO-100 at ISAS, reaches $h = 5 \times 10^{-22}\ 1/\sqrt{\text{Hz}}$ at 100 Hz, and can be improved by a longer base-line. Thus, the quantum noise based on the uncertainty principle can be smaller than expected signals due to gravitational waves so that we can neglect its effects.

In the case of interferometric detectors where signals of gravitational waves are detected as a laser intensity change of the interfered beams, the change of intensity caused by quantum noise is much smaller than that due to the photon counting error (detailed in this Chapter). This statistical error of the photon counting is known as photon shot noise, which is realistic limitation of the sensitivity and detailed in the subsection "Shot Noise" in this Chapter.

5.2 Seismic Noise

5.2.1 Seismic Noise around TENKO-100

Four main mirrors and a beam splitter must behave as free masses in order that an interferometer works as a gravitational wave detector. It is easy to let mirrors fall freely in space, but difficult on the earth. Instead of free falling mirrors, we can obtain the same performance by suspending them with thin wires. However, by suspending them, it becomes inevitable that the displacement will be disturbed by the ground motion through wires. Although the ground motion, *i.e.* the seismic noise, varies with the location of interferometers, its typical vibration amplitude is described as following :

$$\Delta x = 10^{-7}\left(\frac{1}{f}\right)^2 \quad \left[\mathrm{m}/\sqrt{\mathrm{Hz}}\right] \quad , \tag{5.2}$$

which is characteristic of the decreasing amplitude due to a f^{-2} law for the frequency range above 0.1 Hz and flat for the frequency range below 0.1 Hz. The factor is around 10^{-7} in the city, for example, Sagamihara City where TENKO-100 is located, while it falls around $10^{-8} \sim 10^{-9}$ in mines or deserts providing the most reliable site for a km-class interferometer. We measured the displacement of a bottom plate where many optics of the interferometer were located in the center tank as well as the displacement of the end tanks by accelerometers. As Figure 5.1 shows, the seismic noise around TENKO-100 in ISAS was not only about 10 times worse than the typical level in view of the floor level, but also had many peaks on the displacement spectrum. It was mainly because one arm of the interferometer was located along a busy road by only five meters away. The total contribution of the seismic noise was multiplied by the reflection number of 102 from $\Delta x = 10^{-11}$ m/$\sqrt{\ }$ Hz to $\Delta L = 10^{-9}$ m/$\sqrt{\ }$ Hz at 100 Hz. This indicated that we needed

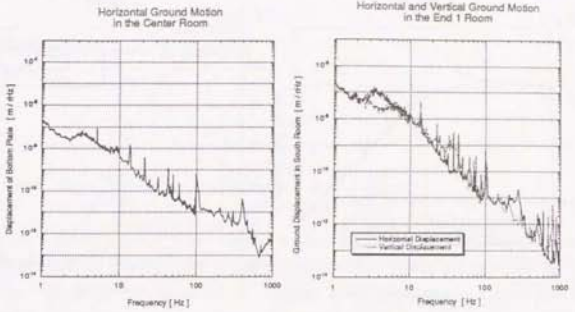

Figure 5.1: The displacement of bottom plates in the center tank and the end tanks

140dB isolation of the mirror displacement at 100 Hz to achieve the targeted sensitivity of $2\times10^{-20}\,1/\sqrt{\ }$ Hz. Although the mirror suspension by a single pendulum also had the effect of isolation of 80 dB at 100 Hz by itself, an additional or new type of isolation systems were needed. For example, a multiple pendulum alike a double or triple pendulum [38, 42], a stack [40] and an X-pendulum [41] with about $\sim$ 78 sec resonant period, were proposed to attain the requested isolation ratio. In this sense, the sensitivity in low frequency of interferometric gravitational wave detectors are dominated by the seismic noise.

5.2.2 Seismic Noise Isolation

Single Pendulum

Generally, a single pendulum has a transfer function $H_{1P}(f)$ as follows

$$H_{1P}(f) = \frac{dx}{dy} = \frac{f_0^2 + if f_0/Q}{f_0^2 - f^2 + if f_0/Q} \quad , \tag{5.3}$$

where

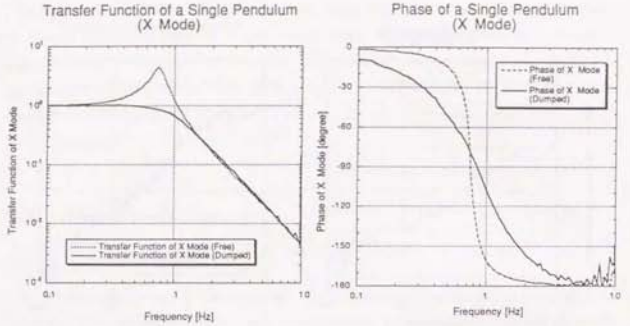

Figure 5.2: The transfer function and the phase of a single pendulum
The transfer function and the phase of a single pendulum is denoted by the dotted curve. The solid line shows one damped critically by the local control.

dx	:	Displacement of a suspended mass	[m]
dy	:	Displacement of a suspending point	[m]
f_0	:	Resonant frequency of a pendulum	[Hz]
f	:	Frequency	[Hz]
Q	:	Q value of resonance	

which is simplified by the approximation in the limit where $f \gg f_0$ and $Q \gg f/f_0$, to the following equation:

$$H_{1P}(f) = \left(\frac{f_0}{f}\right)^2 \quad . \tag{5.4}$$

It can be seen that a single pendulum works as a 2-pole low pass seismic noise filter as shown in Figure 5.2, and that more effective isolation ratio can be obtained by setting the resonant frequency (f_0) of a pendulum as low as possible. However, it is inevitable to enhance the motion of a mirror at resonant frequency, and the wire resonance well-known as a violin mode (f_w) decreases this isolation ratio over f_w as follows

$$H_{1P}(f) = \left(\frac{f_0}{f_w}\right)^2 \frac{f_w}{f} \quad , \tag{5.5}$$

where the wire resonance f_w is given by

$$f_w = \frac{1}{2\ell_w}\sqrt{\frac{T}{S\rho}} \quad . \tag{5.6}$$

T	:	Tension of a wire	[N]
S	:	Safety factor	
ρ	:	Density of a wire	[kg m^{-3}]
ℓ_w	:	Length of a wire	[m]

We can reduce the excited mirror motion by damping it actively with the local control feedback system. It is desirable to use a short and thin wire to increase the first wire resonant frequency from where the f^{-1} isolation starts [42]. This is in conflict to the isolation activity because the pendulum with a shorter wire length has a higher resonant frequency from where the f^{-2} isolation becomes effective. In addition, the line density of a wire is also limited by the demand of suspending a heavy main mirror weight of 17 kg. Thus, there exists an optimum wire length and a line density. In TENKO-100, tungsten wires with $\phi = 0.45$ mm and with the minimum strength necessary to suspend the main mirrors were used. The wire had the first wire resonant frequency of 128 Hz which was just a little over the minimum target frequency of TENKO-100 of 100 Hz. Furthermore, the main mirror pendulum could not be thought of a simple pendulum with a point mass since the length between the center of the main mirror and the suspending point was only about four times as long as the radius of a main mirror. It was not so important from the point of view of the seismic noise isolation, but very important in the point of view of a mirror alignment control design. The difference in motions between the top and the bottom of the mirror should have been considered.

In addition, 80dB isolation ratio at 100 Hz obtained with the single pendulum was insufficient. We should have used a double pendulum system, a stack system and any other different kinds of mechanical isolation techniques to obtain additional 80dB isolation ratio.

Double Pendulum

Deriving from the isolation ratio of the single pendulum, the isolation ratio of an n-stage suspension system between the pendulum resonant frequency and the first resonant frequency of the wire can be expressed roughly as [42, 45, 46]

$$H_{NP}(f) = \left(\frac{f_0}{f}\right)^{2N} \quad . \tag{5.7}$$

f_0 : The highest pendulum resonant frequency [Hz]
f : Frequency [Hz]

So, an isolation ratio of 160dB at 100 Hz can be obtained with two-stage (double) pendulum and this type was used for the beam sampler suspension for the absolute control.

In contrast to the active damping of the local control system, the lower mass (corresponding to an optical component) of the double pendulum is damped indirectly through a position coupling with the upper mass (usually made of copper or aluminum) which is directly damped by eddy current induced by strong magnets located closely around it. In addition, the support stage for these magnets is equipped at the end of a thin metal plate which provides isolation performance alike a pendulum, otherwise the isolation ratio for the frequency range just above the resonant frequency of the plate obeys f^{-3}, not f^{-4}. In order to control the mirror motion, the suspension points of the upper mass are actuated by PZTs, not a magnet-coil coupled force to the mirrors as in the local control system used for TENKO-100 in order to prevent the system noise of the local control such as circuit noise from disturbing the isolated mirror displacement.

Figure 5.3 and Table 5.1 shows the 2-stage pendulum setup for the beam sampler suspension. The upper mass was made of a copper rod and it was suspended with two wrapping piano wires at 22 cm. It was damped with eddy current through six flat cylindrical Fe-B-Nd magnets fixed on the end of the aluminum thin plate. The lower mass consisted of a beam sampler with a holder made of copper. It was also suspended from the upper mass with a single wrapping wire at 20 cm. Figure 5.4 shows the isolation ratio obtained by this configuration .

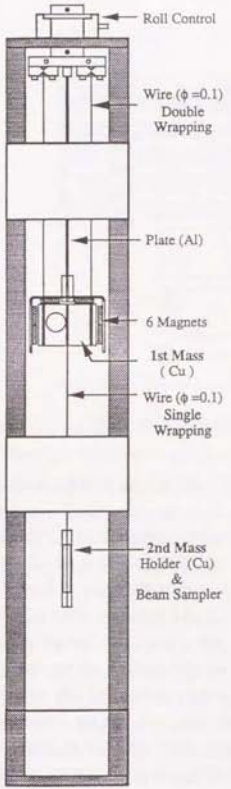

Figure 5.3: The setup of the double pendulum

Double Pendulum for the Beam Sampler of the Absolute Control	
1st Mass	Double Wrapping
Materials	Copper
Dimensions	ϕ40 [mm] × 80 [mm]
Weight	1.2 [kg]
Wire	ϕ0.1 [mm] × 220 [mm] Piano Wire
2nd Mass	Single Wrapping
Materials	Copper Ring Frame Beam Sampler
Dimensions	ϕ70 [mm] × 8 [mm] ϕ50 [mm] × 5 [mm]
Weight	0.25 [kg]
Wire	ϕ0.1 [mm] × 210 [mm]
Damping Magnet	6 Units for 1 Mass
Subscribe	Nd-B-Fe
Dimensions	ϕ20 [mm] × 5 [mm]
Resonance	
1st	0.8 [Hz]
2nd	2.0 [Hz]

Table 5.1: Specifications for the double pendulum

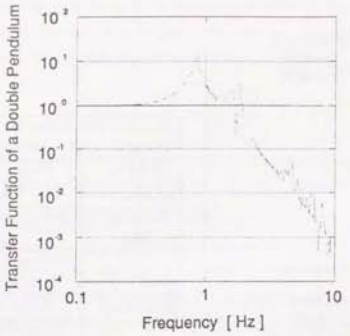

Figure 5.4: The transfer function of the double pendulum

Stack Isolation

In addition to the single pendulum, more than four orders of magnitude isolation ratio at 100 Hz was required for TENKO-100 to decrease the seismic noise down to the shot noise level. In this sense, it was quite useful to use a vibration isolation stack, consisting of alternating layers of rubber and dense compact mass, usually made of viton for the rubber and of lead or stainless steel for the mass. Elasticity of the half-pressed rubber by the dense mass provides a high isolation ratio over the resonant frequency of the stack due to the characteristic elasticity of the rubber blocks, stiff in compress (vertical) and soft in shear (horizontal). The stack can be compact, so we can obtain a very high isolation ratio by stacking up a number of layers. In addition, the stack has not only horizontal but also vertical isolating performance, and the amplification by resonance of the rubber is well-damped by itself in contrast to a pendulum. But, it is difficult to obtain isolation in the low frequency range under about 10 Hz in both directions because the resonant frequency of a stack is rather higher than a pendulum. It is more difficult to understand the isolation mechanism precisely for the following reasons : (1) the mass layers have

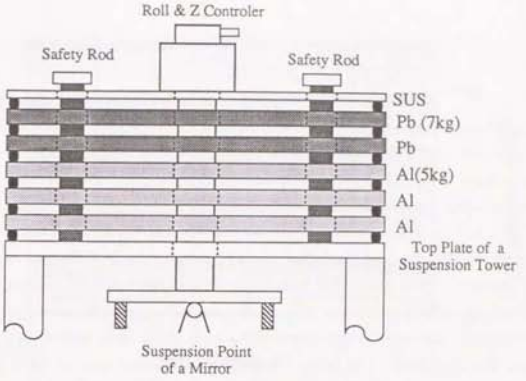

Figure 5.5: The setup of the stack designed by R.Takahashi (NAO)

complicated couplings of translational, rotational degrees of freedom, (2) the internal modes of layers are complicated, (3) the elasticity of rubber has a non-negligible complicated frequency response. As a result, cut and try was often made to determine a design of the stack.

The structure of the stack used in TENKO-100 is shown in Figure 5.5. They consisted of two layers of lead plates (10 kg each), three layers of aluminum plates (5 kg each) and one plate of stainless steel of 7 kg. The transfer function of the stack in horizontal motion is shown in Figure 5.6. It was measured by taking the ratio of the amplitude of the displacement fluctuation between the top of the stack and the suspended mirror with the accelerometers equipped at each position. The transfer function was complicated, and it showed that the isolation ratio of 5×10^3 at 100 Hz with respect to horizontal motion was achieved without sharp peaks of resonances to disturb the mirror alignment control. One needed to take into consideration that the stack's isolation ratio for horizontal motion depended strongly on the slight difference of the stack structure. For example, the difference in the shape and the attachment position of the rubber blocks and masses could cause a large effect on the interferometer. A part of the vertical seismic noise damped insufficiently might deteriorate the horizontal mirror motion.

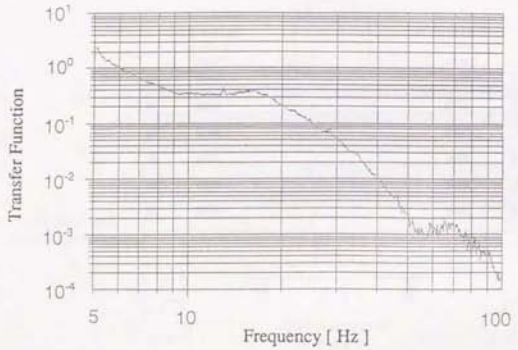

Figure 5.6: The transfer function of the stack
This transfer function measured by AKASHI ASE-B335 in ISAS for vibration test of satellites. It can actuate 1mm displacement with sinusoidal wave from 5 Hz to 100 Hz

Bottom Plate Pendulum

As described, the shock wave noise caused by the cars passing near the west side of TENKO-100 disturbed the interferometer control in addition to the high floor level of the seismic noise. The stack isolation for the bottom plates, where many optics were fixed such as mirror suspension towers, Pockels cells and so on, would be the most preferable because of its simplicity, and the dense mass of the bottom plates themselves, whose weight reached 300 kg including the optics. However, since there was not enough space to insert stack layers effectively, the idea could not be applied. In order to protect them from the seismic shocks, all bottom plates were suspended by three wires alike pendulums (see in Figure 5.7). Resonant motions of the heavy bottom plates, 1.1 Hz in the translational motion and 1.7Hz in the torsional motion, were damped by eddy current with strong magnets (see in Figure 5.7). Figure 5.8 shows the effect of the isolation of the bottom plate suspension. An average isolation ratio of 20dB was achieved, but the internal modes of the bottom plate and wire resonances around 15 Hz were slightly amplified because of its thinness of 3 cm for its diameter of 150 cm. The shock waves were also damped, therefore,

continuous operational locking time was increased.

Total Performance of Seismic Noise Isolation

Figure 5.9 shows the effect of the total seismic noise isolation in the sensitivity of TENKO-100 in low frequency range. The thin gray curve is the displacement of the mirror without the stack nor the bottom plate suspension (suspended bottom plates were fixed by the friction of many metal plates which stuck out of the bottom plates and contacted with the walls of tanks), while the solid curve shows one with both isolations. The attained displacement level was almost in agreement with the calculated level from the bottom plate displacement and the integration of the isolation ratio of the single pendulum, the stack and the bottom plate suspension under 40 Hz. The peaks around 15 Hz were the wire resonance of the bottom plate suspension which were also seen in Figure 5.8. Although the increase of 50 Hz was also observed in the transfer function of the stack (Figure 5.6), the detailed structures and the amount were quite different, and the displacement level around 100 Hz was $\sim$ 40dB larger than the expected level.

5.3 Optical Noise Sources

5.3.1 Shot Noise

Shot Noise Performance

The optical path fluctuation perturbed by a gravitational wave is detected as the optical power fluctuation of the interfered beam at the output of the interferometer. Photons from the interferometer are transformed at photo-detector into electrons with some ratio. In this process when photons with a mean number $N = \tau\bar{n}$ are counted during one measurement interval τ, the counted number of photons have some probability distribution $P(n)$ due to the quantum nature characterized by a Poisson distribution as follows

$$P(n) = \frac{\bar{n}^n e^{-\bar{n}}}{n!} \quad . \tag{5.8}$$

In the limit that $n \gg 1$, Eq 5.8 becomes $\sqrt{\bar{n}}$, which is well-known as the photon counting error. This means that the amount of photon counting error, so called the shot noise, and the change of photo current induced by a gravitational wave cannot be distinguished. The

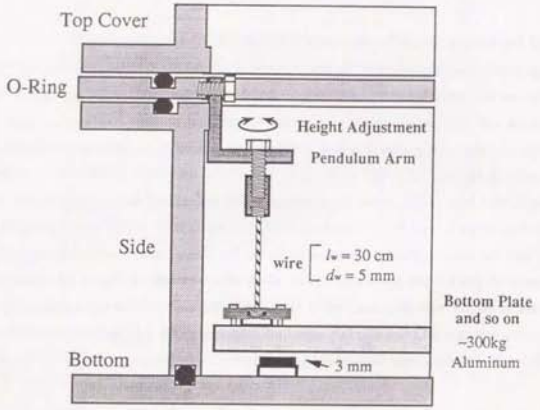

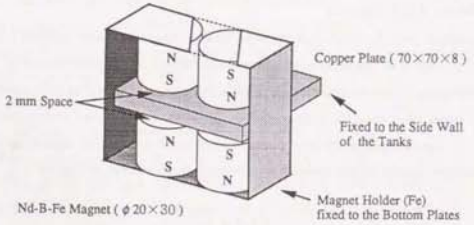

Figure 5.7: The suspension system and eddy current damping of the bottom plate

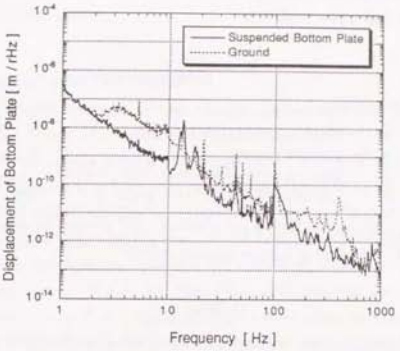

Figure 5.8: The effect of the bottom plate suspension

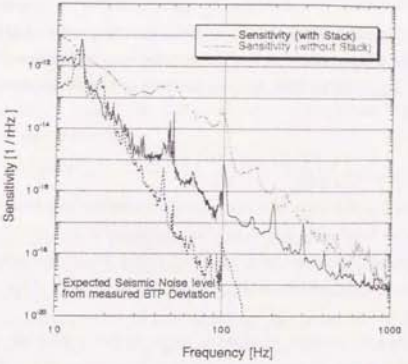

Figure 5.9: The total effect of the seismic noise isolation

photon shot noise limits practically the sensitivity of an interferometer. The photo-current induced with the light power is given by

$$I_0 = e\frac{\eta P_0}{2\pi\nu\hbar} \quad . \tag{5.9}$$

P_0	:	Effective laser power	[A]
I_0	:	Photo current induce by P_0	[W]
e	:	Electron charge	[C]
η	:	Photo current efficiency of photo-detector	
ν	:	Frequency of a laser (wave length = λ)	[Hz]

According to the argument of the photon counting error, the shot noise of photo current can be expressed in the form of a power spectral density:

$$\sqrt{2eI_0} \quad . \tag{5.10}$$

The ratio of the signal to noise determines the detectable phase limitation of the interferometer as follows

$$\Delta L_{\rm shot} = \sqrt{\frac{\pi\nu\hbar}{\eta P_0}} \quad . \tag{5.11}$$

In the application of the darkfringe locking to detect the change of the optical path length (phase modulation is often used), the modulation index (m), the contrast (K) and photo-detector's noise (I_{det}) must be taken into consideration as follows (for the internal modulation technique)

$$\Delta L_{\rm shot} = \frac{\lambda}{\pi}\sqrt{\frac{e}{2I_0}}\frac{\sqrt{1 - KJ_0(m) + 2I_{\rm det}/I_0}}{KJ_1(m)} \quad \left[\mathrm{m}/\sqrt{\mathrm{Hz}}\right] \quad . \tag{5.12}$$

This formula indicates that there exists an optimum modulation index which provides the minimum shot noise limiting the sensitivity of an interferometer for a given contrast. Practically, it becomes very important to choose the optimum modulation index to minimize the shot noise level which limits the sensitivity of TENKO-100 in the range of 800 Hz to 2 kHz.

The shot noise level can be easily improved by increasing the injection laser power because the signal to noise ratio for the shot noise decreases with the square root of the laser power. But at the same time, the mirrors also suffer from the fluctuation of the laser pressure which

is characterized by quantum nature of the photons alike the shot noise, *i.e.* Radiation Pressure noise detailed in later.

Noise Characteristics in TENKO-100

Figure 5.10 shows the measured relation between the shot noise and the laser power of the bright fringe. Dotted points with error bars indicate the measured shot noise level under an uniform modulation index of $m \approx 0.2$ rad, and the contrast of $K = 95$ % which had a negligible fluctuation, and the solid line is a least square fit for the measured data, and the dotted line is the theoretical shot noise level. They were in good agreement with the theoretical relation except for the level. As the laser power increased, the measured shot noise began to part from the theoretical shot noise level. This meant unknown noises existed at the level of $\sim 10^{-16}$ m/$\sqrt{}$ Hz. One of the possibilities was the Johnson noise of the photo-detector, 2×10^{-16} m/$\sqrt{}$ Hz. The second were the frequency noise itself limited by the stability of the reference cavity (10^{-16} m/$\sqrt{}$ Hz corresponding to $\sim$ 100 mHz/$\sqrt{}$ Hz) and the frequency noise coupled with the excess scattered light. The third was the non-stationary scattered light noise.

The shot noise level in TENKO-100 would be suppressed much more with our high power Ar^+ ion laser with 8 W in a single mode (TEM_{00}). But, in practice, the photo-detector could not resist continuous high power illumination ($P_{in} \geq 1$ W, $P_{eff} \geq 200$ mW). In addition, various noises which exceeded the present shot noise were dominant in the sensitivity of TENKO-100, especially, under 1 kHz which was the most interesting frequency range for the gravitational wave detection.

5.3.2 Frequency Noise

Noise Characteristics in a Delay-Line Interferometer

To detect the displacement between two mirrors with one optical path of an interferometer, the laser frequency (or wave length) fluctuation limits the precision of this measurement unless it is well-stabilized below the shot noise level. But in the case of the actual interferometer with two optical paths, the frequency noise can be rejected by the symmetrical interferometer construction, so called Common Mode Rejection (CMR).

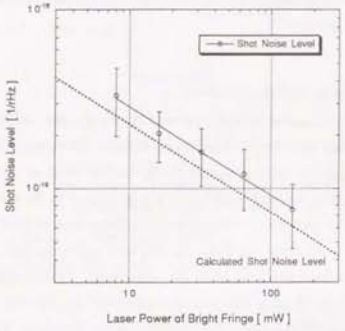

Figure 5.10: The relation between the shot noise and the laser power of the bright fringe

The difference in the two optical path lengths produces the frequency noise (ΔL_f) as follows

$$\Delta L_f = \frac{\delta\nu}{\nu} dL \quad \left[\mathrm{m}/\sqrt{\mathrm{Hz}}\right] \quad . \tag{5.13}$$

dL	:	Difference of the both optical path lengths	[m]
$\delta\nu$	:	Fluctuation of the laser frequency	[Hz/$\sqrt{\mathrm{Hz}}$]
ν	:	Laser frequency	[Hz]

This reveals that the frequency noise can be completely suppressed if dL was set to 0, and that dL is a straightforward indicator of the requirement for the frequency stabilization. In the case of TENKO-100, the difference of the optical path lengths, 10^{-4}m, produces an equivalent displacement sensitivity of 1.8×10^{-16} m $\sqrt{\ }$ Hz, with the free run laser frequency noise of 10^3 Hz/$\sqrt{\ }$ Hz at 1 kHz. It could not be expected to match the path lengths within 1 m since the radii of the mirror curvatures could not be matched equally within 1 cm accuracy over the base-line of 100 m as mentioned in Chapter 4. In fact, several meter light path difference was produced if I tried to realize individually the re-entrance condition

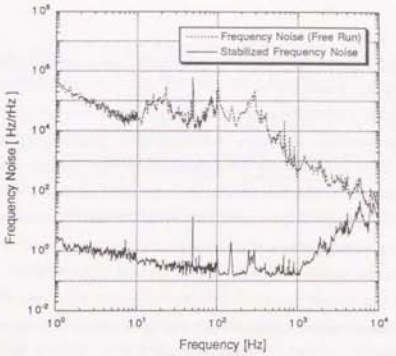

Figure 5.11: The frequency noise

in each light path. If more than 12 cm difference of the curvature radii was produced, the path length difference was increased by 400 m because it was the same value to change the reflection number by four. In addition, the anisotropy in the radius of curvature in one mirror was expected to produce transverse shift of the re-entrance position due to the accumulation of deviation from the ideal reflection path during the Delay-Line trip. In general, it cannot be compensated with any mirror alignment or arm length adjustment.

In the case of TENKO-10, the high quality mirrors with the equal radius of curvature around 10 m within less than 1.5 mm accuracy, enabled us to match the two optical path lengths to less than 1 mm over 1 km total optical path length. This provided a 120dB of CMRR (Common Mode Rejection Ratio), so the frequency noise could be completely suppressed under the shot noise level. In the case of TENKO-100, the optical path length difference was decreased to about 2 m (70dB CMRR) by deforming the best re-entrance conditions in each arm, and finally, a transverse shift of the re-entrance beam prevented us from matching it. Figure 5.11 shows the un-stabilized frequency noise. This 70dB CMRR and the measured free running frequency noise revealed that the required stabilized frequency noise level was less than $\sim$ 100 mHz$\sqrt{\ }$ Hz and that 70dB open loop gain was required for the frequency stabilization system.

Pound Drever Method

We can suppress the frequency noise for the frequency range less than 10 kHz around 100 mHz/$\sqrt{}$ Hz with the Pound-Drever Method [43, 44] in which three frequency tunable actuators (a Slow PZT, a Fast PZT and outer Pockels Cells) are used if the reference cavity is well isolated from the seismic noise and the acoustic noise. Figure 5.12 shows the optical setup. About 10 mW of the main laser beam was sampled and injected into the reference cavity. The reference cavity had two mirrors with the same curvature radii of 25 cm at either both end of the cylindrical rod, and had finesse of 300 with a corner frequency of 600 kHz. The Cavity was suspended as a single pendulum by two piano wires at the base of a suspension platform and damped with eddy current induced by the attached magnets. The suspension system was located in a small evacuated chamber which was also put on the top plate of the same seven layers stack used in the main mirror isolation system. Before injected into the reference cavity, the sampled beam was longitudinal linearly polarized and was modulated in phase with a 12.0 MHz sinusoidal signal by a Pockels Cell (PM-25). The polarization was then transformed into a circular through a quarter-wave plate shifter after a PBS, and its wave front was adjusted to the cavity mirror curvature with a lens. The interfered beam between the beam reflected on the optical plate in front of the cavity which involved 12.0 MHz side band and the reflection beam from the cavity which was well stabilized in frequency due to the elimination property without resonant frequencies, traveled through the quarter-wave phase shifter again and was transformed into a beam with transverse polarization . There, it was reflected by the PBS and detected with a resonant type photo-detector. The lower frequency range of the demodulated signal ($\lesssim$ 200 Hz) was fed back to the Slow PZT attached to the front mirror of the laser. The middle frequency range (200 Hz ~20 kHz)was fed back to the Fast PZT attached to the rear mirror and the high frequency range ($\gtrsim$ 20 kH) to the four Pockels Cells located successively on the beam axis outside the laser in an optical system loop. Their specifications are shown in Table 5.2. At first, we tried a system with two paths including the Slow PZT and the Fast PZT, before establishing the three paths system.

Figure 5.13 shows the output beam transmitted from the cavity and the correlated demodulated signal. They were obtained by sweeping the length of the cavity by the Slow PZT attached to one of the cavity mirrors. The efficiency [V/Hz] of the demodulated signal is given by

Actuators	Slow PZT	Fast PZT	Pockels Cell
Dimension	$\phi 25 \times 25$ [mm] Cylindrical	$\phi 7 \times 2$ [mm] Plate	5 [mm] $\times$ 5 [mm] Crystal
Efficiency	8.5 [nm/V]	0.54 [nm/V]	0.32 [nm/V]
1st Resonance	30kHz	280kHz	$\geq$ 1MHz
Manufacture	Fuji Ceramics	Fuji Ceramics	Gsänger

Table 5.2: Specifications of the SlowPZT, the FastPZT and the Pockels cell

$$\frac{V_{p-p}\mathcal{F}}{\mathrm{FSR}} \quad . \tag{5.14}$$

V_{p-p} : Voltage for peak to peak swing of a demodulated signal
FSR : Free spectral range of a cavity
$\mathcal{F}$: Finesse of a cavity

Although the frequency noise stabilized relatively to the cavity could be estimated from the demodulated signal, the actual frequency stability was dominated by the stability of the cavity length excited by the seismic noise and the acoustic noise. Therefore the seismic noise isolation of the cavity was quite important.

The actual frequency stability can be measured from the demodulated signal from an additional Pound-Drever system in which the stabilized laser frequency is also locked to another more stabilized Fabry-Perot cavity. In the case of the Fabry-Perot type interferometer, one arm is often used for the reference cavity for the measurement of the frequency noise. In the case of the Delay-Line interferometer, we can regard, as a reference, the optical path over the cross frequency where stabilization of the Delay-Line optical path determined by extremely isolated mirrors becomes smaller than the equivalent displacement fluctuation determined by the stabilized frequency with a rigid Fabry-Perot cavity. We used the latter method.

Feedback Servo Design

At first, the block diagram and the bode diagram of the feedback servo for the two paths system are shown in Figure 5.14 and Figure 5.15, respectively. The cross over frequency of the Slow PZT path and the Fast PZT path was around 100 Hz. The unity gain frequency

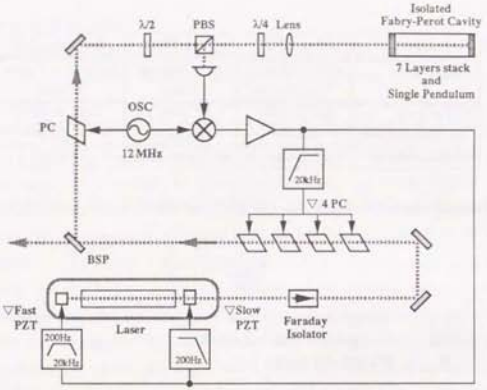

Figure 5.12: The Pound-Drever method for the frequency stabilization

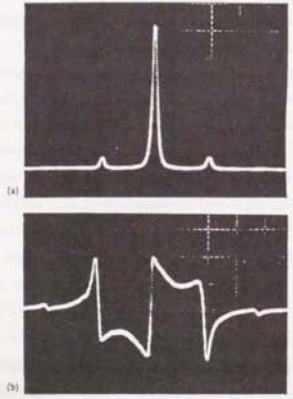

Figure 5.13: The transmitting beam signal (a) and the demodulated signal (b)

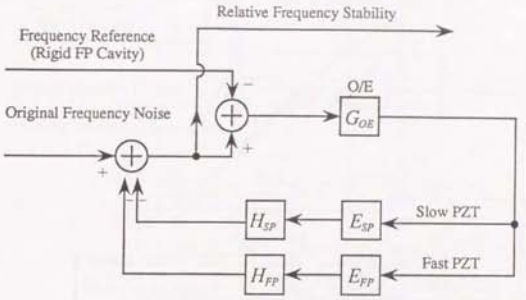

Figure 5.14: The feedback block diagram for the two paths frequency stabilization

was limited below 20 kHz because of the mechanical resonance of the mount of the PZT of 3 kHz. To compensate the phase delay due to the mechanical resonance due to the PZTs, a step up circuit was inserted on the Fast PZT path and the Slow PZT path. To keep the stable locking and obtain large open loop gain enough to stabilize the frequency around shot noise level (limited by the incident laser power), the total gain was enhanced by a f^{-4} slope at 5 kHz with a gain integration circuit after initial locking. The measured open loop gain curves were in good agreement with the original design. In this system, we obtained 65dB open loop gain and enough frequency stability at 1 kHz, but frequency over 3 kHz was not fully stabilized because of the low unity gain frequency.

To enlarge the unity gain frequency, we tried the three paths system. Figure 5.16 and Figure 5.17 show the block diagram and the bode diagram of the feedback servo for the three paths system respectively. A cross over frequency between the Slow PZT path and the Fast PZT path was set to 300 Hz, and to 10 kHz between the Fast PZT path and the Pockels cell path. A step up circuit around 15 kHz was inserted on the Slow PZT path and the Fast PZT path to compensate the phase delay. Total open loop gain was enhanced by

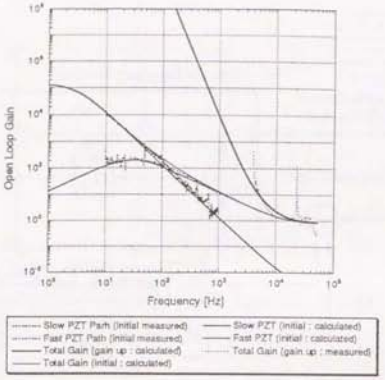

Figure 5.15: The feedback bode diagram for the two paths frequency stabilization

a f^{-1} slope at 100 kHz and 50 kHz with two gain integration circuits after initial locking. We could obtain 35dB open loop gain at 10 kHz and 90dB at 1kHz, and enough stability under 10 kHz (Circuit design is detailed in Appendix E).

Stabilized Frequency Noise

With the two paths system, the frequency noise before and after the stabilization control are shown in Figure 5.18. The frequency noise of the free running laser was driven from the feedback signal to all actuators (denoted by a thick dotted curve) and it was in good agreement with the sensitivity of TENKO-100 (denoted by a thick solid curve). The stabilized frequency from the demodulated signal is denoted by a thin dotted curve, and it was barely below the attained sensitivity below 3 kHz. The shot noise level due to 10 mW incident laser power was about $\sim 1 \times 10^{-1}$ Hz/$\sqrt{}$ Hz, so it was comparable to the attained demodulated signal. The frequency might be stabilized to about 0.2 Hz/$\sqrt{}$ Hz at 1 kHz resulted from the 65dB stabilization.

Figure 5.19 shows the measurement apparatus for the actual frequency stability. In

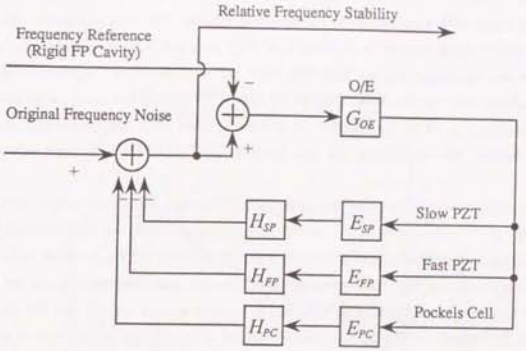

Figure 5.16: The feedback block diagram for the three paths frequency stabilization

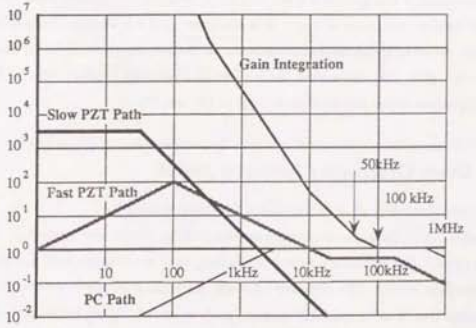

Figure 5.17: The feedback bode diagram for the three paths frequency stabilization

this interferometer with 10 km optical path difference, the interfered fringe was locked at dark fringe with a proper feedback system as follows : the high frequency part of the demodulated signal was fed back to the Slow PZT attached to the suspended mirror, and the low frequency part was fed back to a main mirror. The actual frequency noise could be measured from the feedback signal to the Slow PZT for the frequency range above the cross frequency at which the stability determined by the Delay-Line optical path provided by the isolated mirrors became less than the equivalent stability of the rigid Fabry-Perot cavity.

Figure 5.20 shows the measured actual frequency noise spectrum denoted by a solid curve. It showed that the floor level (0.2 Hz/$\sqrt{}$ Hz) was comparable with the value calculated from the demodulated signal denoted by a dense dotted curve over 100 Hz, but that some excess noise existed around 800 Hz. Although the expected cross frequency would be 30 Hz for the frequency stability of 0.2 Hz/$\sqrt{}$ Hz, it became around 100 Hz and the spectrum between 30 Hz and 100 Hz did not match with the expected level of the isolated mirror's displacement denoted by thin solid line. It showed unknown noises existed around 100 Hz as also observed in the sensitivity spectrum.

With the three paths system, the relative frequency noise before and after the frequency stabilization control is shown in Figure 5.21. The stabilized frequency with the two paths is denoted by a dotted curve and one with the three paths is denoted by a solid curve. It showed that we obtained drastic improvement of the frequency stability for the frequency range above 1 kHz. We can expect the frequency noise over 3 kHz shown in Figure 5.18 can be suppressed under the shot noise level in the sensitivity.

5.3.3 Laser-Originated Intensity Noise

Noise Characteristics in a Delay-Line Interferometer

Any signal has a signal to noise ratio determined by the intensity noise of the original light (δI) against the stationary power (I) as long as it is obtained from the power signal of the same light source. The detected intensity fluctuation of the interfered beam locked at dark fringe due to other possible sources, such as seismic noise, frequency noise and so on, as well as, a gravitational wave, has at least a component of the noise proportional to the signal to noise ratio ($\delta I/I$) determined by the same ratio of the intensity noise of

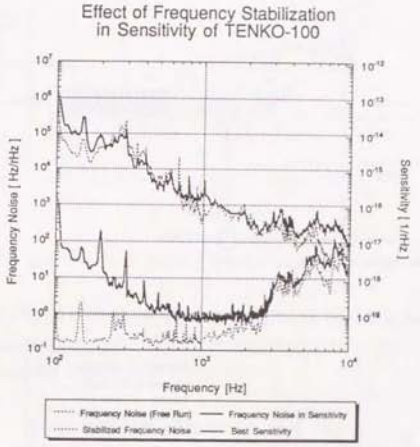

Figure 5.18: The frequency noise before and after the frequency stabilization control in the sensitivity

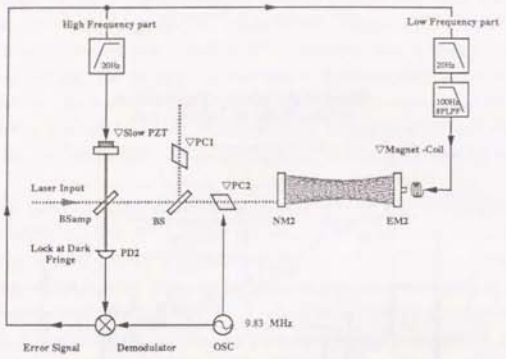

Figure 5.19: The setup for the measurement of the practical frequency stability

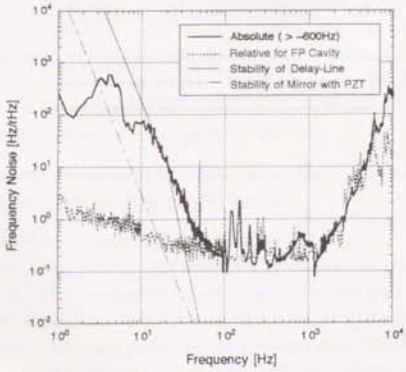

Figure 5.20: The actual frequency stability

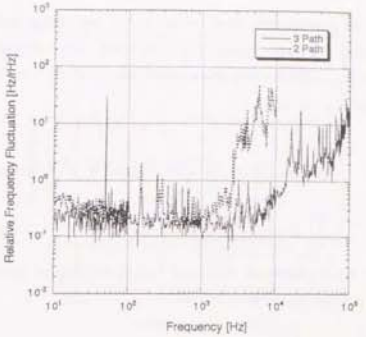

Figure 5.21: The relative frequency stability with the two paths system and the three paths system

the original laser beam. The largest intensity fluctuation, or the displacement, is usually excited by the seismic noise in low frequency range to provide the dominant intensity noise coupled to the original intensity noise $\delta I/I$, given by

$$\Delta L_{int} = \frac{\delta I}{I}\delta L_{lowf} \quad \left[\mathrm{m}/\sqrt{\mathrm{Hz}}\right] \quad . \tag{5.15}$$

ΔL_{int} : Intensity Noise
I : Intensity of a laser
δI : Intensity fluctuation
δL_{lowf} : Residual dark fringe fluctuation caused by the seismic noise (enough low frequency range)

The residual dark fringe fluctuation can be obtained by dividing the natural displacement of the total optical path length in the low frequency by the open loop gain of the corresponding frequency of the dark fringe locking servo. In addition, the deviation of the dark fringe point decreases it by the ratio of the intensity at the shifted dark fringe over an ideal point.

The intensity noise can be rejected by the perfect dark fringe locking meaning $\delta L_{lowf} = 0$. This is usually realized with the phase modulation method which is an essential technique

for the interferometric gravitational wave detection, the dark fringe locking (detailed in Chapter 4). Assuming the phase modulation of the laser with a sinusoidal wave whose angular frequency is $\omega_{\rm mod}$ and the amplitude (modulation index) is m, the output signal of the photo-detector is given by

$$I_{PD} \approx \frac{I_0 + \delta I}{2}\left[1 - J_0(m)\cos(\Phi_0 + \delta\phi) + 2J_1(m)\sin(\Phi_0 + \delta\phi)\sin\omega_{\rm mod}t\right] \quad . \qquad (5.16)$$

Φ_0 : Residual dark fringe fluctuation
$\delta\phi$: Displacement signal

The contribution of the displacement signal and that of the original intensity noise in the demodulated signal can be separated as follows

$$I_{DC} = \frac{I}{2}(1 - J_0(m)\cos\Phi_0) + \frac{\delta I}{2}(1 - J_0(m)\cos\Phi_0) \quad ,$$
$$I_{SIG} = I_0 J_1(m)\sin\Phi_0 + I_0 J_1(m)\left[\frac{\delta I}{I_0}\sin\Phi_0 + \delta\phi\cos\Phi_0\right] \quad .$$

The first term corresponds to the contribution to the shot noise since the phase modulation frequency is selected at a high frequency ($\geq$10 MHz) where the intensity noise falls to the shot noise level. The second term involves signals of the displacement and the intensity noise separately. With the perfect dark fringe condition, *i.e.* $\Phi_0 = 0$, the intensity noise term falls to 0.

Figure 5.22 shows the relation between the deviation from the dark fringe and the correspondent output noise in the sensitivity of TENKO-100 when we applied 1 kHz intensity noise of 2×10^{-5}. It was in good agreement with Eq 5.15 and we could understood the effect of intensity noise suppression around 0 μm. But, We couldn't verify this relation within the scale of 10^{-10} m deviation of the dark fringe, which meant that the dark fringe fluctuated in the same scale. One of reasons was that the residual coupling modes of R and P motion to X motion fluctuated the contrast. Another reason is the residual fluctuation between the common motion of end mirrors fed back by the feedback signal for the magnet-coil path of the absolute control system (detailed later).

The expected intensity noise of the Argon ion laser was about $10^{-3} \sim 10^{-4}$ for frequency below 10Hz, which needed to be suppressed by more than 140dB under 1 Hz to achieve the

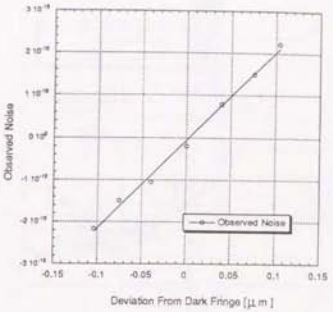

Figure 5.22: The relation between the deviation from the darkfringe and the correspondent output noise in the sensitivity

targeted sensitivity of 2×10^{-16} m/$\sqrt{\ }$ Hz as detailed in Chapter 4. Figure 5.23 shows the sensitivity of TENKO-100 and the intensity noise involving the calibration signal at 1 kHz whose peak was matched to the corresponding peak of 1kHz in the sensitivity curve. It showed that more open loop gain or the intensity noise stabilization were necessary because the intensity noise level was barely below the present sensitivity level 1.1×10^{-15} m/$\sqrt{\ }$ Hz.

Intensity Stabilization by the AOM

Figure 5.24 shows the intensity stabilization system with the Acoustic Optical Modulator (AOM). The AOM had the ability to distribute one input laser beam into n-th order angular directions in power by Bragg Reflection. The process involved a stationary refraction pattern standing in a crystal caused by an inertial elastic stresses applied by a PZT modulated at a high frequency, where 80 MHz~100 MHz was usually used. The power of the 0th order beam which passed straightly through AOM's crystal was adjusted by distributing the power into higher order beams through the modulation power control.

The intensity of the laser beam illuminating the interferometer, *i.e.* transmitting beam

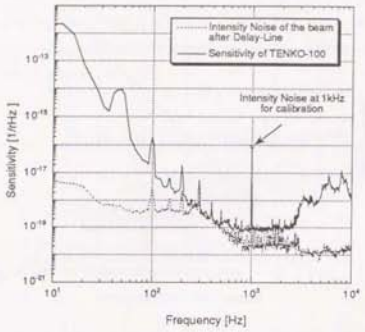

Figure 5.23: The intensity noise in the sensitivity of TENKO-100

of the AOM, was stabilized by using a sampled portion of the beam reflected on the AR coating surface of the beam splitter as an error intensity signal, not by itself. Figure 5.25 and Figure 5.26 shows the block diagram and the bode diagram of the intensity stabilization system, respectively. The unity gain frequency was set around 10 kHz, which was 1/10 times as small as the corner frequency of the AOM power controller response, in order to obtain enough phase margin there. The locked laser power was decreased by 10% $\sim$ 20% of the maximum transmitted light power to obtain enough dynamic range and a linear frequency response of the AOM. The measured open loop gain denoted by a dotted curve and the unity gain frequency were in good agreement with the theoretical one (denoted by a thick solid curve). Figure 5.27 shows the intensity noise of the original laser beam, the stabilized sampled portion and the beam after Delay-Line traversal. To eliminate the contribution of the scattered light noise as much as possible, the absolute control (detailed later) was operated during the measurement. Although the sampled beam was well-stabilized to the shot noise level of about 10^{-7}, the beam after the Delay-Line traversal was not as good as the input beam. The scattered light superimposed on the sampled light and the scattered light from the Delay-Line might decrease the stabilization efficiency, however the reason

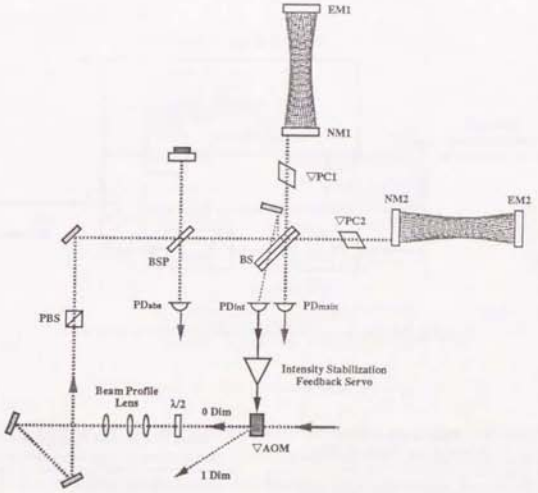

Figure 5.24: The setup for the intensity stabilization

for this point was not yet known precisely.

5.3.4 Beam Jitter Noise

Noise Characteristics in a Delay-Line Interferometer

The contribution of the geometrical fluctuation of the illuminated injection beam caused by the internal intensity fluctuation due to the additional higher transverse modes of the TEM_{00} mode and due to the vibration of non-isolated mirrors, can be canceled with the symmetrical interferometer setup. However, much of it couples to the imperfect symmetry of the interferometer and optical isolation, and produces "beam jitter noise".

The behavior of the beam jitter noise in a Delay-Line interferometers is expected to be

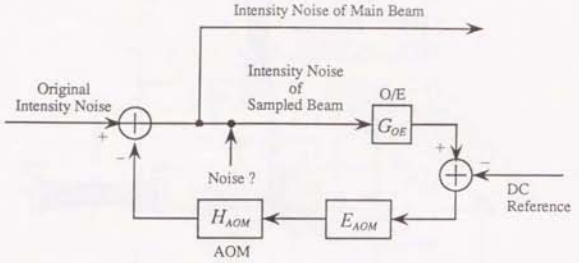

Figure 5.25: The block diagram for the intensity stabilization

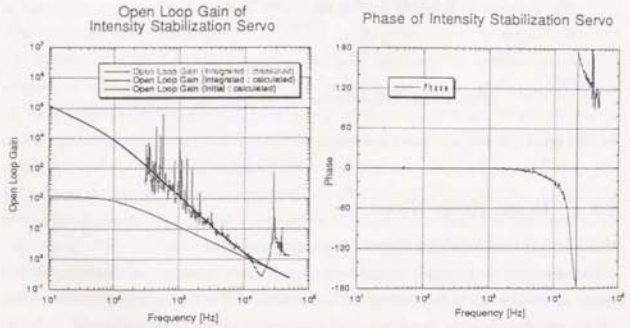

Figure 5.26: The bode diagram for the intensity stabilization

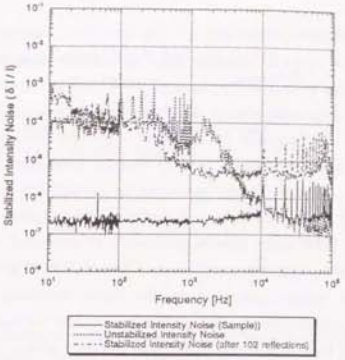

Figure 5.27: The stabilized intensity noise

nearly the same as that of a simple Michelson interferometer because the re-entrance beam of the Delay-Line can be regarded as the beam reflected from the back of near mirror's surface in a Michelson interferometer. On the other hand, the contribution of the beam jitter noise due to the Delay-Line traversal is proved to be negligible from the theoretical calculation [49].

If the beam splitter has an angular deviation, $\delta\theta_{BS}$, in rotation from the symmetrical position and the injection beam has transverse fluctuation, $\delta x_{\rm in}$, then, their coupling produces noise the following [50]

$$\Delta L_{BJ} = 4\delta\theta_{BS}\delta x_{in} \quad \left[\mathrm{m}/\sqrt{\mathrm{Hz}}\right] \quad . \tag{5.17}$$

In the case of TENKO-100, the expected geometrical fluctuation of the injection beam was 10^{-11} m/$\sqrt{\ }$ Hz around 100 Hz and the rotational one was 10^{-5} rad. This would bring a comparable displacement fluctuation, 4×10^{-16} m/$\sqrt{\ }$ Hz at 100 Hz in the sensitivity.

Mode Cleaning

The expected beam jitter noise level in TENKO-100 might be negligible at present, but

it should be suppressed in the future km-class interferometers. One method for suppressing the beam jitter noise is an optical glass fiber [47] which has a Gaussian intensity distribution and passes only TEM_{00} mode. The output structure of the fiber located in vacuum should be isolated by some suspension system. However, there are two distinct disadvantages : one is the loss of the input power at the input port of the fiber and the other is the power limitation. Loss is typically about 10 % to 50 % of the maximum laser power below 1 W. These limitations were totally quite insufficient for TENKO-100. Another method is a mode cleaner [52, 48] which works as a mode selector and a frequency stabilizer. A mode cleaner has a Fabry-Perot cavity consists of a couple of suspended mirrors facing with each other, and their separation is controlled by a proper servo to keep only the TEM_{00} on resonance and to prevent degeneracy from other higher transverse modes. Thus, only TEM_{00} beam is transmitted into this cavity , and it is used for the injection beam for the interferometer. Since there was an improvement of efficiency of over 40dB reported with such mode cleaner, it will be the most reliable instrument for the future usage.

5.3.5 Scattered Light Noise

Noise Characteristics in a Delay-Line Interferometer

Scattered Light Generation

Imperfections in the mirror's surfaces scatter a small amount of the beam away from the expected reflection paths. This kind of scattered light produces noise by interfering with the incident beam at the photo-detector after traveling completely different paths, which are difficult to be diagnosed in many possible ways.

However, in Delay-Line laser interferometers, another kind of scattered light [53] produces malignant characteristic noise more dominant than any other noise. This is mainly because of the existence of a re-entrance hole in the near mirror. For example, a small amount of the beam located on the edge of the Gaussian beam due to the fraction fails to exit through the entrance hole, and traces back the same path. It eventually re-enters the hole after making one more or many complete Delay-Line trips. This type of scattered light interferes with the main beam every characteristic periodical time interval corresponding to the Delay-Line trip. Such large phase shift of the scattered light proved to produce frequency up-conversion

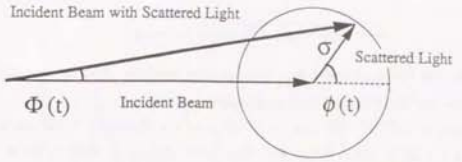

Figure 5.28: The phase of the main beam with the scattered light

noise.

Other type of the scattered light characteristic in Delay-Line comes from overlapped area of neighboring spots. Such scattered light may take the same path as the neighboring beam should take due to the roughness of the coating surface and dust. Then, such optical length cuts length by four times arm length due to the Delay-Line rule (refer to Chapter 4). In TENKO-100, the scattered light from the overlapped area may be negligible because the overlapped area did not exist in the given beam profile, but a part of the diffraction of the beam may contribute.

Scattered Light Noise

According to the vector summation of the phase of the main beam ($\Phi(t)$), and the phase of interfered scattered light whose relative power ratio and phase are given by, σ^2 and $\phi(t)$, respectively, as shown in Figure 5.28 [53], we can derive the following equation:

$$[1 + \sigma\cos\phi(t)]\tan\Phi(t) = \sigma\sin\phi(t) \rightarrow \Phi(t) = \sigma\sin\phi(t) \quad , \tag{5.18}$$

in the approximation of $\sigma \ll 1$.

On the other hand, $\phi(t)$ is given by

$$\phi(t) = 2\pi\frac{\nu(t)\,L(t)}{c} \quad . \tag{5.19}$$

$\nu(t) = \nu_0 + \delta\nu$ Frequency of a laser which fluctuates by $\delta\nu$ around ν_0
$L(t) = L_0 + \delta L$ Relative path difference which fluctuates by δL around L_0

From Eq 5.18 and Eq 5.19, we obtain

$$\Delta\Phi(t) = \sigma\left(\frac{\delta\nu}{\nu_0} + \frac{\delta L}{L_0}\right)\phi_0 \cos\phi_0 \quad . \tag{5.20}$$

This shows that the scattered light noise has two separate contributions, one is the frequency noise and the other is the seismic noise.

In the case of TENKO-100, the contribution of the frequency noise was estimated to be about 1.8×10^{-16} m/$\sqrt{}$ Hz at 100 Hz, assuming that $\sigma = 10^{-4}$, $\delta\nu = 10^{-1}$ Hz/$\sqrt{}$ Hz and $L_0 = 10^4$ m. This was just comparable with the sensitivity goal of TENKO-100 and indicated that the frequency stabilization was indispensable even with a symmetrical interferometer setup. The other contribution involved worse severe noise generation in the Delay-Line interferometer.

Up-Conversion Noise

The straightforward contribution of the seismic noise in Eq 5.20 was estimated to be below 3.6×10^{-16} m/$\sqrt{}$ Hz for the frequency range less than 100 Hz, with the assumption of $\sigma = 10^{-4}$, the seismic noise in low frequencies $\sim 10^{-7}$ m/$\sqrt{}$ Hz and $L_0 = 10^4$ km, because of the high seismic noise isolation efficiency by the combination of the pendulum and the stack. However, Figure 5.28 and Eq 5.20 show that the non-linearity of the scattered light noise transformation with $\delta\Phi(t) \propto \cos(\nu(t))$. Supposing that the mirror displacement at 1 Hz is comparable to the laser wave length (λ or 2π in phase) caused by the seismic noise, it is multiplied by the number of reflections of the Delay-Line. Therefore, the relative phase difference of the scattered light is $N \times 2\pi$, which means that the noise was converted up to N Hz. Such an up-conversion noise is large enough and just in the observational frequency band to decrease the sensitivity seriously. The expected up-converted frequencies are given by

$$f_{up} = 2 f_0 N \frac{dx_m}{\lambda} \quad . \tag{5.21}$$

λ : Wave length of a laser
f_0 : Original frequency
dx_m : Displacement of a mirror

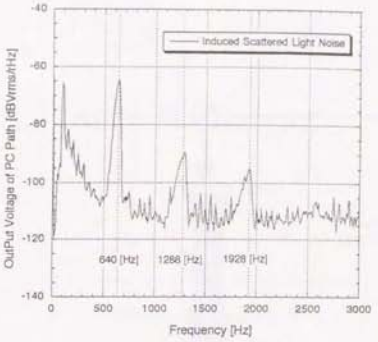

Figure 5.29: The induced up-conversion noise

In the case of an interferometer, the displacement fluctuation in the low frequency range is mainly dominated by the seismic noise (Eq 5.2), the expected up-converted frequency is given by

$$f_{up} = 7.7 \times 10\left(\frac{1}{f_0}\right) \quad (0.1\text{Hz} < f < 0.625\text{Hz}) \quad . \tag{5.22}$$

For TENKO-100, the up-conversion noise over 1 kHz was expected to be observable. Specifically, the round trip scattered light was even more dominant in the Delay-Line laser interferometers than other non-stationary scattered light. The periodical characteristic could be observed as up-converted frequencies as shown in Figure 5.29 which was obtained by swinging the end mirror at 1 Hz. (see in Figure 5.30). The first largest peak corresponded to the traversal of one more Delay-Line and second and third large peaks correspond to the complete traversal of the Delay-Line path by two and three more times. Figure 5.31 shows the relation between the mirror displacement and frequency of the up-converted scattered light noise. They were in good agreement with the theoretical calculation from Eq 5.21 both in the up-converted frequency and the linearity for the mirror displacement.

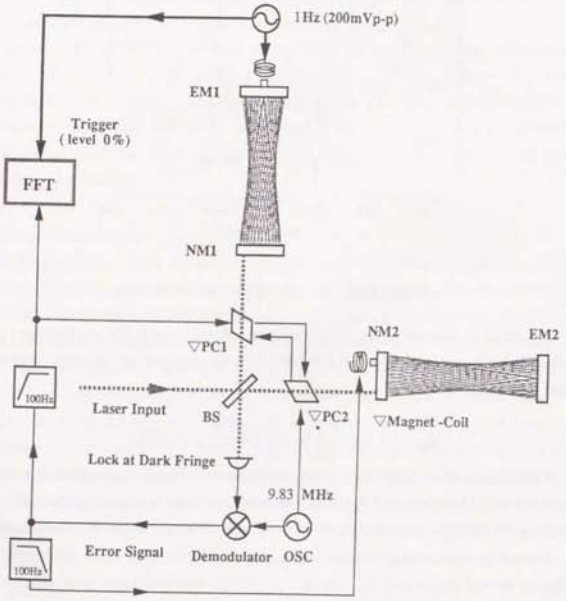

Figure 5.30: The experimental setup for the up-conversion noise measurement

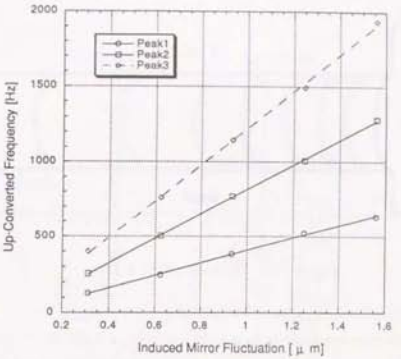

Figure 5.31: Relation between the mirror displacement and the up-converted frequency of the scattered light noise

Scattered Light Noise in km-class Interferometer

The scattered light came not only from on the main mirrors, but also from other optics, such as, Pockels cells, PBS, and a beam sampler. The scattered light was produced by impurities in the optics. Even in TENKO-100, the scattered light illuminated the all main mirrors and filled the whole of the ducts. In the future km-class interferometer, slowly sweeping scattered light reflected from the surface of large ducts which are perturbed by wind or inertial oscillation waves across the surface will be a significant noise source.

Passive Noise Reduction

It is important to reduce the amount of the scattered light passively. Firstly, we provided the same spot size of the beams on the mirrors to reduce the overlapped area by the beam profile of the injection beam as well as controlling the resolution of the beam spot distortion. Secondly, a black entrance hole adapter was used to let in and out the beam and prevented the diffraction of neighboring spots near the edge of entrance hole. Thirdly, the displacement fluctuation in the low frequency range was decreased to suppress the maximum up-converted frequency by the bottom plate suspension. This also improved the

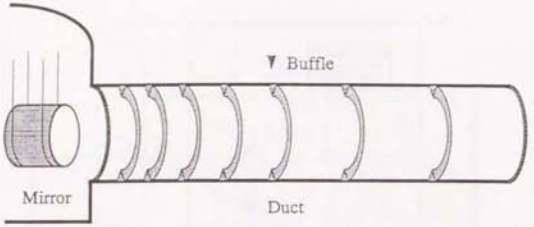

Figure 5.32: The baffles with a duct

poor seismic noise environment around TENKO-100.

For the full scale interferometer such as LIGO project, a baffle structure in the ducts (Figure 5.32) [54] was proposed. Baffles are a set of thin ring plates located on the internal surface of ducts according to the predetermined separation from the theoretical calculation, and they cause scattered light to reflect between them many times. Hence, the scattered light decreases drastically in power to acceptable levels for the targeted sensitivity. It was also proposed to apply the baffle structure in TENKO-100 in future.

Absolute Control System

Up-conversion can be prevented if the displacement fluctuation of the total optical path length in the low frequency range due to the seismic noise can be suppressed below the laser wavelength. In this case, the equivalent relative phase of the scattered light is deduced to below 2π. To stabilize it to the level of $1/N$ (reflection number) of the original fluctuation, we fix the absolute numbers of the laser waves counted in the Delay-Line whose wave length or frequency is quite stabilized with the isolated rigid Fabry-Perot cavity, by locking the interfered fringe between the beam before and after Delay-Line trip at dark fringe. This is called as an Absolute Control system [51]. The bright fringe beam obtained at the other output port of the interferometer after the darkfringe locking operation is used for the beam traveling the Delay-Line. The phase modulation method is also used to detect the fluctuation of the Delay-Line optical path length. In the case of TENKO-100 with optical path length of 10^4 m, the frequency stability below 100 Hz/$\sqrt{}$ Hz was required for the

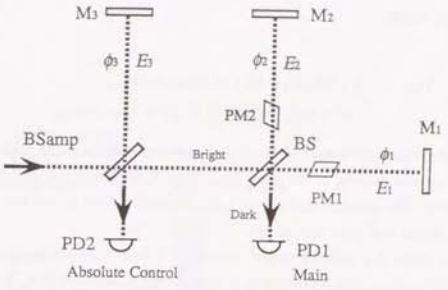

Figure 5.33: The absolute control setup

reference usage to suppress the displacement fluctuation of the total optical path length caused by the frequency noise to less than $\lambda/100$.

For example, we consider the absolute control of a simple Michelson interferometer as shown in Figure 5.33. The fringe at port PD1 is locked at the dark fringe for the main interferometer operation and the fringe at port PD3 is also locked at the dark fringe for the absolute control. Assuming that the phase delay of each traveling beam from injection are ϕ_1, ϕ_2, ϕ_3, the amplitude of the electrical field of the laser in each arm are $E_1 = E_2$ and E_3, the laser is modulated in phase inversely with $m/2$ modulation index at both Pockels cells, the electrical field at PD3 is given by

$$E_{PD3} = \frac{E_0}{2} e^{-i\left(\phi_1 + \frac{m}{2}\sin\omega_{\rm mod}t\right)} + \frac{E_0}{2} e^{-i\left(\phi_1 - \frac{m}{2}\sin\omega_{\rm mod}t\right)} - E_3 e^{-i\phi_3} \quad , \tag{5.23}$$

where $\phi_1 = \phi_2$ and $\phi_1 + \phi_2 = 2\phi_3$ mean the dark fringe at the PD1 and the PD3 port, respectively. Then, the photo-current at the PD3 is given by

$$\begin{aligned} I_{PD3} \;\propto\; & 2 + k^2 + 2\cos\left(\phi_2 - \phi_1 - m\sin\omega_{\rm mod}t\right) \\ & -2\cos\left(\phi_1 - \phi_3 + \frac{m}{2}\sin\omega_{\rm mod}t\right) - 2\cos\left(\phi_2 - \phi_3 - \frac{m}{2}\sin\omega_{\rm mod}t\right) \quad , \end{aligned} \tag{5.24}$$

where $k = 2E_3/E_0$. Eq 5.24 can be transformed by replacing, $\phi_1 - \phi_2 = d\phi_{dark}$, $\phi_1 + \phi_2 - 2\phi_3 = d\phi_{abs}$ as follows

$$I_{PD3} \propto 2 + 2J_0(m) - 4J_1(m)\,\Delta\phi_{dark}\sin\omega_{mod}t + k^2 - 4kJ_0(m/2) - 4kJ_1(m/2)\,\Delta\phi_{abs}\sin\omega_{mod}t \quad . \tag{5.25}$$

Only the first order contribution of the Bessel function is taken. The first row can be regarded as the contribution of the main dark fringe locking and the second one as the absolute control. The effective modulation index becomes half of m and the value of the displacement signal is in proportional to k.

Figure 5.34 shows the absolute control system for TENKO-100. The input beam was sampled with a beam sampler suspended by a double pendulum in front of the beam splitter. It was reflected back at the suspended mirror with the Slow PZT on its back, while the recombined beam locked at bright fringe by the beam splitter was "re-recombined" with it at the beam sampler and the "re-recombined" beam is locked at the dark fringe. Thus, the total optical path length could be stabilized to the displacement of the mirror with the Slow PZT if the frequency was stabilized below the equivalent level.

Figure 5.35 and Figure 5.36 show the block diagram and the bode diagram (calculated and measured) for the absolute control system, respectively. The servo had two loops to the Slow PZT and the both end mirrors. The higher frequency part of the demodulated signal was fed back to the Slow PZT which had a mechanical resonance at 2.7 kHz which limited the unity gain frequency. The lower part of the demodulated signal was fed back to the two inputs of the local control for the both end mirrors to use the common mode efficiency. The cross over frequency was set around 20 Hz and the unity gain frequency was set around 1 kHz. Moreover, the feedback signal to the mirrors over 100 Hz was filtered by a 8 pole low-pass steeply not to "kill" the signal of gravitational waves by this feedback servo. The measured open loop gain was in good agreement with the theoretical design. Appendix F shows the feedback servo circuit. A gain integration circuit at 10 Hz was installed to obtain a stable locking in low frequency. Because of the low frequency resonance of the PZT and the wire of the main mirror suspension, the feedback signal involved a slight oscillation after the absolute control locking.

Figure 5.37 shows the effect of the absolute control on sensitivity. It could be drastically

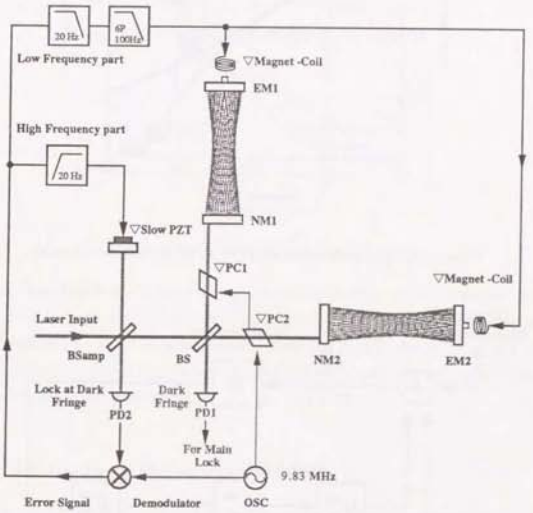

Figure 5.34: The absolute control setup for TENKO-100

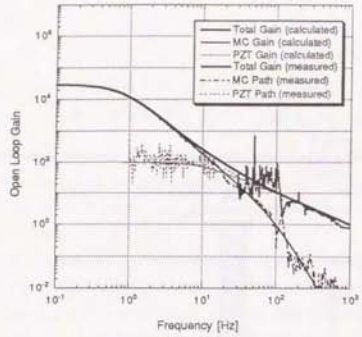

Figure 5.35: The feedback block diagram for the absolute control

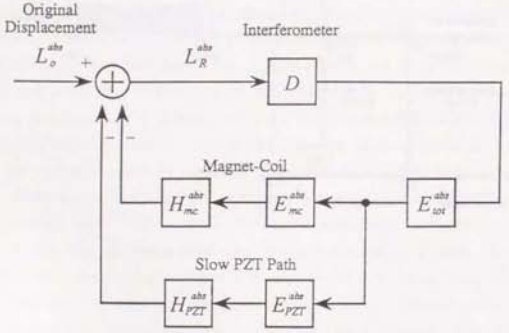

Figure 5.36: The feedback bode diagram for the absolute control

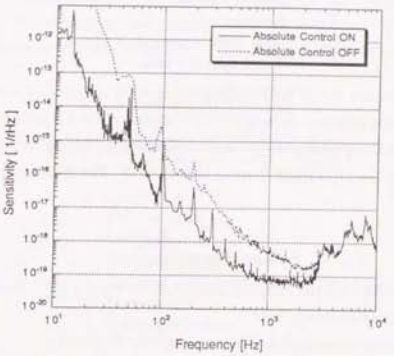

Figure 5.37: The effect of the absolute control

improved less than 3 kHz through the absolute control. This was the first time that the effect of the absolute control has been demonstrated in such a large scale interferometer. There might exist a residual up-converted scattered light noise due to the several Delay-Line trips (over several 10 km) because of the insufficient open loop gain in low frequency and insufficient isolation of the mirror with the Slow PZT.

5.4 Radiation Pressure Noise

The change of the momentum of photons due to striking mirrors results to apply a force to the mirrors. The photon number fluctuation from the quantum nature of photons leads to perturbation in the position of the mirrors, which is called as radiation pressure noise.

The optical path fluctuation caused by the radiation pressure in a simple Michelson interferometer is given by

$$\Delta L_{rad} = \frac{1}{Mf^2}\sqrt{\frac{hP_{circ}}{2\pi^3 c\lambda}} \quad . \tag{5.26}$$

M : Mass of a mirror
f : Frequency
P_{cic} : Laser power hitting on a mirror
λ : Wavelength of a laser

where the loss of power due to the reflection is neglected. In the case of the Delay-Line interferometer with a reflection number of N, the amount of force is multiplied by N. The amount of the displacement fluctuation is also multiplied by $2N$, so totally scaled up by $2N^2$. On the other hand, the signal is also scaled up by N. The radiation pressure noise is given by

$$\Delta L_{rad,DL} = \frac{N}{Mf^2}\sqrt{\frac{2\hbar P_{in}}{\pi^3 c\lambda}} \quad . \tag{5.27}$$

In the case of TENKO-100, the radiation pressure noise was $5 \times 10^{-23}\ 1/\sqrt{\text{Hz}}$, which was far below the targeted sensitivity level.

Since the shot noise determined by the same condition is given by

$$\Delta L_{shot} = \frac{1}{N}\sqrt{\frac{\hbar c\lambda}{2\pi P_{in}}} \quad , \tag{5.28}$$

the cross over frequency where the radiation pressure noise overtakes the shot noise is given by

$$P_{cross} = \frac{\pi c\lambda M f^2}{2N^2} \quad . \tag{5.29}$$

In the case of TENKO-100, this cross over frequency was 0.5 Hz which was well below the observational band assuming M = 17 kg, N=102, P_{in} =1W. Even in the case of a km-class interferometer, the 70 Hz for P_{in} = 1 kW .

5.5 Thermal Noise

If an instrument is soaked in thermal volume, its internal resonance vibration is excited by thermal brownian motion. All of them, the thermal noise from a pendulum and a mirror gives a severe limitation for the sensitivity. The motion equation [55] is given by

$$M_r\frac{d^2x}{dt^2} + \gamma\frac{dx}{dt} + kx = f_T(t) \quad , \tag{5.30}$$

where M_r is the reduced mass of a mode and $f_T(t)$ is the fluctuating force due to the thermal noise. The equivalent elastic constant has imaginary part [56], which means it depends on frequency. The spectrum of the harmonics mode is given by

$$\left\langle f_T(\omega)^2 \right\rangle = \frac{4M_r\omega_0^2\phi(\omega)k_BT}{\omega} \quad , \tag{5.31}$$

$$\left\langle x(\omega)^2 \right\rangle = \frac{4k_BT}{\omega}\frac{\omega_0^2\phi(\omega)}{M_r\left|-\omega^2+\omega_0^2(1+i\phi(\omega))\right|^2} \quad . \tag{5.32}$$

x : Coordinate
M_r : Reduced mass
$\phi(\omega)$: Complex elastic constant
ω : Vibration angular frequency
ω_0 : Resonant angular frequency of the mode
T : Temperature
k_B : Boltzman constant

The thermal noise of a pendulum is given by [57]

$$\sqrt{\left\langle x(\omega)^2 \right\rangle} \approx 8.2\times10^{-21}\left(\frac{M_r}{10kg}\right)^{-\frac{1}{2}}\left(\frac{f_p}{1Hz}\right)^{\frac{1}{2}}\left(\frac{10^5}{Q}\right)^{\frac{1}{2}}\left(\frac{f}{1kHz}\right)^{-2} \quad \left[\text{m}/\sqrt{\text{Hz}}\right] \quad . \tag{5.33}$$

The thermal noise of a mirror is given by [55]

$$\sqrt{\left\langle x(\omega)^2 \right\rangle} \approx 7.0\times10^{-20}\left(\frac{M_r/2}{10kg}\right)^{-\frac{1}{2}}\left(\frac{3.5kHz}{f_0}\right)\left(\frac{\phi}{10^{-5}}\right)\left(\frac{f}{1kHz}\right)^{-\frac{1}{2}} \quad \left[\text{m}/\sqrt{\text{Hz}}\right] \quad . \tag{5.34}$$

They indicate that the mirrors should have low internal resonant mode and high mechanical Q value.

In the case of TENKO-100, mirrors made of fused silica have mass of 17 kg and their Q value was $10^4 \sim 10^5$, the internal first resonant frequency was 3.5×10^3Hz, young modulus was 7.03×10^{10} N/m^2, mass density was 2.2×10^3 kg/m^3, and they had 35 cm diameter and 8.2 cm thickness. The thermal noise of a pendulum was estimated to be 5.1×10^{-19} m/$\sqrt{}$ Hz at 1 kHz and 5.1×10^{-17} m/$\sqrt{}$ Hz at 100 Hz due to the contribution of the 102 times reflections, which were well below the targeted sensitivity. The thermal noise of a mirror was also estimated to be 8.5×10^{-18} m/$\sqrt{}$ Hz. If the mechanical Q value was

Molecule	Reflection Index n_0	Mean Speed [m/s]	Required Pressure 10^{-1} [Torr]
H_2O	1.000252	435	0.9
N_2	1.000297	349	0.5
H_2	1.000138	1310	9

Table 5.3: Required pressure for typical outgas

decreased below the expected values because of the direct attachments, *i.e.* magnets and wire standoffs, it might be enhanced, however, this was hardly the case presently.

5.6 Residual Gas Noise

Although the refractive index fluctuations due to the air density and the acoustic noise from the environment produce the phase fluctuation of the optical path, these undesirable contribution can be suppressed easily below the goal sensitivity in such a Delay-Line interferometer as TENKO-100. On the contrary, quite severe pressure level below 10^{-8} Torr will be required for the km-class interferometer because the required pressure level [57, 58] is given by

$$\sqrt{\langle x^2 \rangle} = \sqrt{16\sqrt{\frac{2}{\pi}}\frac{(n_0-1)^2}{(A_0/V_0)\,u_0\sqrt{\ell\lambda}}\left(\frac{P}{P_0}\right)\left(\frac{T}{T_0}\right)^{3/2}} \quad \left[\mathrm{m}/\sqrt{\mathrm{Hz}}\right] \quad . \tag{5.35}$$

- ℓ : Arm length
- n_0 : Refraction index of standard state
- V_0 : Volume occupied with 1mol gas molecules at standard state
- A_0 : Abogadro index (6×10^{23})
- u_0 : Mean velocity of gas molecule at standard state
- λ : Wave length of laser
- P : Pressure
- T : Temperature

This shows the equivalent sensitivity is proportional to the square root of pressure. Table 5.3 shows the required pressure level for the representative outgas, H_2O, N_2 and H_2. In the case of TENKO-100, the required pressure was estimated to be 10^{-3} Torr which was well within the vacuum ability for 15,000 ℓ of TENKO-100. The amount of the outgas of one arm whose internal surface area reached $1.25 \times 10^6 \mathrm{cm}^2$ was measured to be 4.16×10^{-10} Torr $\ell\ \mathrm{s}^{-1}\ \mathrm{cm}^2$, which meant 6 hour continuous operation under 10^{-3} Torr was feasible.

Chapter 6

Spectral Sensitivity of TENKO-100

6.1 Experimental Apparatus and Conditions

As a result of the various noise reduction systems, the spectral strain sensitivity of TENKO-100 as shown in Fig 6.1 was obtained with the experimental setup shown in Figure 6.2 under the conditions shown in Table 6.1.

The main beam (970 mW) emitted from the laser passed through a Faraday isolator to prevent any part of the beam from returning to the laser. A portion of the main beam ($\sim$ 10 mW) was reflected on a beam sampler and was led to the frequency stabilization system. The remainder of the main beam passed through the AOM for the intensity stabilization and about 20% of the power was diffracted with it to obtain enough dynamic range for the intensity stabilization system. After beam profile with a set of three flat-convex lenses to match curvatures between the mirror and the beam's wave front, the beam (610 mW) was adjusted for the angle, the vertical, and the translational position of the input beam by two crank mirrors and fed into the interferometer.

The beam entered into the central vacuum chamber and passed through a PBS to match its linear polarization to the beam splitter, and a portion was reflected by the suspended beam sample mirror of the absolute control system. The beam splitter divided the beam in half power and illuminated both arms of the interferometer. In each arm, the beam passed through a Pockels cell where the beam was modulated in phase by 9.83 MHz signal and then formed the Delay-Line path after passing entrance holes. A portion reflected on the AR coating of the beam splitter was detected as a reference signal of the beam intensity.

After traveling the Delay-Line path of 10 km, the beams were recombined at the beam

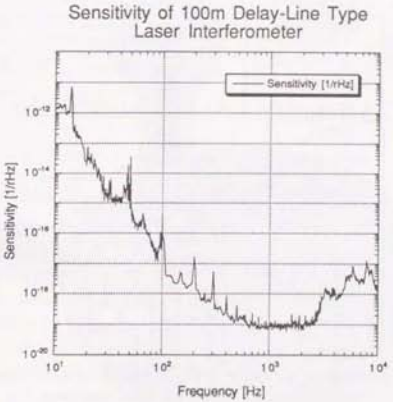

Figure 6.1: The sensitivity of the 100m Delay-Line Laser Interferometer at ISAS

splitter and one port was locked at the dark fringe with the main feedback servo. According to the characteristic of the beam splitter, the recombined beam was locked at bright fringe in one port if it was locked at the dark fringe in the other port.

In addition to the dark fringe locking operation, the beam recombined to the bright fringe was recombined with the input sampled beam reflected by the suspended mirror with the Slow PZT at the beam sampler. This was also locked at the dark fringe with the absolute control feedback servo system.

The TENKO-100 was operated in the midnight from 1 AM to 4 AM to minimize the disturbance due to a nearby car traffic. Moreover, all pumps except cryo and turbo pumps in both mid rooms, and air conditioners of all rooms, which produced the troublesome 48 Hz noise, were turned off.

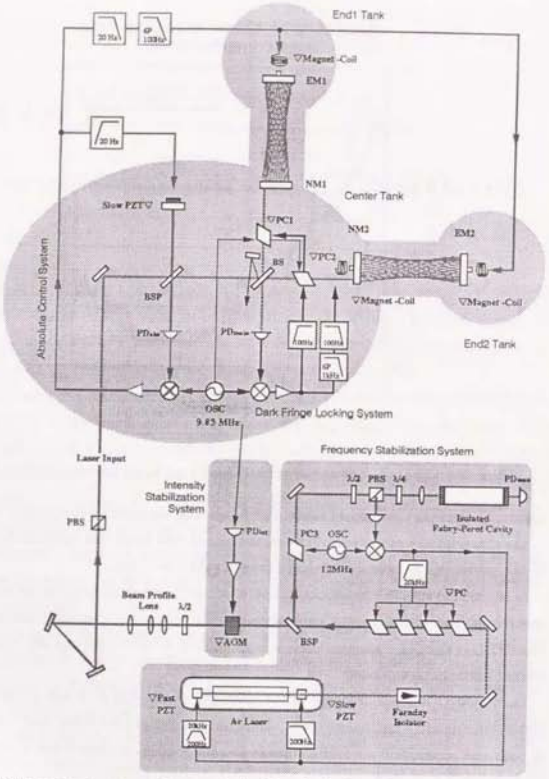

Figure 6.2: The control system and setup of the 100m Delay-Line Laser Interferometer for the sensitivity measurement

Factors	Conditions	Optical Stabilization	Status
Incident Laser Power	140 [mW]	Frequency Stabilization	○
Modulation Index	0.2 [rad]	Intensity Stabilization	○
Contrast	98 [%]	Phase Modulation	○
Total Optical Path Length	102 × 100.5 [m]	Absolute Control	○

Table 6.1: Sensitivity measurement conditions

6.2 Possible Noise Element in the Attained Best Sensitivity

In this section, possible noise sources dominant in the sensitivity are discussed for each frequency range. Almost all dominant noise sources were identified except for the range from 40 Hz to 200 Hz.

6.2.1 Seismic Noise (≤40 Hz)

Fig 6.3 shows that the isolated seismic noise was dominant for the frequency range less than 40 Hz. It reveals that the seismic noise was isolated as we expected from the individual isolation performance of the single pendulum, the bottom plate suspension and the stack. In this range, a satisfactory sensitivity level has been attained.

6.2.2 Unknown Noise (40 Hz∼200 Hz)

Noise source dominant in this frequency range of 40 Hz to 200 Hz have not been accurately identified yet. One possible source is non-stationary scattered light noise, but it was not verified yet.

6.2.3 Intensity Noise (200 Hz∼800 Hz)

Figure 6.4 shows that the measured intensity noise might be dominant from 200 Hz to 800 Hz because of insufficient intensity noise stabilization and the fluctuation of the dark fringe. One of reasons for this was that the spectrum of the beam after the Delay-Line traversal was still dominated by the scattered light noise with an optical path difference

more than several 10 km. Another reason was that the photo-detector for the dark fringe locking and/or for the intensity stabilization suffered from scattered light.

6.2.4 Shot Noise and Other Sources of Noise (800 Hz~2.5 kHz)

While the calculated shot noise level was 6×10^{-21} $1/\sqrt{\text{Hz}}$ with a contrast (K) of 98%, incident power ($P_{\max}$) of 140 mW and the modulation index (m) of 0.2, obtained floor level from 800 Hz to 2.5 kHz was around 1.0×10^{-19} $1/\sqrt{\text{Hz}}$ and it couldn't be improved even when the incident laser power was increased. In addition, the floor level often stimulated up to 5.0×10^{-19} $1/\sqrt{\text{Hz}}$. One of possible reason was that the intensity noise was close to it as shown in Figure 6.5. Theoretically, the intensity noise should have been suppressed with enough open loop gain of the main feedback servo around the low frequency range. However, the contrast was quite sensitive to the rolling motion of the mirrors that it might produce a large coupled noise with the intensity noise. Another reason was that the practical frequency noise was close to it. The third reason was the scattered light noise coupled to the frequency noise detailed in Chapter 5. The contribution for this could be estimated around 1.8 to 0.18 $\times 10^{-19}$ $1/\sqrt{\text{Hz}}$ from the relative intensity of the scattered light $\sigma = 10^{-4}$ and the practical frequency noise. The fourth was the non-stationary scattered light noise which was afraid to provide the flat noise spectrum from 4 to 0.4 $\times 10^{-19}$ $1/\sqrt{\text{Hz}}$ from the theoretical prediction because of separate beam paths of the Delay-Line path and the inferior location of TENKO-100.

6.2.5 Frequency Noise (2.5 kHz~10 kHz)

Fig 6.6 shows that the frequency range above 2.5 kHz was dominated by the frequency noise insufficiently stabilized with the two PZT paths. I have already established the frequency stabilization system with an additional feedback path, *i.e.* pockels cell path, and have stabilized it around 0.2 Hz/$\sqrt{\text{Hz}}$ under 10 kHz. Hence, it would be quite reliable to decrease the contribution of the frequency noise for the frequency range above 3 kHz. In future, we should use a mode cleaner system which not only reduces the beam jitter noise but also provides a more stable reference cavity than the rigid type in this high frequency range.

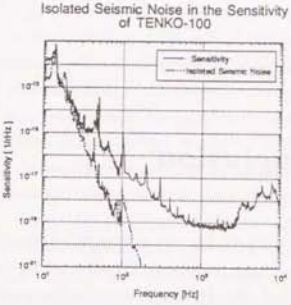

Figure 6.3: The seismic noise in the sensitivity of TENKO-100

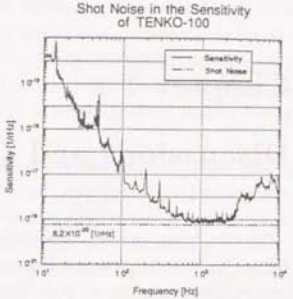

Figure 6.5: The shot noise in the sensitivity of TENKO-100

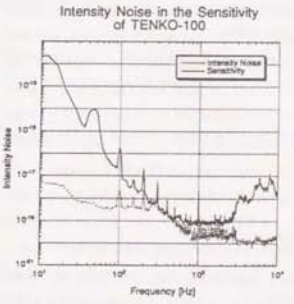

Figure 6.4: The intensity noise in the sensitivity of TENKO-100

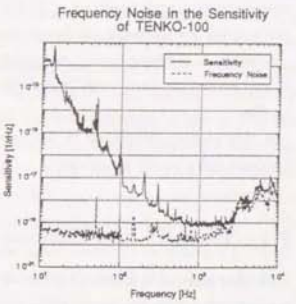

Figure 6.6: The frequency noise in the sensitivity of TENKO-100

Chapter 7

Discussions and Conclusion

The 100m Delay-Line laser interferometer, TENKO-100, has been constructed. TENKO-100 has the longest optical path length (10km) in the world with 102 times reflections between mirrors separated by 100 m. The principal control system as a pre-km-class gravitational wave detector has been established. Various noise characteristics of TENKO-100 were verified and corresponding noise reduction systems were also evaluated, while their strain sensitivity were improved to be $h = 1.1 \times 10^{-19}$ $1/\sqrt{\text{Hz}}$ around in the frequency range 800 Hz to 2.5 kHz with basic noise reduction systems. We also successfully demonstrated the long term operation of TENKO-100 for about ~100 hours to verify that the gravitational wave detector can be operated in this scale.

However, at the same time, it was proved that scattered light induced large noise in the Delay-Line interferometer and limited the sensitivity of TENKO-100 around 1.1×10^{-19} $1/\sqrt{\text{Hz}}$.

In this section, the results of this experiment are discussed focusing on the current problems and proposal for solutions.

7.1 Results and Discussions

The first attempt to fabricate mirrors with a large radius of curvature of 100m was nearly successful except the appearance of the beam spot distortion due to anisotropy of the mirror curvature. Although it left a problem for a km-class Delay-Line laser interferometer, the beam spot distortion and resulting fatal low contrast could be avoided with a proper choice

of the beam profile.

The 100m Delay-Line laser interferometer was operated as a gravitational wave detector for a long term operation with 100 hours. Continuous 2 hours operation of the frequency stabilization, continuous 3 hours operation of the intensity stabilization, and continuous 40 minutes operation of the absolute control and the dark fringe locking were verified. The break of operation of the absolute control and the dark fringe locking is mainly due to the violent disturbance by a nearby car traffic.

Noise performances, which limited the sensitivity of the detector, were verified for various noise sources such as the frequency noise, the intensity noise and the scattered light noise. They are proved to behave as theoretically expected. In addition, the basic noise reduction system for each noise sources were constructed and evaluated.

The frequency stabilization system was implemented with the Pound-Drever Method with three feedback paths adopting the Fast PZT, the Slow PZT and the outer Pockels Cells. Although the frequency noise can be reduced by CMRR, the matching of the optical path length was limited around 1m~2m due to miss-matching of each mirror curvature radius. The present stabilized frequency noise level was around 0.2 $\text{Hz}/\sqrt{\text{Hz}}$ and additional stabilization over 10dB was necessary for the targeted sensitivity, and more stabilized reference was necessary. The intensity stabilization system was realized by the AOM. The intensity noise for the frequency range around 1kHz was stabilized by 20 dB, while that for the frequency range less than 200Hz was not stabilized and the whole the intensity noise was not stabilized as the sampled beam. It was not verified precisely, however, the scattered light on the detector or the scattered light from the Delay-Line path might produce the intensity noise. The seismic noise isolation system was composed of a single pendulum and a stack. The seismic noise reduction with the stack was verified for the frequency range under 40 Hz in sensitivity. The absolute control system was implemented with the suspended mirror with the Slow PZT to reduce the scattered light noise by 20dB.

As a result of these noise reduction systems, the strain sensitivity reached $h = 8 \times 10^{-20}$ $1/\sqrt{\text{Hz}}$ and typically $h = 1.1 \times 10^{-19}$ $1/\sqrt{\text{Hz}}$ from 800 Hz to 2.5 kHz. The noise limit of the system was improved by 15 dB (35 dB) at 1 kHz, 40 dB (60 dB) at 500 Hz from 10m Delay-Line laser interferometer (TENKO-10) in addition to the scale factor 20dB (the number in the bracket represents total improvement). Any all of the noises listed above, the scattered light noise was the most obstructive problem and almost all effort was spent

for the scattered light noise reduction.

A new type absolute control system to reduce the scattered light noise was demonstrated and accomplished sufficient noise reduction ($\geq$20dB) in such a large scale interferometer as the 100m Delay-Line laser interferometer. In the existing absolute control system, a rigid Fabry-Perot cavity was used for the reference for the low frequency range, while for the high frequency range, the stabilization of the path length in the Delay-Line using isolated mirrors with a single pendulum and a stack system was used for the reference. High frequency part of the composed demodulated signal was fed back to an internal Pockels cell in a laser cavity and low frequency part was fed back to a Slow PZT attached with the front mirror of the laser cavity. Here, the absolute control was operated only by the feedback to both end mirrors. That was because the locking of the frequency stabilization and the absolute control should be operated simultaneously. We proposed a new type absolute control system because the internal Pockels cell can never be applied to the future high power laser and the dynamic range and frequency band width of the Fast PZT is insufficient for this scheme. If outer Pockels cells were used for the compensation for this, the feedback system becomes very complicated in addition to the composition of the demodulated signal. Hence, in this scheme, the low frequency part of the demodulated signal was fed back to the both end mirrors and the high frequency part was fed back to a Slow PZT attached with a mirror isolated by a single pendulum for usage of the sampled input beam reflection. With our scheme, we could reduce the contribution of the scattered light noise by ~20dB.

However, the up-conversion of the scattered light with the optical path difference over ~10 km against the main beam cannot be suppressed and the contribution of other scattered light which might reflect on the surface of ducts or might come from optical components could not be completely eliminated with this scheme. Actually, the sensitivity level from 800Hz to 2.5kHz could not be improved from 8×10^{-20} $1/\sqrt{\text{Hz}}$ with any stabilization system and this floor level was easy to stimulate up to 5×10^{-19} $1/\sqrt{\text{Hz}}$. This level was in accordance with the theoretically calculated scattered light noise level. In addition, the unknown noise for the frequency range from 40Hz to 200Hz might be the intensity noise caused by the interfering with scattered light. This revealed the disadvantage of the Delay-Line interferometer against the Fabry-Perot interferometer which has reached to the sensitivity level of 8×10^{-21} $1/\sqrt{\text{Hz}}$ at Caltech.

7.2 Present Problems and Possible Improvements

- Frequency Stabilization and Beam Jitter Noise

  Although the frequency stability for the frequency range less than 10 kHz reached around 0.2 Hz/$\sqrt{\text{Hz}}$ by the three paths feedback servo systems (the Slow PZT, the Fast PZT, and the Pockels cells), it was comparable with the targeted sensitivity level. In addition, the beam jitter noise was not stabilized at all at present system. These problems can be removed by a mode cleaner.

  In a linear mode cleaner, a Fabry-Perot cavity composed of two suspended mirrors provides a well-stabilized frequency reference. The transmitted beam from the cavity is tuned to the only TEM_{00} mode and used for the injection beam of interferometers. The reflected beam from the cavity is detected with a circulator set before the cavity and detected with a photo-detector. The low frequency part of the demodulated signal is fed back to the magnet-coil path of the cavity mirrors, middle range is fed back to the Slow PZT and the Fast PZT in a laser cavity, and high frequency part is fed back to the outer Pockels cells. We also tried to construct mode cleaner and succeeded in locking the beam at TEM_{00} mode. To obtain the sufficient frequency stability, the cross over frequency between the magnet-coil path and the PZT path should be as low as possible, however, it was limited around 10Hz at present and locking was not stable. Thus, more isolation such as double pendulum for the reference cavity mirror will be necessary.

  Recently, a ring cavity mode cleaner composed of three mirrors was proposed for the improvement of a linear mode cleaner. A ring mode cleaner can eliminate the contribution of the reflected beam from interferometers.

  In addition, the laser tube itself should also be mechanically isolated through a stack from the super-inver table which was fluctuated by the water flow of a cooling system.

- Intensity Stabilization for large loop

  Figure 6.4 shows that the intensity noise was originally comparable to our targeted sensitivity of $h = 2 \times 10^{-20}$ $1/\sqrt{\text{Hz}}$. The intensity stabilization system with the AOM revealed the two order of magnitude reduction ratio for the transmitting beam in the

head test, however it could not stabilized the intensity noise of the beam traveling the Delay-Line path so much if it was employed in the interferometer. This was not fully understood. One of reasons might be badly located photo-detector, and another might be the scattered light from the Delay-Line path.

- Local Control Circuit Noise

  If all optical noises are sufficiently reduced, the noise produced by the coupling force between the magnets on the mirrors and the local control circuit noise of 30 nV/$\sqrt{\text{Hz}}$ at present (due to integration of resistor Johnson noise) will become important for the frequency range less than 400 Hz. An application of weaker magnets and resistors with around 100Ω are the remedy for this.

- Baffles in Ducts

  In order to reduce the scattered light noise, baffles should be implemented. According to theoretical studies [54], the scattered light noise of a km-class Fabry-Perot interferometer can be reduced to 10^{-24} $1/\sqrt{\text{Hz}}$ level from 10^{-19} $1/\sqrt{\text{Hz}}$ using appropriate baffles.

7.3 Conclusions

In this experiment, the 10m Delay-Line interferometer (TENKO-10) has been upgraded to the 100m Delay-Line interferometer (TENKO-100) and the sensitivity of the TENKO-100 could be improved by more than scale factor of 20dB, from the sensitivity of TENKO-10. However, as a result of any effort to improve the sensitivity, the scattered light noise became obstructive for the improvement of the Delay-Line interferometer even in the scale of 100m arm length, and its sensitivity level was limited to around 1.1×10^{-19} [$1/\sqrt{\text{Hz}}$]. This was regarded as the disadvantage of a Delay-Line interferometer against a Fabry-Perot interferometer and would become a partial evidence for the determination of the type for km-class interferometers.

Appendix A

Composition and Decomposition of Position Signals of a Mirror

The pure motion signals of a mirror (P_{pos}, R_{pos}, X_{pos}, Y_{pos}) are composed from the position signals of A_{pos}, B_{pos}, C_{pos}, and D_{pos} as follows

$$\begin{pmatrix} P_{pos} \\ R_{pos} \\ X_{pos} \\ Y_{pos} \end{pmatrix} = \begin{pmatrix} k_1 & -1 & -k_2 & 0 \\ 0 & 1 & k_3 & 0 \\ k_4 & 1 & k_5 & 0 \\ 0 & 0 & 0 & 1 \end{pmatrix} \begin{pmatrix} A_{pos} \\ B_{pos} \\ C_{pos} \\ D_{pos} \end{pmatrix} .$$

where we suppose that the contribution of the A signal to the Pitch signal can be negligible with equilateral disposition of the magnets on the back of mirrors because of leverage.

The mode elimination efficiency can be increased by the method to adjust k factors as follows ,

1. k_3 factor Induce X motion with the resonant frequency of X mode (0.625 Hz) from X input. Adjust k_3 factor to minimize the contribution of X mode in R GC monitor.
2. k_2 factor Induce R motion with the resonant frequency of R mode (0.3 Hz) from R input. Adjust k_2 factor to minimize the contribution of R mode in P GC monitor.
3. k_1 factor Induce X motion with the resonant frequency of X mode (0.625 Hz) from X input. Adjust k_1 factor to minimize the contribution of X mode in P GC monitor.
4. k_5 factor Induce R motion with the resonant frequency of R mode (~0.3 Hz) from R input. Adjust k_5 factor to minimize the contribution of R mode in X GC monitor.

5. k_4 factor Induce P motion with the resonant frequency of P mode (~0.7 Hz) from P input. Adjust k_4 factor to minimize the contribution of P mode in X GC monitor.

Then, we obtained over 20dB mode elimination ratio.

After determination of k factors, t factors for de-composition from $P_{drv}, R_{drv}, X_{drv}, Y_{drv}$ feedback signals to the position driving signals, $A_{drv}, B_{drv}, C_{drv}, D_{drv}$ can be determined as follows

$$\begin{pmatrix} A_{drv} \\ B_{drv} \\ C_{drv} \\ D_{drv} \end{pmatrix} = \begin{pmatrix} t_1 & 0 & t_2 & 0 \\ -1 & t_3 & t_5 & 0 \\ -t_4 & -1 & 1 & 0 \\ 0 & 0 & 0 & 1 \end{pmatrix} \begin{pmatrix} P_{drv} \\ R_{drv} \\ X_{drv} \\ Y_{drv} \end{pmatrix}$$

In the same way, the mode elimination efficiency can be increased by the method to adjust t factors as follows,

1. t_5 factor Induce X motion with ~2 Hz signal from X input. Adjust t_5 factor to minimize the contribution of ~2 Hz in R GC monitor.

2. t_4 factor Induce P motion with ~2 Hz signal from P input. Adjust t_4 factor to minimize the contribution of ~2 Hz in P GC monitor.

3. t_3 factor Induce R motion with ~2 Hz signal from R input. Adjust t_3 factor to minimize the contribution of ~2 Hz in P GC monitor.

4. t_2 factor Induce X motion with ~2 Hz signal from X input. Adjust t_2 factor to minimize the contribution of ~2 Hz in P GC monitor.

5. t_1 factor Induce P motion with ~2 Hz signal from X input. Adjust t_1 factor to minimize the contribution of ~2 Hz in X GC monitor.

Appendix B

Circuit for the Local Control System

The following circuit was designed for the local control system.

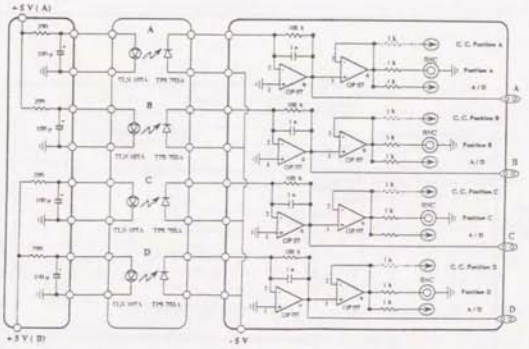

A, B, C, D → P, R, X, Y

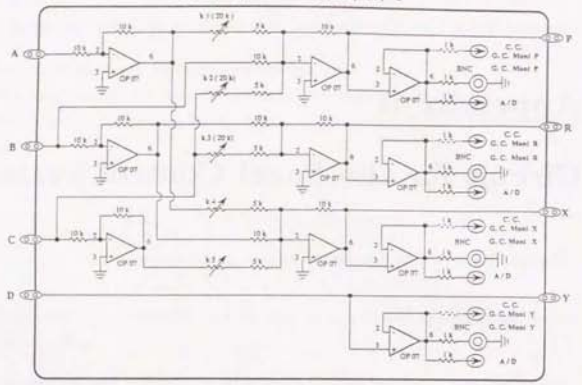

Band Pass Filter & Gain

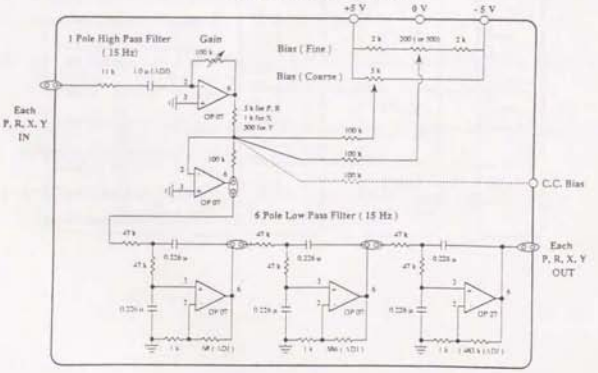

P, R, X, Y → A, B, C, D

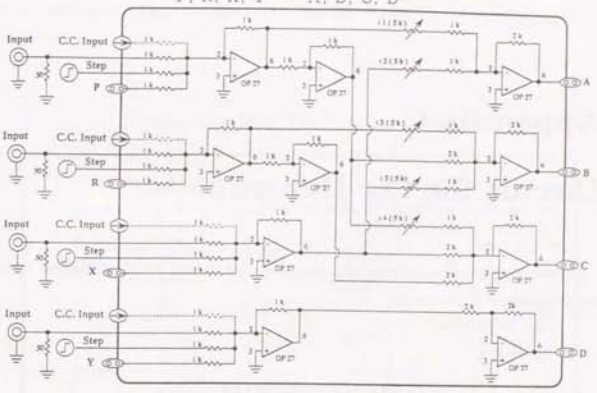

Driver

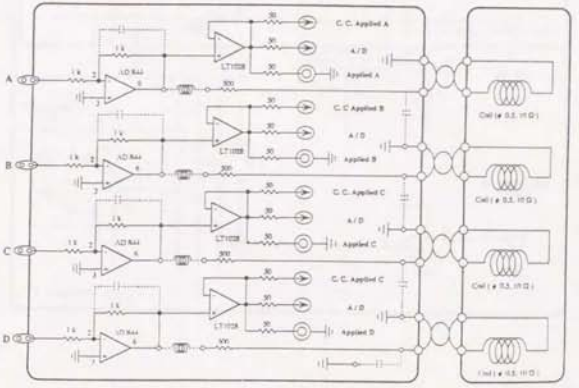

Appendix C

Circuit for the Demodulator

The following circuit was designed as low noise demodulator for the darkfringe locking and the absolute control system.

10MHz Demodulator (for Main)

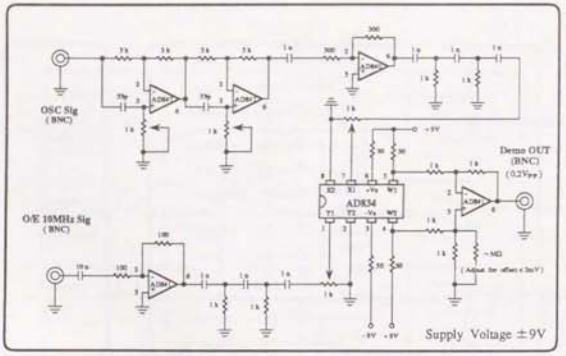

The following circuit was designed as low noise demodulator for the frequency stabilization system.

12.0MHz Demodulator (for Frequency Stabilization)

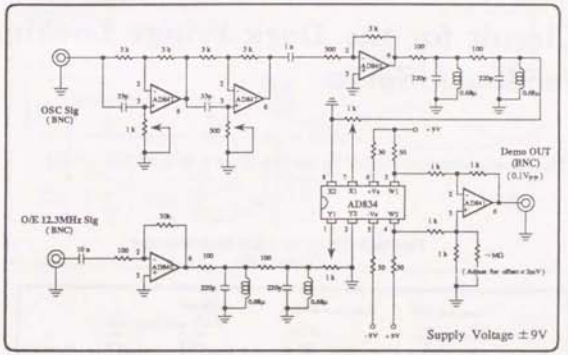

Appendix D

Circuit for the Dark Fringe Locking Feedback Servo

The following circuit is designed for the dark fringe locking for TENKO-100.

Feedback Circuit for Main Interferometer
(Pockels Cell)

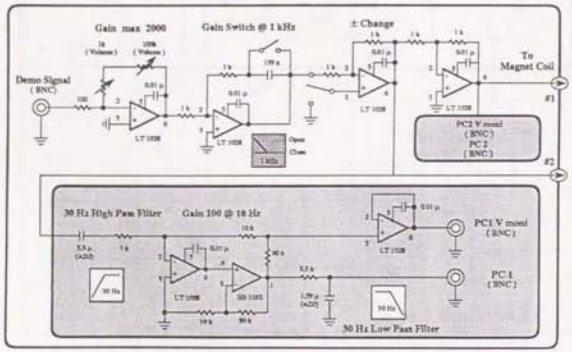

Feedback Circuit for Main Interferometer
(Magnet - Coil)

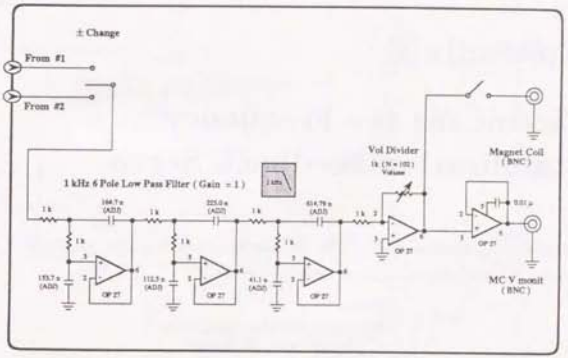

Appendix E

Circuit for the Frequency Stabilization Feedback Servo

The following circuit was designed for the three paths (the Slow PZT, the Fast PZT, the Pockels Cell) frequency stabilization system.

Frequency Stabilization Circuit
(Slow PZT & Fast PZT & EOM)

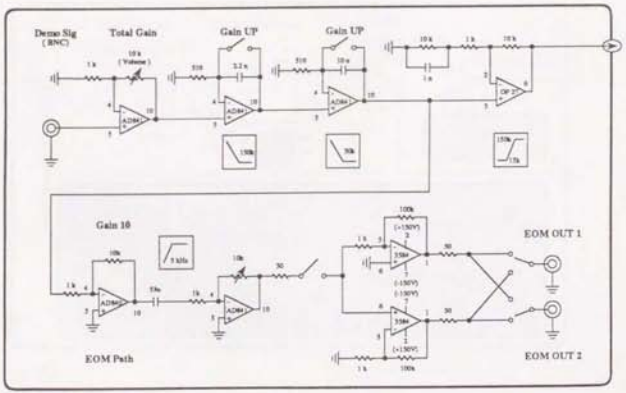

Frequency Stabilization Circuit
(Slow PZT & Fast PZT & EOM)

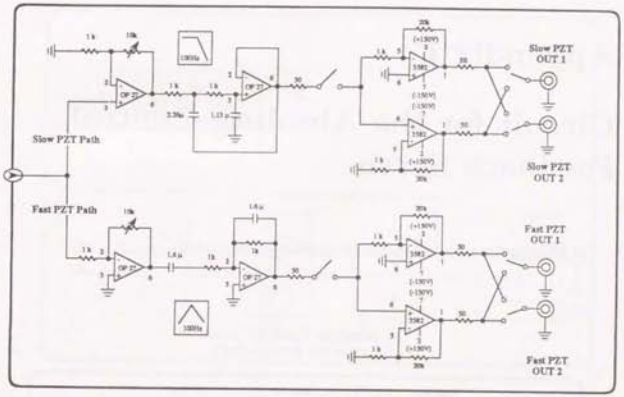

Appendix F

Circuit for the Absolute Control Feedback Servo

The following circuit was designed for the absolute control system.

Absolute Control Circuit
(Slow PZT & Magnet-Coil)

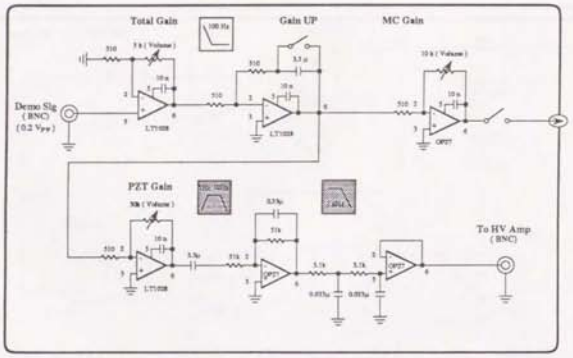

Absolute Control Circuit
(MC Path)

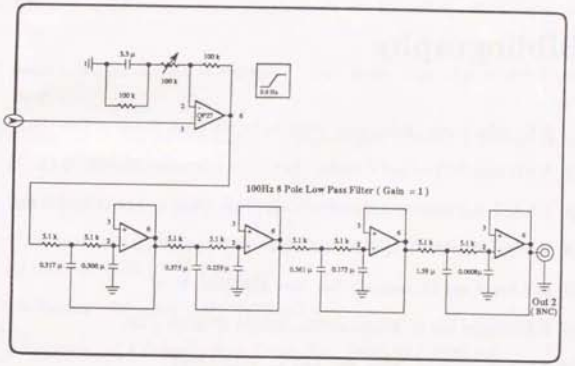

Bibliography

[1] A.Einstein, Sitzber. Deut. Akad. Wiss. Berlin, KI. Math. Physik u. Tech (1916) p.688

[2] R.v.Etövös, D.Pekar and E.Fekete : Ann. Phys. (Germany) 68 (1922) p.11.

[3] P.G.Roll, R.Krotkov and R.H.Dicke : Ann. Phys. (New York) **26** (1964) p.442.

[4] V.B.Braginsky and V.I.Panov : Sov.Phys. JETP **34** (1972) p.463.

[5] R.V.Pound and J.L.Snoder : Phys. Rev. **140** (1965) B788.

[6] R.F.C.Vessot and M.W.Levine : Gen. Relativ. **10**(1979) p.181.

[7] R.F.C.Vessot, *et al.* : Phys. Rev. Lett **45** (1980) p.2081.

[8] J.Bailer, *et al.* : Nature **268** (1977) p.301.

[9] A.Einstein, Sitzber. Deut. Akad. Wiss, Berlin : KI. Math. Physik u.Tech (1916).

[10] J.Weber : Phys. Rev. Lett. **22** (1969) p.1320.

[11] J.H.Taylor : *Paper presented at the 13th Int. Conf. on General Relativity and Gravitatio* of Cordoba, Argentina, 1992 : Part 1 Plenary Lectures.

[12] R.Vogt : *Proceedings of Marcel Grossmann Conference*, Kyoto, Japan (July 1991)

[13] *14th International Conference on General Relativity and Gravitation* of Florence, Italy. August 6-12. 1995 (Proceedings on press)

[14] M.Ohashi : Doctor Thesis. : *The development of a 20m Fabry-Perot laser interferometer for a gravitational wave detector* (1995).

[15] M.Araya : Doctor Thesis. *Optical Mode Cleaner for the Interferometric Gravitational Wave Detector* (1995).

[16] S.Kawamura, J.Mizuno, J.Hirao, N.Kawashima and R.Schilling : ISAS Report 637 (1989).

[17] Stuart L.Shapiro and Saul A.Teukosky : "*Black Holes, White Dwarfs, and Neutron Stars*"

[18] J.Hough *et al* Max-Plank-Institute fur Quantenoptik (Garching) Internal Report. MPQ **147** (1989).

[19] D.H.Hills, P.L.Bender and R.F.Webbink : Astrophys.J. **360** (1990) p.75.

[20] T.Nakamura and K.Oohara : Prog. Theor. Phys. **820** (1989) 535, **82** (1989) p.1066, **83** (1990) p.906, **86** (1991) p.73.

[21] E.S.Phinney : Astrophys.J. **380** (1992) L17.

[22] T.Nakamura and K.Oohara : Prog. Theor. Phys. Suppl. **90** (19879) p.1.

[23] R.Monchmeyer *et al.* : Astron. Astrophys. **246** (1991) p.417.

[24] T.Nakamura and M.Fukugita : Astrophys. J. **337** (1988) p.466.

[25] K. Ohara and T.Nakamura : Prog. Theor. Phys. **86** (1991) p.1788.

[26] J.Kristian *et al.* : Nature **338** (1989) p.234.

[27] F.B.Estabrook and H.D.Wahlquist : Gen. Relat. Gravit. **6** (1975) p.439.

[28] R.W.Helling : Phys. Rev. D. **17** (1978) p.3158.

[29] R.W.Helling, P.S.Callahan and J.D.Anderson : JPL. Res. July. 1980 "Spacecraft-Doppler Garavity Wave Detection II".

[30] *Proceedings of the Fifth Marcel Grossmann Meeting on General Relativity* of World Scientific, Singapore, 1989)

[31] S. Owa, M.K.Fujimoto, H.Hirakawa, K.Morimoto, T.Suzuki and K.Thubono : in *Proceedings of the Forth Marcel Grossmann Meeting on General Relativity* of World Scientific, North-Holland, 1986)

[32] Mizutani : Doctor Thesis. *Development of a Resonant-type Gravitational Wave Detector using an Interferometer* (1991). Univ of Tokyo.

[33] M.E.Gertsenshtein and V.I.Poustvoit : Sov. Phys. JEPT **16** (1963) p.433.

[34] R. Weiss : Progress Report, MIT. **105** (1972) p.54.

[35] P.R.Saulson : *Fundamentals of Interferometric Gravitational Wave Detectors.*

[36] ESA LISA Working Group : Proposal for Laser Interferometer Gravitati onal Wave Detector in Space, MPQ (1994)

[37] D.Herriot, H.kogelnik and R.Kompfner : Appl. Opt. **3** (1964) p.523.

[38] K.Tsubono *et al.* : Rev. Sys. Instrm. **64** (1993) p.2237.

[39] M.Stephens. P.Saulson. and J.Kovalik : Rev. Sci. Instrum. **62** (1991) p.924.

[40] Talking at "New Technology for Gravitational Astronomy" in Perth, 1993.

[41] N.Kanda, M.A.Barton, and K.Kuroda : Rev. Sci.Instrum. **65** (1994)

[42] M.Stephens. P.Saulson. and J.Kovalik : Rev. Sci. Instrum. **62** (1991) p.924.

[43] J.Hough, B.J.Meers, H.P.Newton, N.A.Robertoson, H.Ward, B.F.Schutz, I.F. Corbett and R.W.P.Drever : Vistas Astron. 30 (1987) p.109

[44] D. Shoemaker, W.Winkler, K.Maischberger, A. Rüdiger, R. Scilling and L.Schnupp : MPQ 100 (1985)

[45] R.Del.Fabbro. A.Di.Virgilio, A.Giazotto, H.Kautzky, V.Montelatici and D.Passuello : Phys. Lett. A **133** (1988) p.471.

[46] C.Bradaschia, R.Del.Fabbro, L.Di.Fiore, A.Di.Virgilio, A.Giazotto, H.kautzky, V.Montelatici and D.Passuello : Phys. Lett. A **137** (1989) p.329.

[47] D.Shoemaker. A.Brillet, C.N.Man, O.Cregut and G.Kerr : Opt. Lett. **14** (1989) p.609.

[48] D.Shoemaker. R. Scilling, L.Schnupp, W.Winkler, H.Billing and K.Maischberger : Phys. Rev. D **38** (1988) p.423.

[49] R.Takahashi : Doctor Thesis. *Development and Research of a Laser interferometric Gravitational Wave Antenna* (1993).

[50] H.Billing, K.Maischberger, A.Rüdiger, R.Schilling, L.Schnupp and W.Winkler : J. Phys. E. Sci. Instrum. **12** (1979) p.1043.

[51] D.Shoemaker, R.Scilling, L.Schnupp, W.Winkler, K.Maischberger and A.Rüdiger : MPQ **130** (1987a).

[52] A.Rüdiger, R.Schilling, L.Schnupp, W.Winkler. H. Billing and K.Maischberger : Opt. Acta. **28** (1981a) p.641.

[53] R.Schilling, L.Schnupp, W.Winkler. K.Maischberger and A.Rüdiger : J. Phys. E. Sci. Instrum. **14** (1981) p.65.

[54] K.Thorne : Caltech Pre Print. GRP-220.

[55] H.Hirakawa, K.Narihara and M.Fujimoto : J. Phys. Soc. Jpn. **41** (1976) p.95.

[56] P.R.Saulson : Phys. Rev. D **42** (1990) p.2437.

[57] K.Mio and M.Ohashi : The Technical Book for Interferometric Gravitational Wave Detectors **75** (1992).

[58] A.Giazotto : Phys. Rep. **182** (1989) p.365.